ORNL/TM-2012/455

OAK RIDGE
NATIONAL LABORATORY
MANAGED BY UT-BATTELLE
FOR THE DEPARTMENT OF ENERGY

Enhanced Ex-Vessel Analysis for Fukushima Daiichi Unit 1:

Melt Spreading and Core-Concrete Interaction Analyses with MELTSPREAD and CORQUENCH

February 2013

Prepared by
Kevin R. Robb and Matthew W. Francis
Oak Ridge National Laboratory

Mitchell T. Farmer
Argonne National Laboratory

UT-BATTELLE
ORNL-27 (4-00)

ORNL/TM-2012/455

ENHANCED EX-VESSEL ANALYSIS FOR FUKUSHIMA DAIICHI UNIT 1: MELT SPREADING AND CORE-CONCRETE INTERACTION ANALYSES WITH MELTSPREAD AND CORQUENCH

Kevin R. Robb, Ph.D.
Matthew W. Francis, Ph.D.
Oak Ridge National Laboratory

Mitchell T. Farmer, Ph.D.
Argonne National Laboratory

Date Published: February 2013

Prepared by
OAK RIDGE NATIONAL LABORATORY
Oak Ridge, Tennessee 37831-6283
managed by
UT-BATTELLE, LLC
for the
U.S. DEPARTMENT OF ENERGY
under contract DE-AC05-00OR22725

This page intentionally left blank.

CONTENTS

LIST OF FIGURES

LIST OF TABLES

ACRONYMS AND ABBREVIATIONS

ANL	Argonne National Laboratory
CAMS	containment atmospheric monitoring system
DOE-NE	Department of Energy: Office of Nuclear Energy
EPRI	Electric Power Research Institute
HEC	high flow rate glycerol
HP	high pressure
JNES	Japan Nuclear Energy Safety
LP	low pressure
MACE	Melt Attack and Coolability Experiment
MCCI	molten corium-concrete interaction
MT	metric ton
NEA	Nuclear Energy Agency
NRC	Nuclear Regulatory Commission
OECD	Organization for Economic Cooperation and Development
ORNL	Oak Ridge National Laboratory
RPV	reactor pressure vessel
SNL	Sandia National Laboratories
TEPCO	Tokyo Electric Power Company

EXECUTIVE SUMMARY

System-level code analyses by both United States and international researchers predict major core melting, bottom head failure, and corium-concrete interaction for Fukushima Daiichi Unit 1. Although system codes such as MELCOR and MAAP are capable of capturing a wide range of accident phenomena, they do not contain detailed models for evaluating ex-vessel core melt behavior. However, specialized codes containing more detailed modeling are available for melt spreading—such as MELTSPREAD—as well as long-term molten corium-concrete interaction (MCCI) and debris coolability—such as CORQUENCH. On this basis, the Office of Nuclear Energy within the U.S. Department of Energy (DOE-NE) funded an analysis to further evaluate the ex-vessel core debris location and extent of interaction for Unit 1 using modern modeling and simulation tools. The high-level objective was to utilize MELTSPREAD and CORQUENCH to provide rigorous "best estimate" predictions and analysis of ex-vessel core melt accident progression and final debris configuration. Argonne National Laboratory (ANL) performed the MELTSPREAD calculations, while Oak Ridge National Laboratory (ORNL) performed the CORQUENCH calculations.

The evaluation required the integration of models and data from several accident analysis codes. First, three sets of melt pour conditions following reactor pressure vessel (RPV) failure in Unit 1 were compiled based on MELCOR simulations performed by Sandia National Laboratories (SNL) [1] and MAAP simulations performed by the Electric Power Research Institute (EPRI) [2]. These melt pour conditions were used in MELTSPREAD as initial and boundary conditions to predict the time-dependent melt propagation, basemat attack, cladding oxidation (viz. H_2 and CO production), debris cooling, and drywell liner attack during the transient spreading phase. One of the principal outcomes of this analysis was the extent to which the floor was covered by core debris during spreading, since the depth of debris to be cooled in the long term is inversely proportional to the floor area covered by spreading melt. The MELTSPREAD results were then used to define tabular input for CORQUENCH. CORQUENCH was then utilized to evaluate the long-term debris cooling behavior, the amount of concrete ablation, and non-condensable gas generation. A cavity discretization model was developed that allowed localized core-concrete behavior within the drywell to be analyzed.

The MELTSPREAD simulations were performed using refined models for melt viscosity and leading-edge effects. The code also contains a detailed heat transfer model for predicting the heat-up and possible failure of the liner. The MELTSPREAD code has been validated against a total of 35 simulant as well as reactor material melt spreading tests. The CORQUENCH simulations were performed using state-of-the art models for core debris cooling, which includes water ingression through cracks or fissures that form in the debris during cooling, as well as melt eruptions that form as a result of gases sparging through the melt. These models were developed on the basis of a long series of reactor material core debris coolability experiments that were performed as part of the Melt Attack and Coolability Experiment (MACE) and the Organization for Economic Cooperation and Development's Nuclear Energy Agency (OECD/NEA) MCCI programs [10]. CORQUENCH has been validated against 16 reactor material core-concrete interaction experiments under both wet and dry cavity conditions.

The MELCOR [1] and MAAP [2] simulation results for Unit 1 span a wide range of melt pour conditions from the RPV ranging from a gradual pour of low-temperature core debris (MELCOR) to a rapid pour of high-temperature melt (MAAP). Since cavity conditions during the accident are uncertain, a limited sensitivity study was performed with MELTSPREAD to evaluate the effect of the presence and absence of water on the cavity floor, melt pour rate, and sump cover plate failure on the global spreading behavior. A parametric study was also conducted with CORQUENCH to evaluate the effect of the presence of water, cavity pressure, decay heat level, and modeling options on the long-term coolability of the melt.

The results of the MELTSPREAD analysis are highly dependent upon the pour scenario. For the low-temperature gradual MELCOR pour, the code predicts lethargic spreading of a highly viscous melt over a period of approximately 4000 seconds. Concrete ablation is minimal in these cases since the high viscosity limits convection from the melt to the underlying concrete. Despite the low flow rate, in all

cases the melt is predicted to eventually spread out of the pedestal doorway and contact the liner. MELTSPREAD predicted that the liner does not fail by thermal ablation in this location for the MELCOR simulations. When water is present, the core debris spreading is limited to a total of approximately 33 m^2.

For the high-temperature MAAP pours, MELTSPREAD predicted the sump plates rapidly ablated through in less than 5 seconds. Furthermore, the concrete erosion during spreading was significant with approximately 2 m^3 in the first 2 minutes with a maximum ablation depth of about 20 cm outside the pedestal door. The melt was also predicted to fully cover the pedestal and drywell annulus floor areas, which sum to approximately 111 m^2. Both low- and high-pressure MAAP pour sequences were analyzed. The drywell liner was predicted to remain intact for all low-pressure wet cases, and to fail by erosion due to impingement heat transfer from the melt for the high-pressure cases.

The results from the MELCOR and MAAP simulations and the subsequent MELTSPREAD simulations were then used as initial and boundary conditions for the long-term debris coolability analysis with CORQUENCH. If sufficient water was injected into containment to cover the debris starting 15 hours after shutdown, the simulations indicate that the melt was coolable over the long term. The predicted concrete ablation was less than that necessary to reach the liner through downward melt progression. The MELCOR case, which contained relatively cool melt, readily cooled within 2.5 hours after relocation with limited concrete ablation in the sump regions (~18 cm) and less than 10 cm ablation elsewhere. Seventy-six kilograms of hydrogen and 103 kilograms of carbon monoxide were predicted to be generated during core-concrete interactions. The MAAP cases, which contained relatively hot melt, cooled approximately 22.5 hours after melt relocation and resulted in 65 cm of concrete ablation in the sump region and less than 23 cm elsewhere in containment. Large amounts of hydrogen (700 kg), carbon monoxide (750 kg), and carbon dioxide (490 kg) were predicted to be generated during concrete ablation for the MAAP cases.

Key findings of the analysis and their possible implications include the following.

- Given the pour conditions, melt has spread from the pedestal into the drywell and contacted the liner in all cases and scenarios considered. The depths did not exceed the torus downcomer height, so a large amount of core debris is not likely present in the torus.
- The liner was predicted to remain intact for all scenarios under which the RPV had failed after being depressurized. This is consistent with the Mark I liner attack resolution [3] and is also consistent with the recent MELCOR simulations of the Fukushima Daiichi Accident Study [1]. The liner was predicted to fail by erosion due to impingement heat transfer from the melt for all scenarios under which the RPV had failed before being depressurized.
- The 140 tons of core debris is predicted to have been quenched and stabilized following the spreading transients.
- Based on the phenomenology predicted by the codes, the debris should be present as a highly cracked monolithic structure (due to water ingression); this will facilitate eventual removal. The debris is likely not in a particle-bed-type configuration due to the prediction of very limited melt eruption activity (low-gas-content concrete).
    - Based on previous experiment data, the cracked-monolithic debris may have a bulk tensile strength on the order of 1 MPa or less [4].
- The drywell pedestal and floor should be relatively intact after debris removal, with the exception for a pit that would have been eroded outside the pedestal doorway (for MAAP cases).
- The melt pour characteristics impact the final melt distribution and resulting radiation field. The high-flow-rate and high-temperature MAAP pours (in contrast to the low-temperature and low-flow-rate MELCOR pour) resulted in a substantial amount of debris spreading out of the pedestal region into the annular drywell region. Under these conditions, material may have washed up on interior surface of pedestal wall and also on the drywell liner, leaving crust material up a meter or so high. The final debris distribution will provide clues as to the melt pour conditions and accident progression.

1. INTRODUCTION

1.1 BACKGROUND

The MELCOR code simulations for Fukushima Daiichi Unit 1, carried out as a part of a joint effort between the Office of Nuclear Energy within the Department of Energy (DOE-NE) and the Nuclear Regulatory Commission (NRC) Fukushima Daiichi Accident Study [1], predict major core melting, bottom head failure, and corium-concrete interaction. These predictions are in agreement with simulations performed by the Electric Power Research Institute (EPRI) using the MAAP code [2], as well as the Japanese Nuclear Energy Safety Organization (JNES) using MELCOR [5] and the Tokyo Electric Power Company (TEPCO) using MAAP [5,6]. In addition, containment atmospheric monitoring system (CAMS) and reactor pressure vessel (RPV) temperature data as well as energy balance analysis suggest that melt has exited the RPV [7–9]. However, for Units 2 and 3 the MELCOR simulation results [1], as well as results presented by JNES [5] and TEPCO [5,6,8], span a range of possible final core conditions from core debris stabilization in-vessel to partial melt relocation from the RPV. This large range is due to uncertainties in the accident sequence of events for these two units, as well as uncertainties in the timing and rate of water injection. Due to these uncertainties for Units 2 and 3, the focus of the current work is on the ex-vessel accident progression for Unit 1.

Both MELCOR and MAAP are capable systems-level modeling tools that capture a wide spectrum of accident phenomena in a tractable manner. However, for ex-vessel sequences, specialized codes containing more detailed modeling are available for the analysis of melt spreading such as MELTSPREAD [10,11] as well as debris coolability during molten corium-concrete interaction (MCCI) such as CORQUENCH [12,13]. This work focuses on utilizing MELTSPREAD and CORQUENCH to further investigate the ex-vessel core debris relocation and long-term cooling behavior.

1.2 OBJECTIVES

The high-level objective of this work is to utilize MELTSPREAD and CORQUENCH to provide more rigorous, best-estimate predictions and analysis of ex-vessel core melt accident progression and final debris configuration for Fukushima Daiichi Unit 1 based on best-estimate melt pour conditions from MELCOR [1] and MAAP [2] simulations. Other general goals of the study are to

i) provide results for comparison against MELCOR and/or MAAP simulation results,
ii) scope out the range of possible ex-vessel core melt accident progression and final debris configuration, and
iii) identify uncertainties in the predictions.

The results of this study are expected to aid the decommissioning efforts by providing estimates of core debris location(s). Ultimately though, findings from the decontamination and decommissioning efforts are expected to support validation of both domestic as well as international severe accident codes. Finally, this work is intended to support ongoing forensic modeling efforts related to the accident sequence and flammable gas generation.

1.3 APPROACH

Given best-estimate melt pour conditions following RPV failure based on MELCOR [1] and MAAP [2] analyses of the Unit 1 accident sequence, MELTSPREAD was used to predict the time-dependent melt spreading, basemat attack, cladding oxidation (viz. combustible gas production), debris cooling, and drywell liner attack during the transient spreading phase. One of the principal outcomes of this analysis was the extent of floor coverage during spreading, which is important since (to first order) the depth of debris to be cooled in the long term is inversely proportional to the floor area covered by

spreading melt. Since cavity conditions during the accident are uncertain, a limited sensitivity study was performed to evaluate the effect of the presence/absence of water on the cavity floor, melt pour rate and temperature, and sump cover plate failure on the global spreading behavior. The MELCOR and MAAP vessel failure predictions cover a wide range of conditions ranging from a gradual pour of low-temperature core debris (MELCOR) to a rapid pour of high-temperature melt (MAAP).

MELTSPREAD and CORQUENCH are two separate and distinct computer codes. Thus, MELTSPREAD results were used to define tabular input for CORQUENCH, which in turn evaluated the long-term debris cooling behavior. As part of this work, a cavity discretization model was developed that allowed localized core-concrete behavior within the drywell to be analyzed. The CORQUENCH cases were performed using state-of-the-art models for core debris cooling that include water ingression through cracks/fissures that form in the debris during cooling, as well as melt eruptions that form as a result of gases sparging through the melt.

1.4 OVERVIEW OF TOOLS AND CAPABILITIES

The MCCI modeling capability of MELCOR v2.1 is based on CORCON-Mod3 [14]. Since the development of that code, a number of international research programs and experiments have been conducted (MACE, OECD/NEA MCCI-1, and MCCI-2 [15]). Insights and models from these research activities have been integrated into the CORQUENCH code. Phenomena accounted for in CORQUENCH that are not in MELCOR (e.g., crust anchoring and debris cooling by water ingression and melt eruption mechanisms) are known to have potentially large impacts on MCCI progression [15–17].

The CORQUENCH code predicts melt debris coolability and the axial and radial ablation of concrete due to MCCI. In the event that the debris does not quench, the code predicts melt penetration through the containment liner . The code also predicts the amount of gases liberated from the decomposing concrete, oxidation of the melt debris, and steam generated from any water cooling. These processes impact containment failure through pressurization and possible H_2/CO deflagration or detonation.

A number of initial and boundary conditions are required by CORQUENCH. These include the melt mass relocated, the initial temperature and composition, and the decay heat level (timing of relocation). Another key input is the area over which the melt is spread. In general, the volume of melt divided by this area yields the melt pool height. Sensitivity studies have shown this parameter to be among the most important initial conditions for MCCI predictions [16].

The MELCOR code predicts the melt spread area through use of a mass balance and a basic empirical hydraulic relationship which spreads the melt based on the melt height and temperature [1]. The code does not take into account viscosity or leading-edge freezing effects, which are key physics to the spread process. Thus, there is a high degree of uncertainty in the melt spread area predicted by MELCOR.

In contrast, MELTSPREAD calculates the area over which the melt spreads, taking into account a number of physical phenomena including varying melt viscosity, heat transfer, and solidification at the leading edge of the spreading melt. Utilizing MELTSPREAD will provide a “best estimate” of the melt-concrete contact area for use in CORQUENCH. This best estimate of the lateral melt location is also useful for understanding the current state of the core debris and for decommissioning guidance.

In addition to predicting the lateral spread of the melt, MELTSPREAD has the ability to predict melt-liner attack and failure of the liner if the melt is predicted to contact the drywell liner (near the floor). The analysis effort will investigate whether this failure mode is an alternative to the current containment head-lifting hypothesis [1] for Unit 1.

2. MODEL DESCRIPTIONS AND CODE VALIDATIONS

This section provides a brief description of both the MELTSPREAD and CORQUENCH models, as well as an overview of the validation status for both codes.

2.1 MELTSPREAD DESCRIPTION

MELTSPREAD was originally developed to support resolution of the Mark I liner vulnerability issue [3]. Given the time-dependent core melt pour conditions (i.e., temperature, composition, and flow rate) from the reactor pressure vessel (RPV), the code solves the one-dimensional momentum equation to evaluate melt spreading depth and velocity while accounting for local core debris cooldown and solidification, concrete heat-up and decomposition, metals oxidation from concrete decomposition gases, and heat transfer to overlying atmosphere under both wet and dry cavity conditions. The code was developed to treat a wide range of melt compositions ranging from fully metallic to fully oxidic. In addition, the code has the ability to calculate heat-up of structure adjacent to (or in the pathway of) flowing core debris. This model was specifically developed to examine heat-up of the Mark I liner under conditions in which the core debris was calculated to make contact with that structure. However, one modeling deficiency for wet cavity cases is that the code does not calculate melt fragmentation and cooling as the core debris relocates through water and onto the cavity floor. Cooling during this phase is expected to influence the subsequent spreading behavior.

MELTSPREAD was recently updated and extensively validated for application to spreading in the European Pressurized Reactor core catcher design [18]. A literature review indicated that several improvements to the code would be needed in order to make comparisons with the full range of melt spreading data involving heat transfer and solidification. In particular, the melt property subroutines in the original code were only capable of treating mixtures of core and cladding metals and their corresponding oxides, and only substrates composed of concrete, steel, or an arbitrary combination thereof. Thus, one of the first improvements was to provide the ability to input simulant melt and/or substrate material properties (density, thermal conductivity, solid/liquid phase specific heats, heat of fusion, emissivity). This allowed all "simulant oxide" tests identified in the literature to be calculated, as well as tests with ceramic substrate, using property data that were in almost all cases provided by the institutions that carried out the experiments. The ability to overwrite selected melt material properties was also added for sensitivity analysis.

Another key modeling improvement in the area of material properties was providing the ability to input a tabular function for the oxide-phase solid fraction variation between the liquidus and solidus temperatures. The original version of the code assumed that the oxide-phase solid fraction varied linearly in this range, but research since that time has shown that the functional dependence is highly nonlinear for multi-component oxide melts (e.g., see Journeau et al. [19]). Since solid fraction has an important effect on viscosity which, in turn, strongly affects spreading behavior, this was one of the most important improvements to the code in the area of material properties evaluation.

Several other code improvements were also made. The capability to carry out inviscid and/or adiabatic spreading analysis was also added, so that analytical solutions as well as isothermal spreading tests could be calculated by appropriate selection of input data. The ability to model an interfacial heat transfer resistance at the melt-substrate interface was also added. This is important in terms of calculating spreading and solidification of metallic melts for which shrinkage at the melt–substrate interface can have a marked effect on the local heat transfer rate [20–22].

Finally, of the thermo-physical properties affecting spreading, viscosity is the most important [23]. The initial code version used the Ishii-Zuber [24] correlation to account for the effects of solids buildup in the melt on increasing corium viscosity. However, code applications to the database indicated that spreading behavior was better reproduced using the correlation developed by Ramacciotti et al. [25]. In this model, the apparent melt viscosity in the freezing range is correlated as

$$\mu_{app} = \mu_o e^{2.5 C_R \alpha_{sol}},$$

where μ_o is the viscosity at the melt liquidus, α_{sol} is the melt solid fraction, and C_R is an empirical constant that depends upon experiment conditions and varies between 4 and 8 [25]. This model was added as a user option, with the constant C_R left as user specified. As is evident from above equation, accurate knowledge of the solid-fraction variation between the solidus-liquidus is important when using this correlation.

2.2 MELTSPREAD VALIDATION

A key element of the validation process was to assemble a set of test cases against which the code could be compared to check the accuracy of the numerical algorithms and to determine the extent to which the model can reproduce actual spreading behavior [18]. This validation matrix is shown in Table 1. A determining factor in the decision to include a given test in the matrix was that sufficient information was available through open literature sources to assemble a model that included details of the spreading geometry, materials employed, and test operating conditions. Note that this table does not include every test that was reported in the literature. Rather, the matrix was selected to cover the full range of programs for which information was available (e.g., additional tests were conducted as part of the KATS and VULCANO spreading programs), and to provide diversity in the validation database. As shown in the table, a total of 35 different cases were calculated as part of the code verification and validation exercise. The information can be broken down as follows.

1. Analytical solution to dam break problem (one case [26])
2. Isothermal tests (six cases [27,28])
3. Flow and freezing tests (28 cases); that is, core oxides (seven tests [19, 23, 29–32]), core oxide–steel mixtures (four tests [31–32]), simulant oxides (12 tests [33–37]), and steel alone (five tests [34, 35, 38])

The category of flow and freezing tests include five cases in which water was present in the cavity. Spreading on concrete, ceramic, and steel substrates was investigated. The database includes information on spreading velocity, total melt penetration, posttest debris profile, substrate heat-up/ablation profiles, and local melt temperatures. The MELTSPREAD validation calculations included comparisons to all available information for each test in order to evaluate the overall predictive capability of the code.

The code was first compared with the isothermal spreading data to verify proper behavior before moving on to the tests involving freezing effects. The code was found to reproduce the analytical solutions for leading-edge depth and velocity for the dam break problem [26]. For the water spreading tests of Theofanous et al. [27], the code reasonably replicated fluid arrival times and subsequent depth profiles at various locations within a scaled mockup of the Mark I containment. Code predictions were also compared with Corine spreading data [28]. The comparison for a low-flow-rate water test is provided in Figure 1, while the comparison for a high-flow-rate glycerol (HEC) test is shown in Figure 2. In general, the leading-edge penetration vs. time for both cases is reasonably reproduced. Calculations for both wetted and non-wetted surface conditions are shown to illustrate the effect of surface tension on leading-edge propagation.

With regard to heat transfer and solidification effects, one of the key questions addressed in the code assessment [18] was how to translate uncertainties in spreading analysis to plant calculations. A modeling sensitivity study was performed by Journeau et al. [23] with the THEMA code [39–41]. The results of this study indicated that the exponential parameter C_R in the Ramacciotti viscosity correlation, given above is one of the primary factors influencing melt spreading length. Spreading length is also a

key factor that influences longer term behavior in containment such as the extent that debris may be permanently cooled by overlying water (since the melt depth is inversely proportional to spreading area).

Table 1. MELTSPREAD Validation Test Matrix (35 cases in total)

Case or Program	Test or Case	Fluid	Substrate	Flow Geometry	Cavity Condition
Benjamin [26]	1-D dam break Analytical Solution	Water	Inert	1-D channel	N/A
Theofanous [27]	Run no. 1	Water	″	1/10 linear scale model of Mark-I containment	Ambient
	Run no. 2	″	″	″	″
Corine [28]	WAT_Q1.5_G0	Water	″	Feedbox with 24 cm weir → 17º sector	″
	WAT_Q0.5_G0	″	″	″	″
	HEC_3_G0_0.1[a]	HEC[a]	″	″	″
	HEC_3_G0_2[a]	″	″	″	″
RIT [33]	3MDC-Ox-1	Oxide simulant[b]	Concrete	Feedbox → 1-D channel	Dry
	3MDS-Ox-1	″	Steel	″	″
	3MDS-Ox-2	″	″	″	″
	2MWS-Ox-1	″	″	″	12 cm H_2O
	2MWS-Ox-2	″	″	″	″
	2MWS-Ox-3	″	″	″	″
Kats [34,35]	KATS-12	Iron	Ceramic	Feedbox → 1-D channel	Dry
		Oxide simulant[c]	″	″	″
	KATS-13	Iron	Concrete	″	
		Oxide simulant[c]	″	″	″
	KATS-14	Iron	Ceramic	″	″
		Oxide simulant[c]	″	″	
ECOKATS [36,37]	V1	Oxide simulant[d]	Ceramic	″	″
	1	″	Concrete	Feedbox → 1-D channel → 2-D floor	″
	2	″	″	″	″
SPREAD [38]	Test 15	Stainless steel	″	Cylindrical cavity with door →180º sector	″
	Test 21	″	″	″	7 cm H_2O
COMAS [31,32]	COMAS-5a	Core oxides + iron	Concrete	Feedbox with 5 cm weir → 1-D channel	Dry
		″	Ceramic	″	″
		″	Steel	″	″
	EU-2b	Core oxides	Concrete	″	″
		″	Ceramic	″	″
		″	Steel	″	″
	EU-4	Core oxides + iron	″	Feedbox with 5 cm weir → 1-D channel → 45º sector	″
Faro [30]	L-26S	″	″	Cylindrical cavity with 4 cm weir → 17º sector	″
	L-32S	″	″	″	1 cm H_2O
VULCANO [19, 23,29]	EU-7	″	Concrete	Feedbox box with 0.5 cm weir → 9.5º sector	Dry
		″	Ceramic	″	″

[a] Hydroxyl ethyl cellulose
[b] 30/70 wt% CaO/B_2O_3
[c] 83/8.5/6/1.5/1 wt% Al_2O_3/ SiO_2/FeO/MgO/MnO
[d] 41/24/19/16 wt% Al_2O_3/FeO/CaO/SiO_2

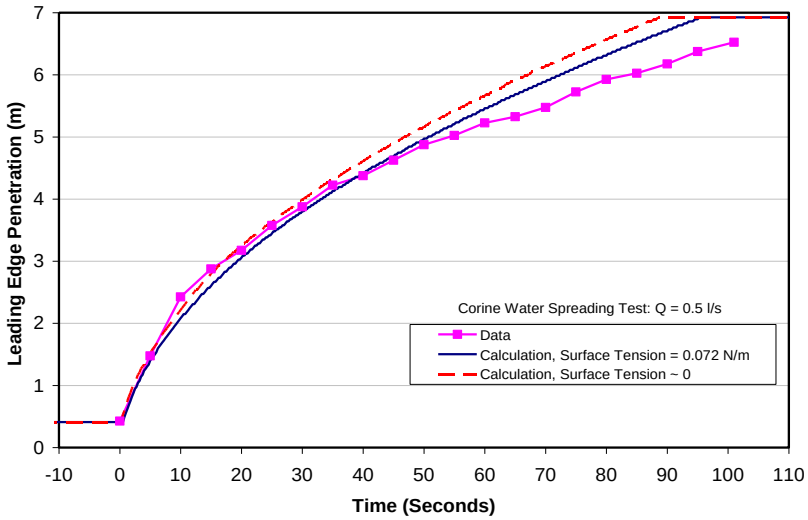

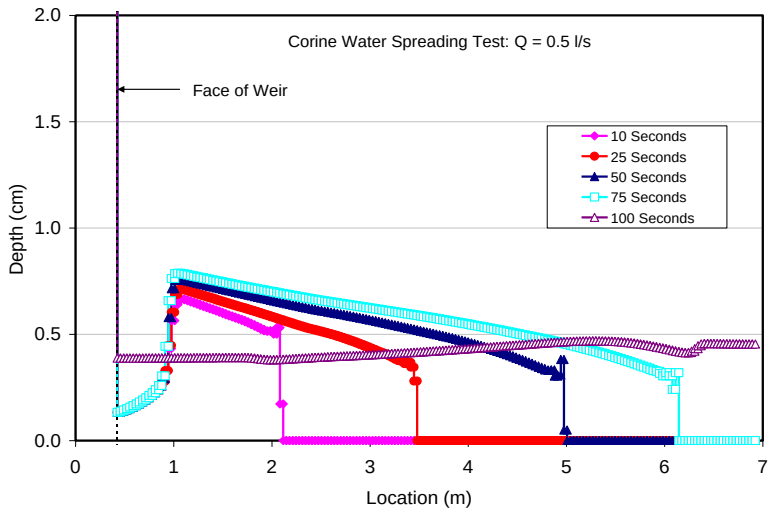

Fig. 1. Leading Edge Penetration (left) and Depth Profiles (right) for Corine [28] Water Spreading Test WAT_Q0.5_G0.

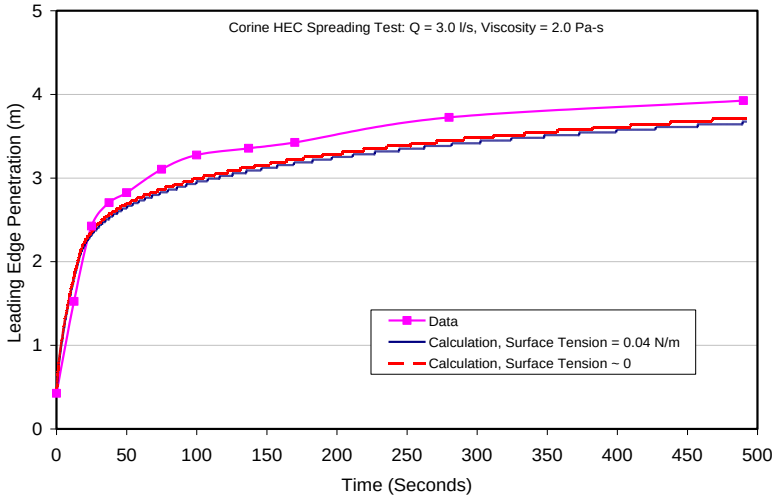

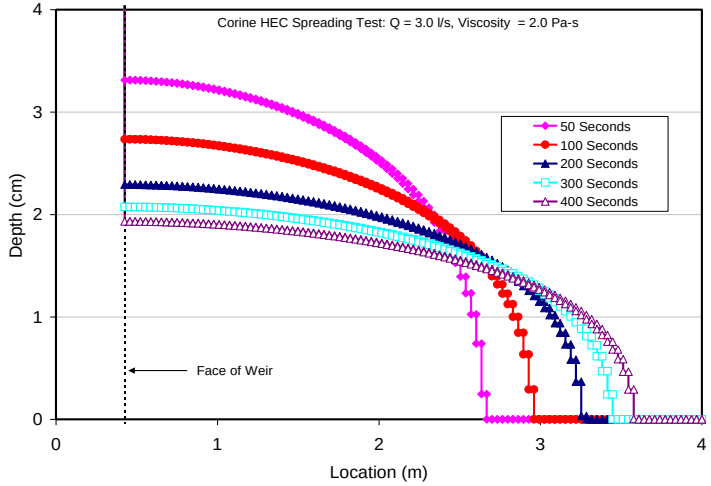

Fig. 2. Leading-Edge Penetration (left) and Depth Profiles (right) for Corine [28] Glycerol Spreading Test HEC_3_G0_2.

On this basis, parametric calculations were performed for each test shown in Table 1 to find the value of C_R that reproduced the experimentally observed spreading length [18]. With this collection of information, a simple statistical analysis was performed to find the average C_R that best fits the data for all experiments, as well as the standard deviation in the fit. The results of this exercise for the reactor material oxide and oxide plus metal tests indicated an average value of C_R of 7.26, with a standard deviation of 0.95 in the parameter fit to the data.

As noted earlier, accurate knowledge of the melt solid-fraction variation between the liquidus and solidus is important when using the Ramacciotti viscosity correlation. The assumed solid fraction functions for the steel and core oxide tests calculated as part of the code assessment exercise are shown in Figure 3. For the Vulcano VE-U7 core oxide test [19], this function was provided as part of the program. However, for the balance of the tests, these functions were not provided and so they were evaluated using the CORQUENCH [12] property subroutines. These subroutines are, in turn, based on early thermo-physical property calculations carried out with the OXY5-GEMINI2 code by Chevalier (see [12]). As is evident, the solid-fraction function for core oxide material is highly nonlinear. The linear function shown for steel in Figure 3 is assumed.

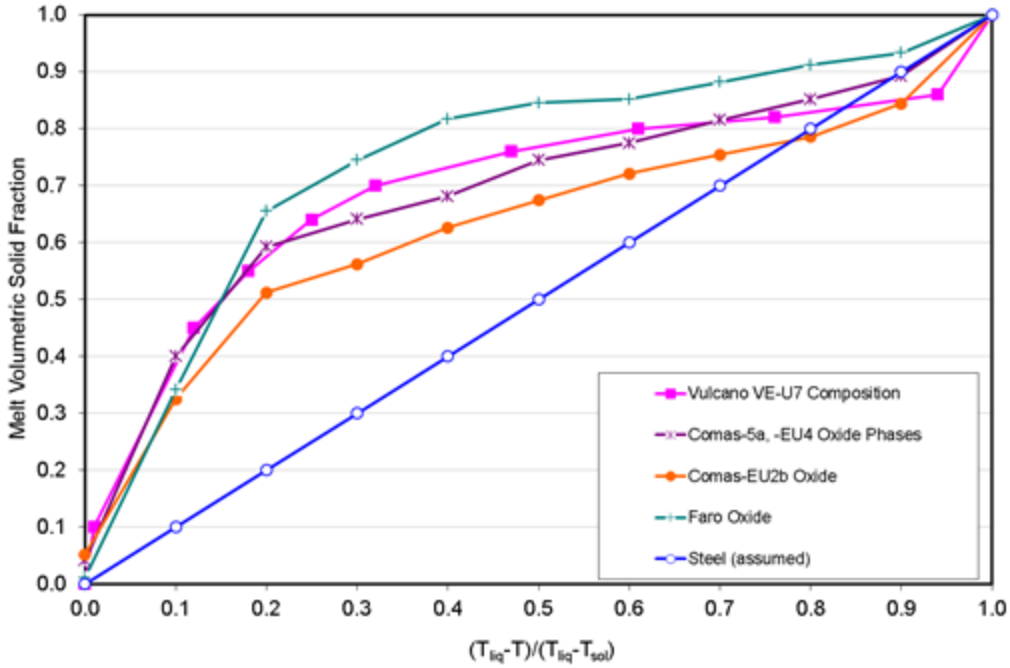

Fig. 3. Core Oxide and Steel Solid-Fraction Functions Assumed for the Various Melt Compositions Addressed in the MELTSPREAD Code Assessment Study [18].

To illustrate the predictive capability of the code under flow and freezing conditions, the VULCANO VE-U7 core oxide melt spreading test on a concrete surface is briefly presented here. The calculated leading-edge penetration, local concrete thermal response, and post-spreading material profile results are compared with test data in Figure 4. Results for C_R =7.26 and $C_R \pm 2\sigma_{C_R}$ are shown in the graph of the leading-edge penetration distance. Temperatures in the concrete substrate 30 cm from the injection box are underestimated near the concrete surface (i.e., 2 mm recess), but the discrepancy decreases as depth into the substrate increases. Finally, the overall shape in the posttest debris profile is reasonably reproduced, but the depth is consistently less than reported for the test [23]. This is due to the fact that the oxide material freezes with porosity due to gas sparging, but porosity during solidification is not modeled by the code.

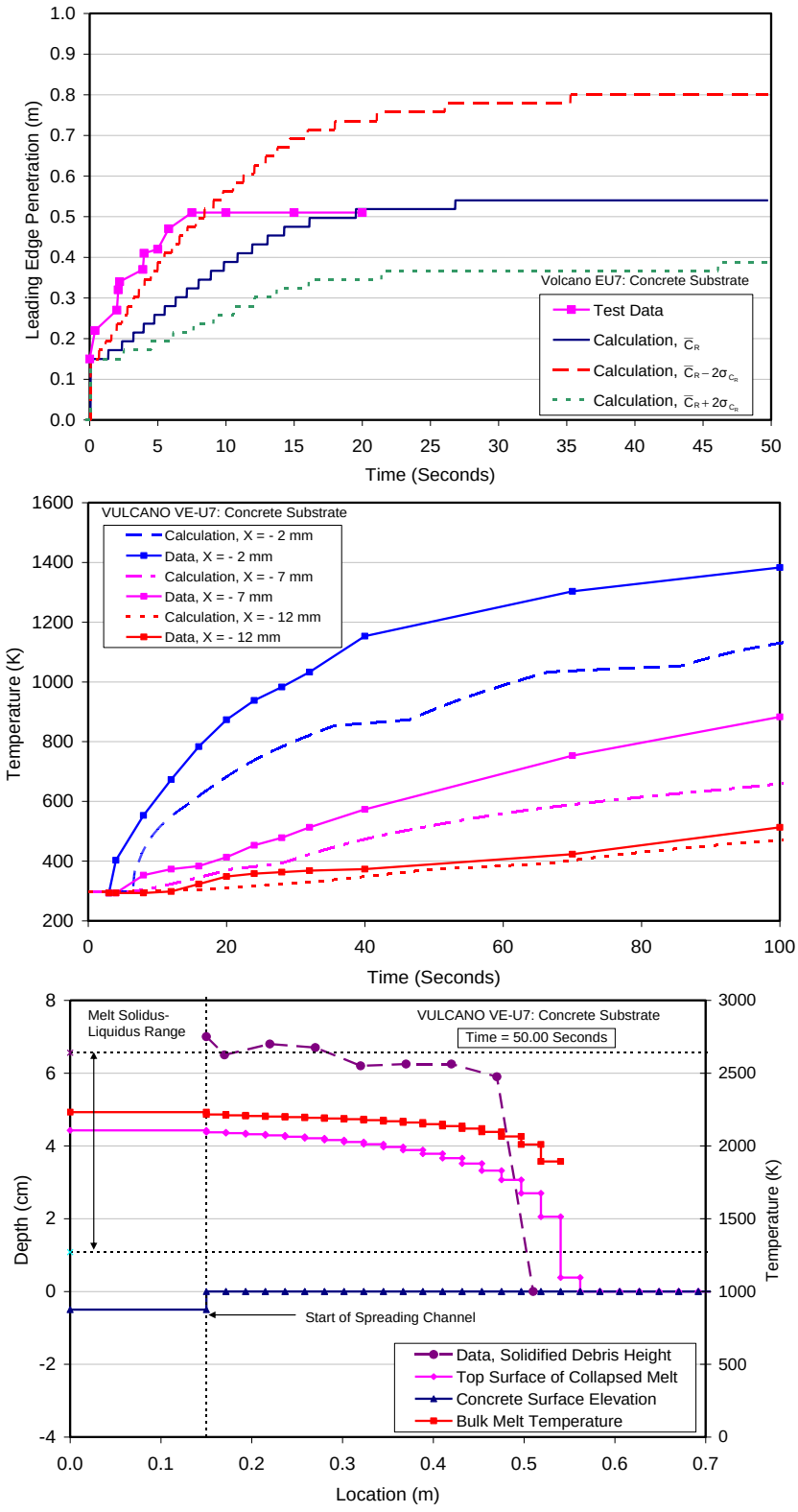

Fig. 4. Melt Penetration (top), Substrate Temperatures (middle), and Debris Profile (bottom) for the VULCANO VE-U7 [23] Core Oxide Spreading Test over Concrete.

2.3 CORQUENCH DESCRIPTION

CORQUENCH [12] was originally developed to provide a simple, modular model of MCCI behavior that could readily be adapted to investigate the adequacy of melt/water heat transfer correlations as they were developed. However, due to the novel nature of the debris cooling models deployed within this code, it is now being used more broadly for reactor safety evaluations [16].

The MCCI model within CORQUENCH is capable of performing either a 1-D or simplified 2-D ablation calculation (2-D geometry can be selected to be either cylindrical or rectilinear, with average axial and radial ablation depths calculated). The MCCI conservation of energy equation includes the following energy source/sink terms: (i) decay heat, (ii) mass flux of melt from the failed reactor pressure vessel, (iii) chemical reactions between metallic melt constituents Zr, Cr, Fe (in sequence) and concrete decomposition gases H_2O and CO_2, (iv) condensed-phase chemical reactions between Zr and SiO_2, (v) downward (and sideward for 2-D case) heat transfer to concrete, including slag heat sink, and (vi) heat transfer to overlying atmosphere (wet or dry). The melt composition can range from fully metallic to fully oxidic; in all cases, the two phases are assumed to be well mixed (i.e., phase stratification is not modeled). The MCCI conservation of mass equations and thermo-physical property subroutines consider most core and concrete metals and their corresponding oxides, so that a wide range of cases can be considered. Melt viscosity is calculated using the Andrade formula (see Nazare et al. [42]) with a correction for SiO_2 as developed by Shaw [43]. Viscosity enhancement due to buildup of solids within the melt can be calculated using either the Ishii-Zuber [24] or Kunitz [44] models. Melt void fraction, which is relevant in determining the location where the crust anchors to the test section sidewalls in experiments, can be evaluated from one of several different correlations, that is, those due to Brockmann et al. [45], Wallis [46], or Kataoka and Ishii [47].

In terms of heat transfer at the melt/concrete interface, CORQUENCH incorporates a transient concrete ablation/decomposition model based on integral thermal boundary layer theory (Corradini [48]). This model was upgraded as part of the code development work [12] to account for the effects of transient concrete heat-up with simultaneous crust growth following initial melt contact with the concrete. The inclusion of a concrete dryout model is considered to be important in evaluating both the early and late phases of a core-concrete interaction. In the early phase, transient crust formation can affect the timing of onset of ablation, while in the late phase, heat transfer to underlying concrete can fall to low levels as the decay heat decreases, and so conduction into the concrete behind the ablation front becomes important in determining the overall ablation depth. The heat transfer coefficient at the melt/concrete interface can be selected from a variety of options, including (i) Bradley's modification [49] to the bubble agitation heat transfer model of Kutateladze and Malenkov [50], (ii) gas film models similar to those deployed in CORCON Mod3 [14], or (iii) the empirical correlations developed by Sevon [51] on the basis of the CCI test results.

At the melt upper surface, radiant heat transfer to overlying structure is calculated when the cavity is dry. When water is present, bulk cooling and incipient crust formation are calculated using the models developed by Farmer et al. [52, 53]. Following incipient crust formation, crust growth is calculated by solving a growth rate equation; the crust material composition is treated separately from the melt material composition, which is important in long-term calculations where significant mass may be frozen in the crust. The melt-side convective heat transfer coefficient is calculated using the correlation of Kutateladze and Malenkov [50]. For the case in which the crust is treated as permeable to water ingression, then the crust dryout limit can be calculated using either a user-specified crust permeability, or the dryout heat flux can be calculated using the Lomperski and Farmer model [54].

For situations in which water is present and a particle bed develops over the crust, the heat flux from the crust upper surface may be limited by the particle bed dryout limit. For this case, the bed dryout limit is calculated with the Lipinski correlation [55]. The heat flux from the crust upper surface is checked during the calculation to ensure that it does not exceed the effective dryout limit. If this limit is exceeded, then the heat flux from the crust surface is capped at the dryout limit.

With respect to wet cavity conditions, one significant model shortcoming is that the code does not currently possess the ability to correctly model situations in which the debris may dry out, or be undercooled by virtue of inadequate water flooding supply. Thus, the model can only address wet cavity scenarios in which the water supply and the rate of addition is adequate to prevent the water inventory from boiling off. The scenario where there is insufficient water addition to keep the debris flooded is bounded by scenarios assuming continuously dry and continuously wet conditions.

In addition to calculating crust growth under a variety of modeling assumptions, particle bed formation by the mechanism of melt eruptions is also evaluated. In order to incorporate the basic elements of this cooling mechanism in the current analysis, the modeling approach of Bonnet and Seiler is adopted [56]; that is, melt dispersal is calculated by assuming that the melt entrainment rate is proportional to the gas volumetric flow rate times an entrainment coefficient. Several options are provided for evaluating the melt entrainment coefficient: (i) the user may specify the coefficient directly, (ii) the entrainment coefficient can be evaluated with the Ricou-Spalding model [57], or the coefficient can be evaluated using the model due to Farmer [58], which also provides analytical solutions for the active melt eruption hole site density, as well as the average eruption hole diameter. Consistent with test observations, the dispersed melt is assumed to be rendered in the form of an accumulating particle bed (with specified particle diameter and porosity) on top of the crust. As noted earlier, the bed dryout heat flux limitation is evaluated with the Lipinski correlation [55].

The above methods provide a general framework for predicting simultaneous upper crust and particle bed growth rates during MCCI. However, the model has also been developed to mechanistically calculate the important experiment distortion of crust anchoring to the test section sidewalls, as well as the subsequent melt/crust separation phase which arises due to concrete densification upon melting. For a given cavity span, the minimum crust thickness required to be mechanically stable due to the combined weights of the overlying water pool, particle bed, and the crust itself is evaluated using a first-order plate strength equation from Roark and Young [59]. During the calculation, the upper crust thickness is compared with that predicted from the Roark and Young equation. When the thickness exceeds the minimum required to be mechanically stable in the given cavity configuration, the crust is assumed to attach to cavity sidewalls with the upper surface elevation fixed at the location at the time of anchoring. Thereafter, the voided melt upper surface location is tracked relative to the crust location so that the onset of gap formation can be predicted. When a gap does form, debris quenching by the mechanisms of crust water ingression and melt eruptions is terminated, and there is a corresponding reduction in upwards heat transfer due to solidification (latent heat) processes. Moreover, a heat transfer resistance across the gap is introduced into the heat balance, which causes a further reduction in upwards heat transfer. This methodology, although first order in nature, does allow the prediction of the crust anchoring time and location for comparison with test results such as those obtained in the Melt Attack and Coolability Experiment (MACE) program [15, 60, 61]. Moreover, the model allows the prediction of the upwards heat flux both before and after separation. This allows the model to be more rigorously validated against test data, which increases the confidence level when the model is extrapolated to plant conditions.

2.4 CORQUENCH VALIDATION

Although there have been both low- and high-temperature simulant material core-concrete interaction and debris coolability experiments reported in the literature, the CORQUENCH validation efforts have focused primarily on oxidic reactor material experiments due to the fact that the code does not currently possess the capability to import or evaluate the complete set of thermo-physical property data that would be needed to adequately calculate simulant material experiments. Secondly, the code does not possess the capability to calculate density-driven phase segregation as is required to model experiments in which segregation occurs (e.g., tests with iron-alumina thermite).

On these bases, the tests shown in Table 2 were utilized in the code validation exercise. The matrix includes both 1-D and 2-D experiments; tests conducted with siliceous, limestone-common sand (LCS), and limestone-limestone (LL) concrete; and tests carried out under both wet and dry cavity

Table 2. Summary of CORQUENCH Validation Experiments

Program	Test	Concrete Type	Cavity Configuration (size)	Melt Gen. Tech.	Corium composition	Cladding Oxidation (%)	Initial Melt Depth	Cavity Cond.
ACE Phase C	L2	Siliceous	1-D rectilinear (50 cm square)	DEH	PWR	70	15 cm	Dry
	L4	Soviet	″	″	BWR	50	″	″
	L5	LCS	″	″	PWR	100	″	″
	L6	Siliceous	″	″	PWR	30	″	″
	L8	L-L	″	″	PWR	70	″	″
NRC-SNL	SURC1	L-L	1-D cylindrical (40 cm dia.)	Embedded Heaters	PWR	70	20 cm	″
	SURC2	Siliceous	″	″	PWR	70	″	″
MACE	M0	LCS	2-D rectilinear (30 cm square)	DEH	PWR		15 cm	Wet
	M1b	LCS	1-D rectilinear (50 cm square)	″	PWR		25 cm	″
	M3b	LCS	1-D rectilinear (120 cm square)	Thermite	BWR	100	20 cm	″
	M4	Siliceous	1-D rectilinear (50 cm square)	″	BWR	100	30 cm	″
OECD-MCCI	CCI-2	LCS	2-D rectilinear (50 cm square)	″	BWR	100	25 cm	Dry, late flooding
	CCI-3	Siliceous	″	″	BWR	100	″	″
	CCI-4	LCS	2-D rectilinear (50 cm x 40 cm)	″	BWR	78	″	Dry[a]
	CCI-5	Siliceous	2-D rectilinear (50 cm x 79 cm; one ablatable wall)	″	BWR	100	″	Dry[b]
	CCI-6	Siliceous	2-D rectilinear (70 cm square)	″	BWR	100	28 cm	Wet

[a]This experiment was flooded late, but the presence of an impervious mantle crust that formed in the upper region of the test section prior to cavity flooding prevented the coolant from contacting the underlying melt. Thus, this test was effectively a dry experiment.

[b]This experiment was not flooded due to the fact that the offgas system plugged early in the experiment sequence.

conditions. Only experiments for which sufficient open-literature data were available to set up an adequate model were included in the matrix. Finally, only tests that ran for a fairly significant length of time (or ablation depth) were calculated so that the ability of the code to predict longer-term behavior could be assessed. In terms of dry cavity experiments, the matrix includes five tests conducted as part of the ACE/MCCI test series [62-63] at Argonne National Laboratory, two tests conducted as part of the SURC test series carried at Sandia National Laboratory [64], and finally two tests conducted as part of the OECD/MCCI-2 program [65] at Argonne. In terms of wet cavity tests, the matrix includes four tests conducted as part of the MACE program [60-61] at Argonne National Laboratory, two tests conducted as part of the OECD/MCCI-1 program [66-68], and finally a single large scale integral test featuring early cavity flooding that was carried out as part of the OECD/MCCI-2 program [65].

The approach for the validation activity was to make a common set of user-specified modeling assumptions, and to apply those assumptions for all the tests that were analyzed. This method illustrates the ability (or lack thereof) of the code to match test results without tuning code input. The common set of modeling assumptions that were made as part of the validation exercises were also employed in the Unit 1 analyses that are provided in Section 4. A complete description of the validation calculations carried out in support of CORQUENCH development can be found in [12].

To illustrate the predictive capability of the code, results of the validation calculations for the MACE M1b experiment [60, 61] are provided here. As shown in Table 2, the test geometry consisted of a 1-D limestone-common sand crucible with a 50 cm x 50 cm basemat surface area. Water was added 14 minutes after the core-concrete interaction began. The melt temperature, ablation front location, and upwards heat flux predictions are compared with the test data in Figures 5 through 7, respectively, while the evolution of the various surface elevations is shown in Figure 8. The overall trends in the melt temperature and ablation front location are in reasonable agreement with the data, although the magnitudes are slightly higher than observed. The model predicts bulk cooling from 14 to 27.2 minutes, at which time a stable crust forms at the interface, and water ingression into a growing crust begins soon after. Continued crust growth leads to crust anchoring at 30.1 minutes, with subsequent melt-crust separation at 40.7 minutes. This separated state is predicted to remain for the balance of the test. Melt eruptions lead to particle bed formation from 27 to 41 minutes.

The overall trend in the heat flux curve again seems to follow the trend of the experiment data both before and after separation occurs, although the magnitudes during both phases are somewhat under-predicted. The analysis suggests a posttest debris configuration that includes an anchored crust that is 3.7 cm thick with an intervening gap of 4.8 cm. The overlying particle bed is predicted to have a mass of 21.9 kg. For comparison, the actual configuration consisted of a 5-6 cm thick crust with an underlying gap of 9 cm. The total particle bed mass was ~ 15 kg. Thus, for this test the crust thickness is under-predicted while the particle bed mass is over-predicted. Part of the disparity may be attributed to the fact that the model predicts slightly earlier melt-crust separation when compared to the test data. Separation leads to termination of the water ingression and melt eruption cooling mechanisms according to the current model.

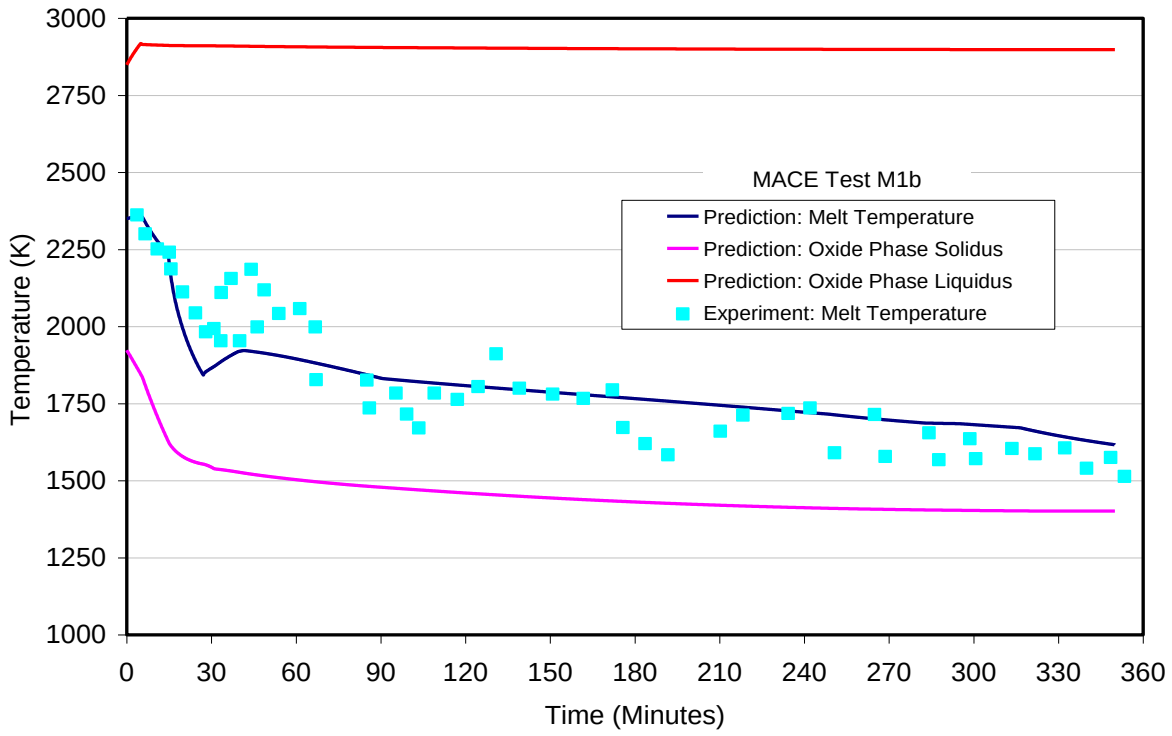

Fig. 5. Melt Temperature Prediction for MACE M1b.

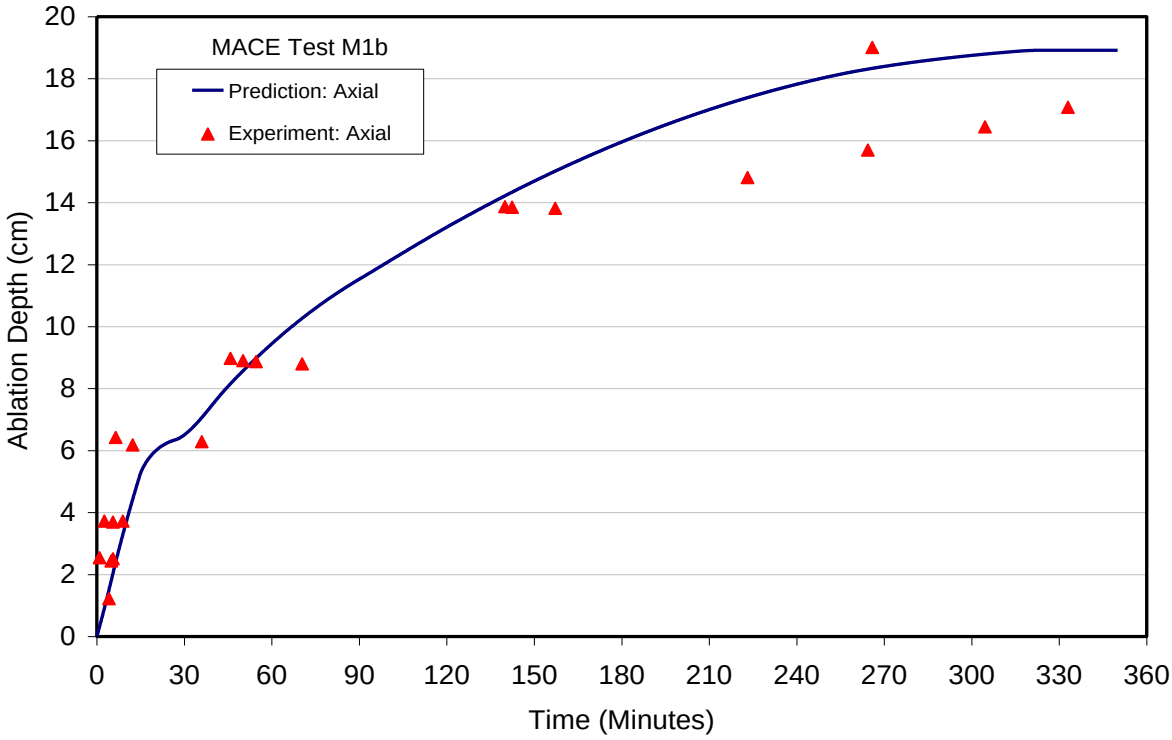

Fig. 6. Ablation Front Location Prediction for MACE M1b.

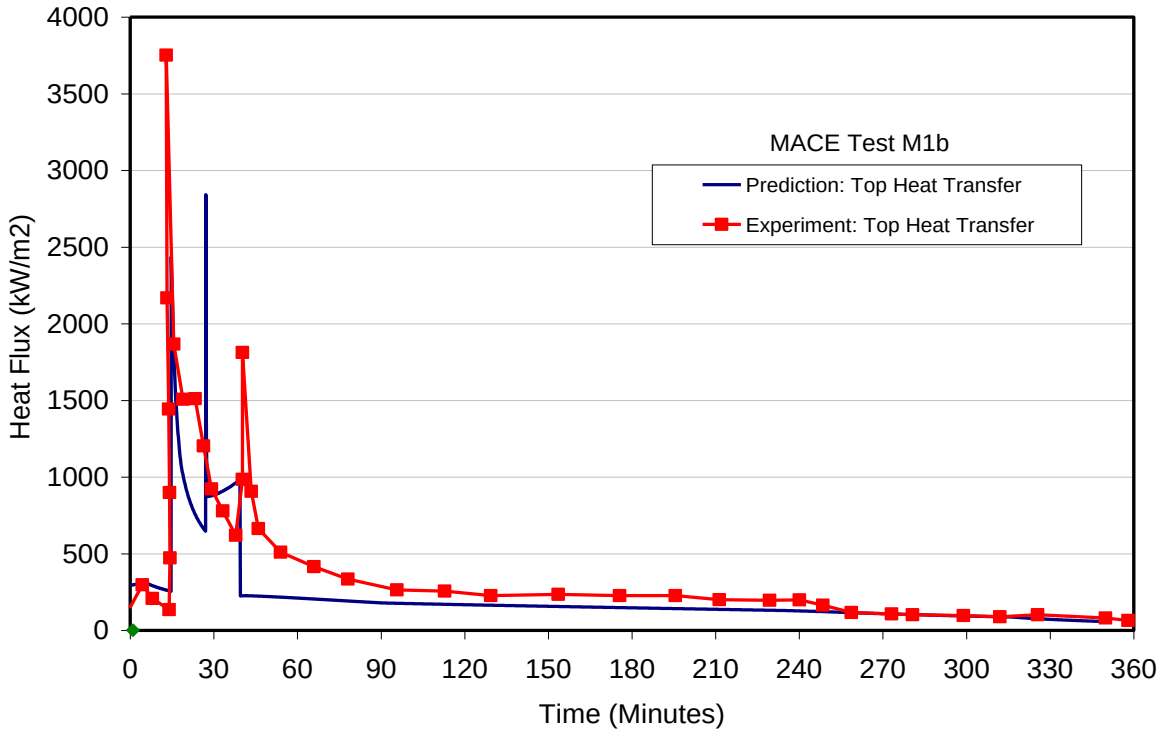

Fig. 7. Melt-Atmosphere Heat Flux Prediction for MACE M1b.

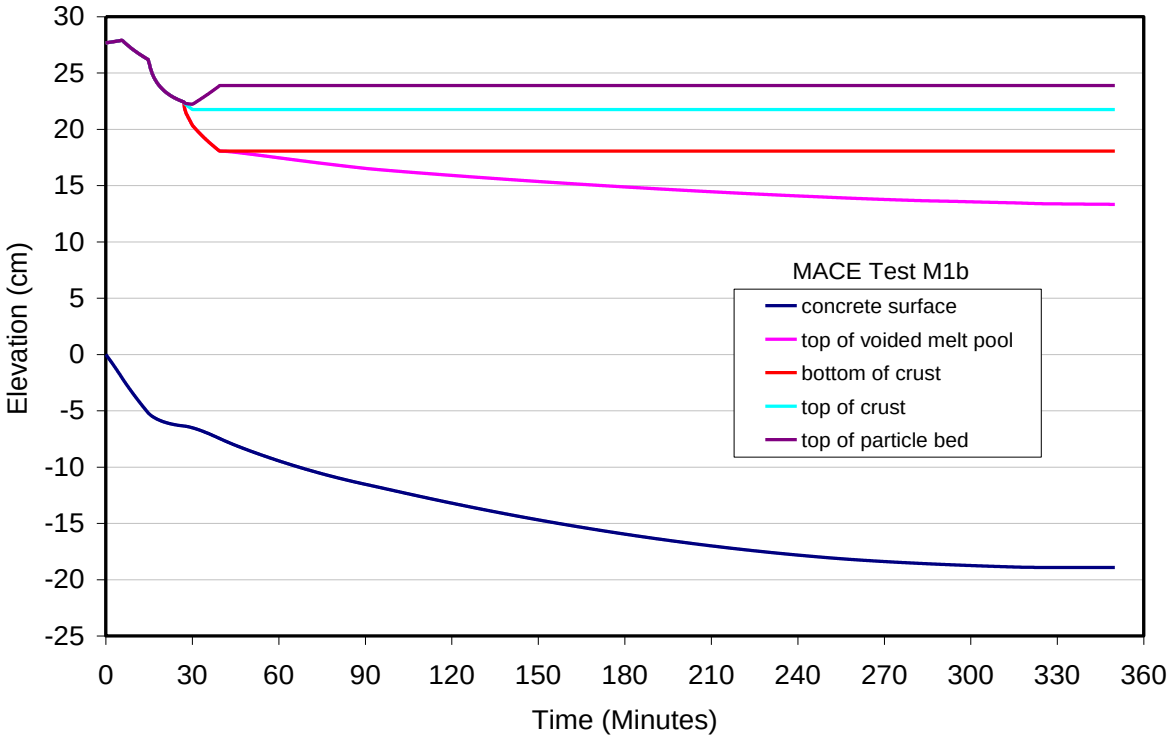

Fig. 8. Surface Elevation Predictions for MACE M1b.

3. MELTSPREAD ANALYSES OF CORE DEBRIS SPREADING

3.1 SUMMARY OF CASE SCENARIOS AND MODELING ASSUMPTIONS

The MELCOR v2.1 and MAAP5 codes were independently exercised under support from DOE-NE/NRC and EPRI, respectively, to evaluate the overall plant response for Fukushima Daiichi Unit 1 during the accident sequence that was initiated on 11 March 2011, [1, 2]. These analyses were carried out up through the point of reactor vessel failure and discharge of the core melt into the reactor containment. The code results thus provided the time-dependent melt pour rate, temperature, and composition as the material relocates ex-vessel. This information was used to carry out MELTSPREAD analyses in order to evaluate the progression of the accident once the core melt fails the reactor vessel. Key input data for the spreading analyses deduced from MELCOR and MAAP5 output are summarized in Table 3.

The MELCOR scenario [1] is a low-pressure sequence in which the vessel is predicted to fail at low pressure at14.27 hours, leading to the gradual discharge of ~ 141 metric tons (MT) of core debris into the drywell over the course of 67 minutes. MELCOR predicts the water depth in the drywell to be ~55 cm at onset of the pour [69]. The cumulative mass of relocated core debris as the sequence progresses is shown in Figure 9. The debris pour rate is highest right after the vessel fails, averaging 0.205 MT/sec (~ 0.028 m^3/sec) over the first seven minutes of the transient. The balance of the material (53 MT) relocates over the following hour at varying rates, all of which are less than the initial rate. The debris temperature distribution in the lower head just before the vessel fails ranges from 1850 to 2100 K [70]. For the purposes of this analysis, an average core debris temperature of 1975 K is assumed. The core melt composition (see Table 3) consists primarily of core oxides (UO_2-ZrO_2) with ~ 43% of the cladding oxidized. The debris contains ~ 20 wt% structural steel. Given the core debris temperature range predicted by MELCOR for this scenario, the metal phase is predicted to be fully liquid, while the oxide is predicted to be fully solid. The resultant solids content in the core debris at the time of vessel failure is thus estimated to be ~ 56 vol% (see Table 3). The melt is expected to be quite viscous with this amount of solids present. The decay heat level in the debris at the time of vessel failure (14.27 hours) is equivalent to 86 W/kg fuel [1].

The MAAP analyses [2] consider both low-pressure (MAAP-LP) and high-pressure (MAAP-HP) scenarios (Table 3). The 'low-pressure' and 'high-pressure' designations refer to the RPV pressure at the time of vessel failure. For the low-pressure case, the vessel is predicted to fail at low pressure at 10.11 hours, leading to rapid discharge of ~140 MT of core debris into the drywell over a time interval of ~ 18 seconds. The predicted water depth in the drywell for the low-pressure sequence is ~ 20 cm at onset of the pour [2]. The cumulative mass of relocated core debris as the sequence progressed for this case is shown in Figure 10. The average pour rate over the 18 second relocation transient is ~ 8 MT/sec (~1.1 m^3/sec), which is ~40 times larger than the flow rate predicted by MELCOR. The debris temperature at the time the vessel fails is 2751 K [2]; thus, the melt is superheated by ~160 K relative to the oxide phase liquidus. As for the MELCOR case, the core melt composition (see Table 3) consists primarily of core oxides (UO_2-ZrO_2), but with slightly less cladding oxidation (i.e., 39 % vs. 43 % for MELCOR). The debris also contains ~ 20 wt% structural steel, but MAAP predicts much higher structural steel oxidation than MELCOR leading to the presence of ~11 MT of iron oxide (FeO) in the melt. This constituent acts (at least according to the CORQUENCH property models based on data) to suppress the oxide phase solidus temperature by ~300 K relative the MELCOR melt composition. As noted earlier, the melt is superheated with respect to both the oxide and liquid phases, and so the core debris is completely fluid during relocation from the RPV to the drywell floor. This case can be contrasted with the MELCOR melt pour stream that contains a nominal solid content of 56 vol%. Decay heat in the debris at the time of vessel failure at 10.11 hours is equivalent to 96 W/kg fuel.

Table 3. Melt Spreading Input Data from MELCOR [1] and MAAP5 [2] Accident Analyses

Case Designator	MELCOR	MAAP-LP	MAAP-HP
Sequence description	Vessel failure at low RPV pressure	Vessel failure at low RPV pressure	Vessel failure at high RPV pressure
Onset of Pour (hours)	14.27	10.11	8.14
Pour Duration (sec)	4030	17.5	5.3
Containment Pressure (MPa)[b]	0.75	0.75	0.75
Water level on drywell floor at vessel failure (cm)	55	20	0
Melt Pour Temperature (K)	Range: 1850-2100 Average: 1975	2751	2797
Oxide Phase Solidus-Liquidus Temperatures (K-K)[a]	2215-2467	1934-2588	1925-2587
Metal Phase Solidus-Liquidus Temperatures (K-K)[a]	1705-1735	1802-1812	1803-1813
Melt Solid Fraction at Temperature (-)[a]	0.56	0.0	0.0
Decay Heat at Relocation (W/kg fuel)	86	96	105
Total Pour Mass of Melt Constituent (kg)			
UO_2	69400	76153.2	76153.4
Zr	25800	16594.1	16616.0
ZrO_2	16600	14141.5	14112.7
Cr	5900	1135.9	1099.4
Cr_2O_3	30	2732.0	2765.5
Fe	20430	16095.1	15928.4
FeO	230	11210.5	11369.5
Ni	2530	555.7	534.8
NiO	30	1208.2	1229.1
B_4C	0	502.0	502.0
Total	140950	140328.3	140310.8

[a]Calculated with CORQUENCH subroutines given composition and melt pour temperature;
[b]approximate, based on plant data.

As shown in Table 3, for the MAAP-HP scenario, the vessel is predicted to fail at high pressure earlier (i.e. at 8.14 hours) in the sequence. Melt pour mass and composition for this case is very similar to the low-pressure scenario, with the exception that the melt is more highly superheated (i.e. 210 K vs. 160 K). The pour rate for this case is quite large (Figure 11), ~26.5 MT/sec (~3.6 m^3/sec), which is roughly three times higher than the low-pressure sequence. There is one additional significant difference between the low and high pressure cases; i.e., the drywell is predicted to be dry during relocation for the high pressure case. Decay heat in the debris at the time of vessel failure is slightly higher than the low-pressure case (viz. 105 W/kg fuel) due to earlier melt release in this sequence.

In terms of the cavity characteristics, the Fukushima Daiichi Unit 1 containment is a Mark I design. Internal to the pedestal, there are two drywell sumps, each of which is rectilinear in cross section (1.45 m by 1.45 m) and 1.2 m deep. During normal operations, the sumps are covered with steel plates that are 6.35 mm (1/4") thick. The centerline of each sump is offset by 1.47 m from the pedestal axial centerline. The internal radius of the pedestal wall is 2.5 m, and the pedestal wall thickness is 1.2 m. There is a single doorway from the pedestal to the drywell annulus that is 1.0 m wide. The radius of the drywell liner is 6.55 m where the liner contacts the drywell floor. The steel liner is 2.5 cm thick.

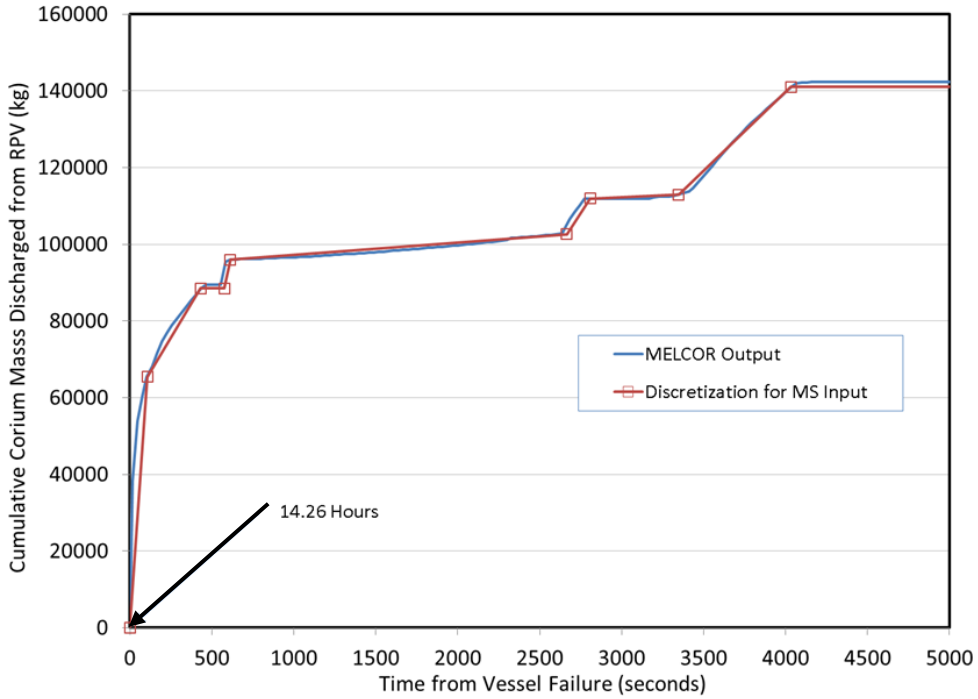

Fig. 9. Cumulative Core Debris Discharge from RPV for MELCOR Sequence [1].

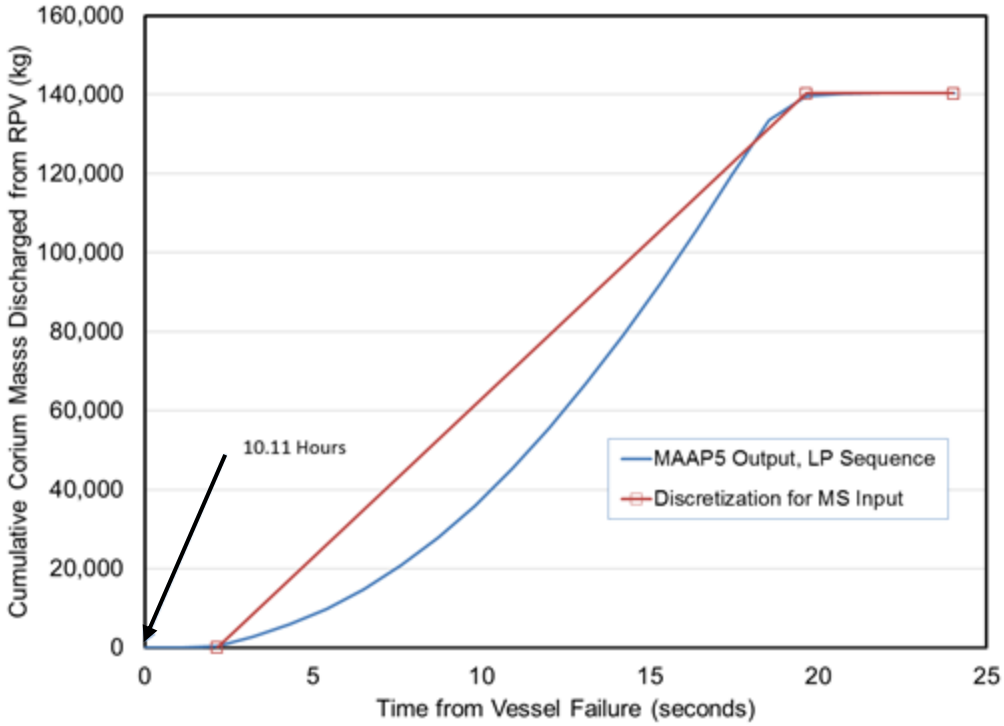

Fig. 10. Cumulative Core Debris Discharge from RPV for MAAP-LP Sequence [2].

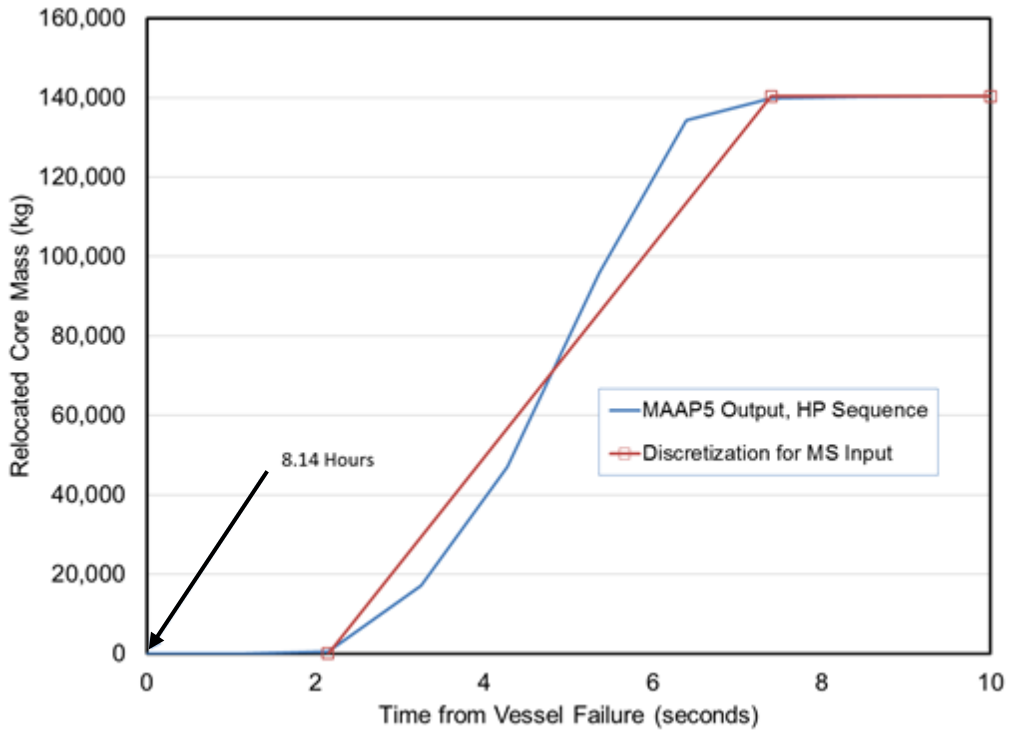

Fig. 11. Cumulative Core Debris Discharge from RPV for MAAP-HP Sequence [2].

Due to the one-dimensional modeling limitations of the code, the two drywell sumps are combined into a single geometric entity that consists of cylinder located at the pedestal centerline that is 2.23 m in diameter and 1.2 m deep. Thus, in the nodalization process the sump volume, cross-sectional areas, and depth are conserved. Core material relocating from the reactor pressure vessel is assumed to drain into the sump region; whether or not the sump plates are initially present is treated parametrically (parametric cases discussed later in this section). The balance of the drywell floor from the sump edge to the pedestal inner wall is discretized into 13 cylindrical mesh cells with a uniform radial incremental thickness of 10.1 cm. Once the melt reaches the interior surface of the pedestal, the melt material is assumed to flow through the pedestal doorway; this area is treated as a one-dimensional channel. The 1.2 m flow distance is discretized into 12 nodes of equal size (10 cm). Outside the pedestal doorway, the core melt is assumed to spread in a 90º sector to the liner. The total distance of 2.85 m from the pedestal outer wall to the drywell liner is discretized into 28 nodes of equal size (10 cm). After the melt contacts the liner, the flow is assumed to be diverted symmetrically into the two sides of the annulus. A courser discretization was used in the annulus; i.e. 28 nodes were used to model this area resulting in a uniform cell size of 47 cm long by 5.7 m wide (5.7 m is equivalent to twice the drywell annulus thickness, which is based on symmetrical flow diversion outside the pedestal doorway).

MELTSPREAD is equipped with a subroutine that can calculate the heat-up of the drywell liner due to impingement heat transfer from the relocating melt by solving the two-dimensional transient heat conduction equation in the liner, including the effects of transient crust growth on the liner surface. To this end, the 2.5 cm thick liner is discretized into 5 mesh cells of 5.0 mm size perpendicular to the liner surface, and 60 cells that are 1 cm long (60 cm total length) parallel to the liner surface. The liner is assumed to be inclined at an angle of 45º with respect to vertical where it makes contact with the drywell floor (this assumption is important since it affects the length of the liner covered by melt given the actual depth of material adjacent to the liner). The heat transfer coefficient from the melt to the liner surface is conservatively modeled as the sum of forced convection (i.e., slot jet impingement; see Martin [71]) and bubble-driven recirculation (see Theofanous et al. [72]) correlations. Conversely, if the debris solidifies

adjacent to the liner, then the long-term heat transfer is evaluated using a simplified 1-D heat transfer model from the debris to the liner.

In all Mark I plants known to the authors, there is a substantial amount of equipment located on the drywell floor in the annulus region. This equipment obviously can divert spreading materials and affect (i.e. restrict by forming local blockages) the overall spreading behavior. The presence of this equipment can be modeled by appropriately reducing flow areas and spreading arc lengths in the spreading mesh at positions where the equipment is positioned, but details of equipment locations and sizes in the annulus of Unit 1 were not know at the time this work was carried out. Thus, this effect is neglected in the current analysis. The additional hydraulic flow resistance provided by this equipment may reduce the overall spreading areas predicted in the current analyses.

Below-vessel structure is extensive in BWRs, primarily consisting of control rod drives and instrument tube penetrations, as well as a catwalk for personnel access to this equipment. These structures may impact the melt relocation behavior, causing flow diversion and possibly creating a rain-drop effect that can reduce impingement heat transfer. A detailed analysis of this type of behavior is beyond the current scope of work. A previous analysis, for two melt pour scenarios different from the current scenarios, found that these lower structures do not have a dominating effect on the melt relocation behavior [82]. As such, the melt is assumed to relocate directly into the drywell sump (modeled as a single discrete mesh cell), and spread from there.

Water present on the drywell floor as an initial condition can also affect spreading behavior by leading to melt jet fragmentation and cooling prior to impact with the drywell floor. This type of interaction would reduce the ability of the core debris to spread. MELTPREAD does not currently contain models that can calculate debris fragmentation and cooling as the debris relocates from the RPV through a water pool, and so the code is expected to over-estimate the spreading potential for sequences when substantial water is present on the drywell floor. In addition, the code does not have a water heat-up and boil-off model, and so for situations in which a limited amount of water is present, the code will over-predict the cooling behavior compared to situations in which the inventory can boil off and uncover previously cooled debris. However, both wet and dry scenarios are considered as part of the parametric spreading analyses, and so potentially water-starved cases would be bounded by these two cases.

Although the concrete used in the construction of the Fukushima Daiichi plants is of the siliceous type, the exact composition is not known. To be consistent with the previous MELCOR analyses [1], the composition was chosen to be the same as the default Basalt concrete composition (a form of siliceous concrete that can be specified as part of the CORCON Mod 3 module that is embedded in MELCOR [14]; see Table 4).

Table 4. Siliceous Concrete Composition Assumed in Analyses (CORCON Mod3 basalt [14])

Constituent	Wt%
SiO_2	54.84
CaO	8.82
Al_2O_3	8.32
K_2O	5.39
Fe_2O_3	6.26
TiO_2	1.05
MgO	6.16
Na_2O	1.8
H_2O	5.86
CO_2	1.5

Other important modeling assumptions are summarized as follows. The convective heat transfer coefficient from the melt to the surface of the core debris is calculated using the well-known Dittus-Boelter forced convection heat transfer correlation with the hydraulic diameter based on local melt depth. This is the same modeling option that was used in the MELTSPREAD code validation exercise [18]. With this assumption the code is expected to provide a best estimate of the melt penetration distance into the drywell, but this will result in an under-prediction of the extent of core-concrete interaction in the longer term after spreading ceases and convection is driven by non-condensable gas generation from core-concrete interaction. This is not expected to be a major issue for the MAAP sequences that are characterized by rapid melt pour rates and relatively short spreading transients. However, for the relatively gradual MELCOR pour conditions, the extent of basemat attack and combustible gas generation may be under-predicted. Aside from the use of the Dittus-Boelter correlation, the empirical constant in the Ramacciotti viscosity correlation [25], Eq. (1), is set to the best-estimate value deduced on the basis of the code validation exercise (i.e., $C_R = 7.26$) in all analyses carried out as part of this study. This assumption is again consistent with providing best-estimates of melt penetration distance in the drywell.

Aside from these assumptions, the containment pressure was assumed to be ~0.75 MPa for all sequences. Plant measurements fluctuated around this value after 13 hours and data are essentially non-existent prior to 10 hours [1], and so the pressure is set at this value in lieu of better information. Water depth on the drywell floor was a parameter in this study, but in all wet cases the water was assumed to be at saturation temperature corresponding to cavity pressure (441 K). For dry situations, the debris is cooled by radiation heat transfer to structures in the upper cavity that are assumed to have an emissivity of 0.3 (typical of steel). In this case, the boundary temperature is also assumed to be at containment saturation temperature. MELTSPREAD currently does not model heat-up of overlying structure during the spreading transient. Thus, the use of the low radiation boundary temperature (441 K) is roughly equivalent to assuming radiation heat transfer to an infinite heat sink. The time step for all cases was taken equal to 10 ms which has been shown to provide highly converged results in these types of studies. Given the input data (Table 3) and modeling assumptions (described above), several parametric cases were evaluated for each sequence in order to examine the sensitivity of the spreading behavior on several factors. The six cases that were calculated for the MELCOR sequence are summarized in Table 5, while the four cases that were calculated for both the MAAP low- and high-pressure sequences are summarized in Table 6 and Table 7, respectively. A common base case scenario was established early in the process in order to provide a technical basis for systematically examining parametric effects. Subsequent discussions and interaction with the individuals who carried out the MELCOR [1, 69] and MAAP [2] analyses provided a technical basis for selecting 'best estimate' cases from the calculation matrices based on expected conditions (principally water depth on the drywell floor) at the time of vessel failure. These best estimate cases are identified during the results presentation in the next section.

The base case for all three scenarios assumes that water is initially present on the drywell floor, and that the depth is limited by the vent line height that is assumed to be 60 cm. Thus, for situations in which local debris depth is larger than 60 cm, the debris cools by radiation to structures in the upper cavity region. However, if the melt depth falls below the vent line height, the material is assumed to be cooled by heat transfer to overlying water (MELTSPREAD utilizes a full boiling curve). The sump cover plates are quite thin (6.4 mm, or ¼") and if they do not fail by impingement heat transfer, the ability of these plates to withstand the immense mechanical load of the core debris is questionable. Thus, the base case assumes that the plates fail upon initial contact with the core debris. Thereafter, melt accumulates in the sumps until the height exceeds the sump depth (1.2 m), and thereafter the debris will start to spread on the pedestal floor.

MELTSPEAD has the ability to analyze thermal heat up and ablation of the sump cover plates as a modeling option. The structural support system for these thin plates is not known, and so early mechanical failure cannot be assumed for all situations. Thus, case two for all three scenarios utilizes the sump cover heat up and ablation model to determine if the plates are predicted to fail by impingement heat transfer, and if not what is the effect of debris relocation over these plates on the spreading behavior. The third case is equivalent to the first case, but the cavity is assumed to be dry during relocation. Thus,

this case examines the effect of a wet vs. dry cavity floor on the spreading behavior. The fourth case is equivalent to the first case, but the water depth on the drywell floor is reduced to ½ the vent line height (i.e. 30 cm). Thus, cases 1, 3 and 4 together parameterize on the water depth during the spreading transient, ranging from initially dry to the situation in which the depth is limited by the vent line height.

Table 5. MELTSPREAD calculation matrix: MELCOR scenario with RPV failure at 14.27 hours

Case No.	Description/Rationale	Parameter Investigated
MELCOR-1	Utilizes MELCOR time-dependent pour over 4030 seconds. Melt relocates into containment at drywell pressure of 0.75 MPa. Average melt temperature of 1975 K assumed (varies between 1850 and 2100 K during relocation [70]). Water initially present on drywell floor and the level is limited by the vent line height of 60 cm. The thin (6.3 mm) sump plates are assumed to fail at pour inception, leading to early melt accumulation in the sump.	Base case in which sump plates are assumed to fail and water level in the drywell is limited to the vent line height.
MELCOR-2	Same as Case 1, but the sump plates remain intact during pour (MELTSPREAD analysis predicts insufficient thermal loading to fail the plates over the pour duration, but the code does not perform a mechanical load limit analysis).	Effect of melt retention in sump on spreading: the sump plates remain intact and so melt spreading starts at pour inception.
MELCOR-3	Same as Case 1, but the cavity is assumed to be dry at the time of vessel failure. It is not completely clear that there was coolant leakage into containment before RPV failure (aside from steam venting into torus through the SRVs).	Effect of water on spreading behavior: no water present
MELCOR-4	Same as Case 1, but the water level in the cavity is assumed to be limited to ½ the vent line height (i.e. 30 cm) at the time of vessel failure.	Effect of water on spreading behavior: only 30 cm present on floor
MELCOR-5	Same as Case 1, but melt is assumed to accumulate in lower head and relocate in 10 seconds. Melt release rate from the vessel is a modeling uncertainty.	This case examines the effect of pour flow rate on spreading behavior.
MELCOR-6	Same as Case 2, but melt is assumed to accumulate in lower head and relocate in 10 seconds.	This would be a worst case scenario for liner failure based on low temperature MELCOR melt pour conditions.

Table 6. MELTSPREAD calculation matrix: MAAP low pressure (LP) scenario with vessel failure at 10.11 hours

Case No.	Description/Rationale	Parameter Investigated
MAAP-LP-1	Utilizes MAAP LP sequence core inventory pour data over 17.5 seconds. Melt relocates into containment at drywell pressure of 0.75 MPa. Core debris temperature at time of vessel failure is 2751 K [2])). Water initially present on drywell floor and the level is limited by the vent line height of 60 cm. The thin (6.3 mm) sump plates are assumed to fail at pour inception, leading to early melt accumulation in the sump.	Base case in which sump plates fail and the water level in drywell is limited to the vent line height.
MAAP-LP-2	Same as Case 1, but the sump plates are initially intact during pour (MELTSPREAD predicts rapid plate ablation and failure by 4.37 seconds for this scenario).	Effect of early melt retention in sump on spreading: the sump plates are initially intact and so melt spreading starts at pour inception.
MAAP-LP-3	Same as Case 1, but the cavity is assumed to be dry at the time of vessel failure. It is not completely clear that there was coolant leakage into containment before RPV failure (aside from steam venting into torus through the SRVs).	Effect of water on spreading behavior: no water present
MAAP-LP-4	Same as Case 1, but the water level in the cavity is assumed to be limited to ½ the vent line height (i.e. 30 cm) at the time of vessel failure.	Effect of water on spreading behavior: only 30 cm present on floor

Table 7. MELTSPREAD calculation matrix: MAAP high pressure (HP) scenario with vessel failure at 8.14 hours

Case No.	Description/Rationale	Parameter Investigated
MAAP-HP-1	Utilizes MAAP HP sequence core inventory pour data over 5.3 seconds. Melt relocates into containment at drywell pressure of 0.75 MPa. Core debris temperature at time of vessel failure is 2797 K [2])). Water initially present on drywell floor and the level is limited by the vent line height of 60 cm. The thin (6.3 mm) sump plates are assumed to fail at pour inception, leading to early melt accumulation in the sump.	Base case in which sump plates fail, and water level in drywell is limited to the vent line height.
MAAP-HP-2	Same as Case 1, but the sump plates are initially intact during pour (MELTSPREAD predicts rapid plate ablation and failure by 3.58 seconds for this scenario).	Effect of early melt retention in sump on spreading: the sump plates are initially intact and so melt spreading starts at pour inception.
MAAP-HP-3	Same as Case 1, but the cavity is assumed to be dry at the time of vessel failure. It is not completely clear that there was coolant leakage into containment before RPV failure (aside from steam venting into torus through the SRVs).	Effect of water on spreading behavior: no water present
MAAP-HP-4	Same as Case 1, but the water level in the cavity is assumed to be limited to ½ the vent line height (i.e. 30 cm) at the time of vessel failure.	Effect of water on spreading behavior: only 30 cm present on floor

As described earlier, the difference in the MELCOR and MAAP pour conditions vary considerably. The conditions range from a slow, gradual pour of a viscous low-temperature melt (MELCOR scenario) to the rapid pour of a superheated core material (MAAP scenarios). Thus, two additional cases were calculated for the MELCOR sequence in which a very rapid pour of a low temperature melt occurs over a compressed timescale of 10 seconds. This type of situation would be indicative of a lower head creep rupture scenario where the head weakens and eventually fails catastrophically, leading to rapid discharge of the core debris into the containment. Case 5 is the same as the base case, but with the pour duration shortened to 10 seconds. Case 6 is the same as case 5, but the sump cover plates are assumed to remain intact during relocation. Thus, case 6 is considered to be a worst case scenario for liner attack based on the MELCOR results.

3.2 MELCOR SPREADING RESULTS

To review, in this scenario the vessel fails at low pressure leading to gradual discharge of a predominately oxidic core melt into the drywell over a period of ~ 67 minutes (see Table 3 and Figure 12). The average pour rate is 0.205 MT/sec (~0.028 m^3/sec). The pour temperature is in the range where the metal phase is expected to be entirely liquid, while the oxide would be solid. According to the MELTSPREAD viscosity subroutine, the viscosity of the core debris is ~77 Pa-sec at the assumed vessel exit temperature of 1975 K, which is the same order-of-magnitude as chocolate syrup or ketchup.[1] Thus, in this scenario the flow is expected to be dominated by viscous effects.

For this case, the MELCOR analysis [69] indicates that the water depth on the drywell floor at the time of vessel failure is ~ 55 cm (Table 3). Thus, the best estimate calculation is selected to be the MELCOR-1 case (Table 5) in which the sump plates fail at initial contact with the core debris, and the material subsequently spreads under water at a depth that is limited by the vent line height of ~ 60 cm.

A series of plots showing the melt height and temperature distributions at various times following vessel failure for the MELCOR-1 case are provided in Figure 13. Additional plots describing the melt leading edge location and cumulative floor area coverage as a function of time for all six MELCOR cases are provided in Figures 12 and 14, respectively. Finally, Figure 15 provides snapshots in time of the melt spread distance, elevation and temperature as a function of position. The spreading path starts at the center of the pedestal (0 m) and extends out through the pedestal doorway to the pedestal wall (6.5 m). The path then arcs around the periphery of the drywell up to the point 180° opposite of the pedestal doorway.

Due to the relatively low pour rate and high viscosity, the melt gradually fills the sump volume and then begins to spread first in the pedestal region, and then out the pedestal doorway, making contact with the liner at ~182 seconds; see Figure 12. After contacting the liner the flow is diverted (symmetrically by assumption) into the annulus where the debris travels a small distance (~50 cm) before relocation is halted by freezing at the leading edge. This corresponds to the end of the spreading transient after the initial 7 minute pour phase; see Figure 12 and depth/temperature plot at 500 seconds in Figure 15. The debris profile at this point consists of a fairly uniform layer of molten material at a depth of ~ 23 cm over the pedestal floor; the material in the sump is ~ 143 cm deep due to the elevation difference.[2] Due to the high viscosity and low spreading velocity of the material, the local convective heat transfer coefficients are small. As a result, the code predicts essentially no concrete ablation during spreading (although there is concrete degasing due to local heat up in the thermal boundary layer).

---

[1] See e.g. http://en.wikipedia.org/wiki/Viscosity, accessed Nov, 2012.

[2] When core debris is predicted to locally solidify, MELTSPREAD immobilizes this material and incorporates it into the basemat nodalization scheme as solid material in contact with the concrete. When this step is performed, the code calculates the equivalent volume reduction by going from a solid to a liquid, and this is reflected as a reduced height of the solidified material (typically 20 %). This fact accounts for the height reduction in Fig. 15 between 500 and 700 seconds as the material solidifies outside the pedestal doorway. The instantaneous height reductions in the debris depth adjacent to the drywell liner in Figure 16 are due to the same modeling approach.

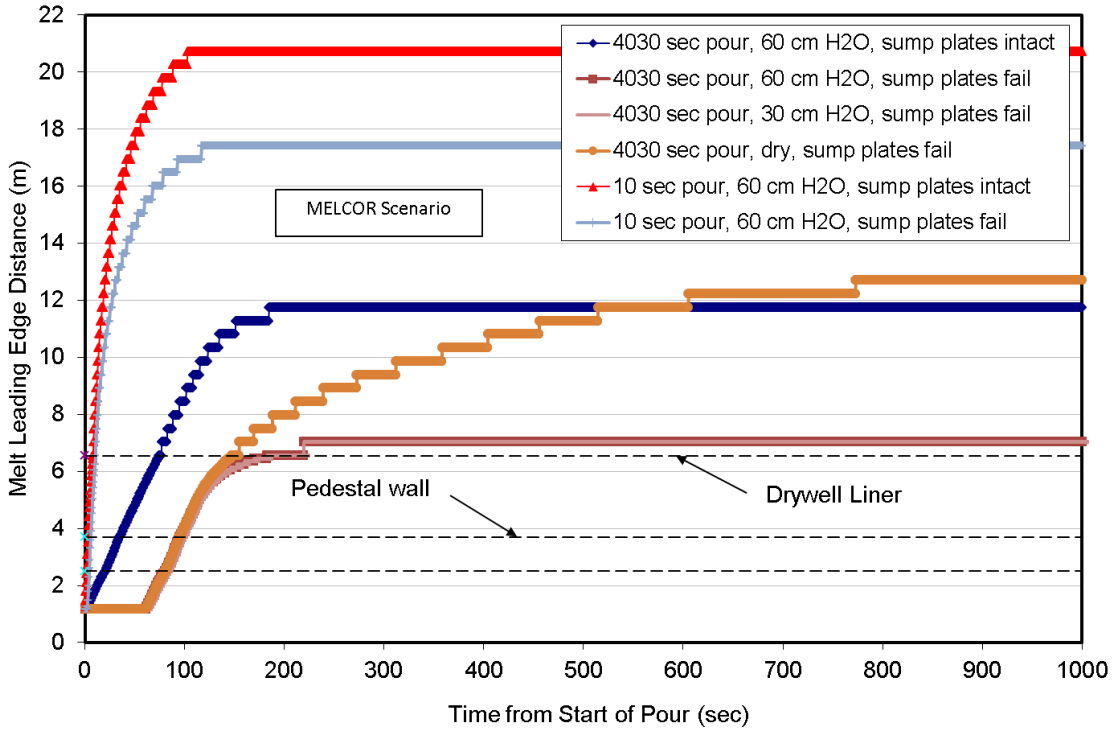

Fig. 12. Melt Leading Edge Penetration Rate for the MELCOR Parametric Cases.

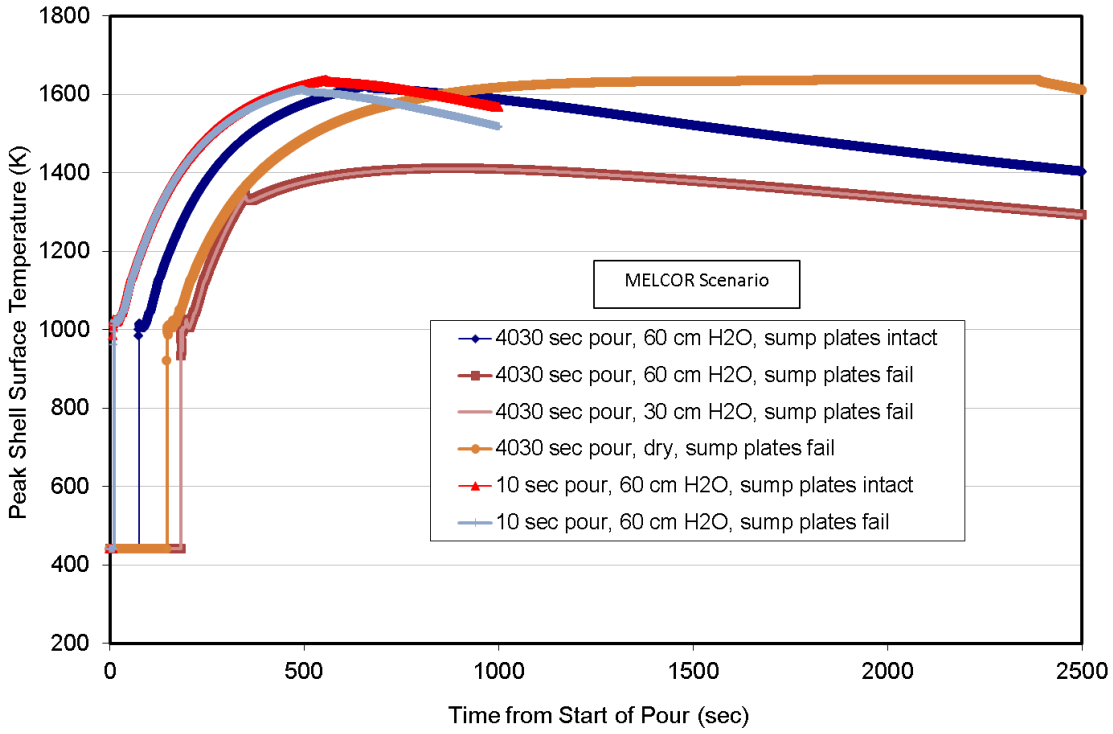

Fig. 13. Peak Liner Surface Temperature for the MELCOR Parametric Cases.

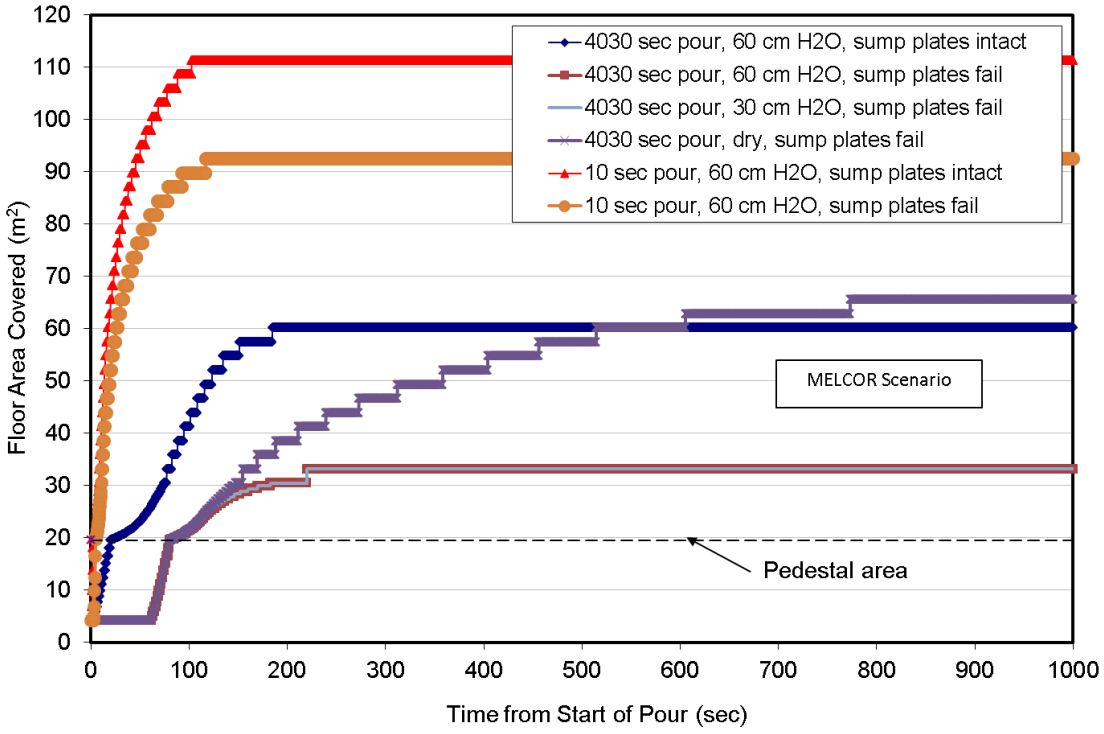

Fig. 14. Basemat Floor Area Covered by Melt for the MELCOR Parametric Cases.

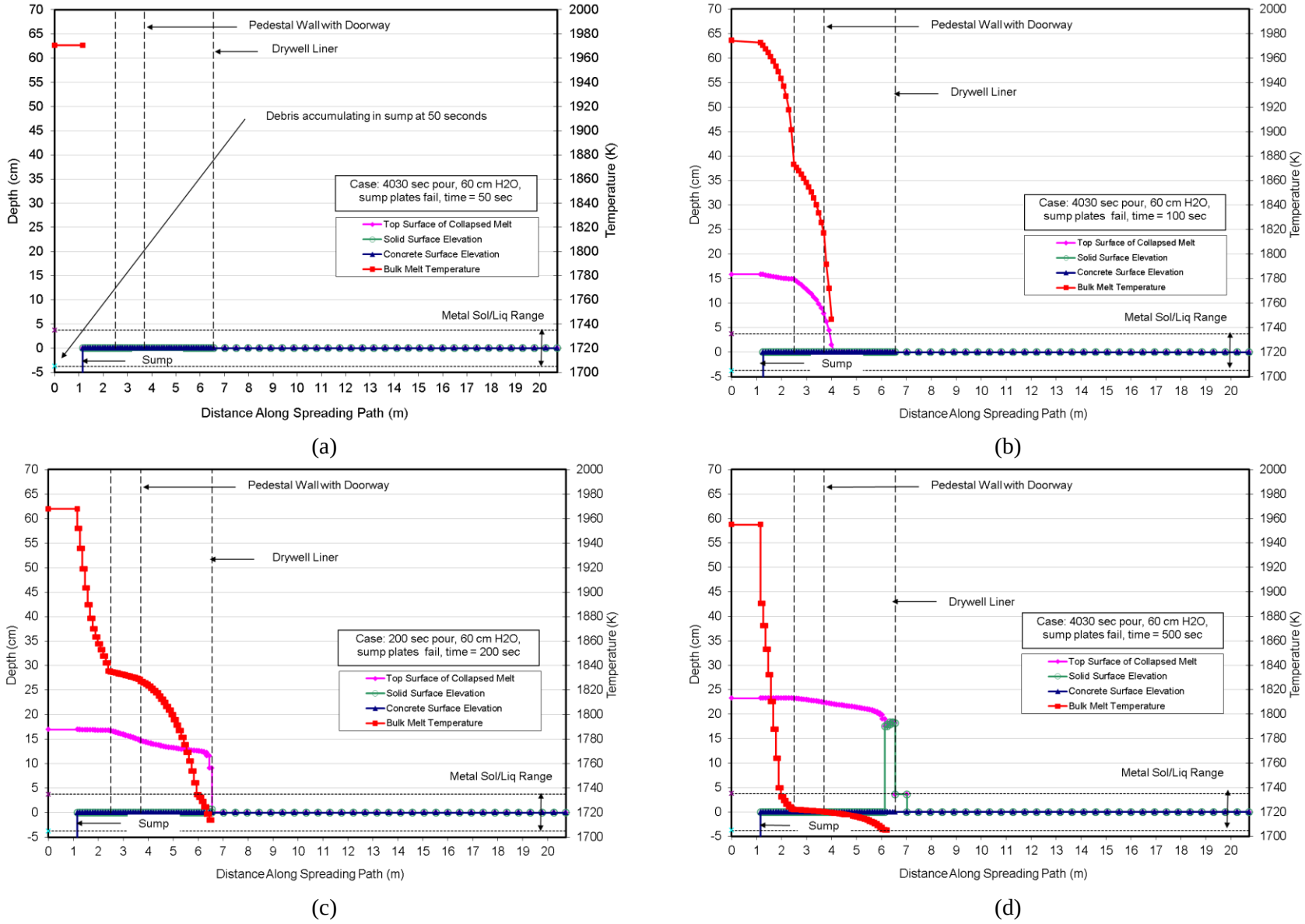

Fig. 15. (a-d) Melt Temperature-Depth Profiles at 50, 100, 200, and 500 sec for MELCOR Best Estimate Case.

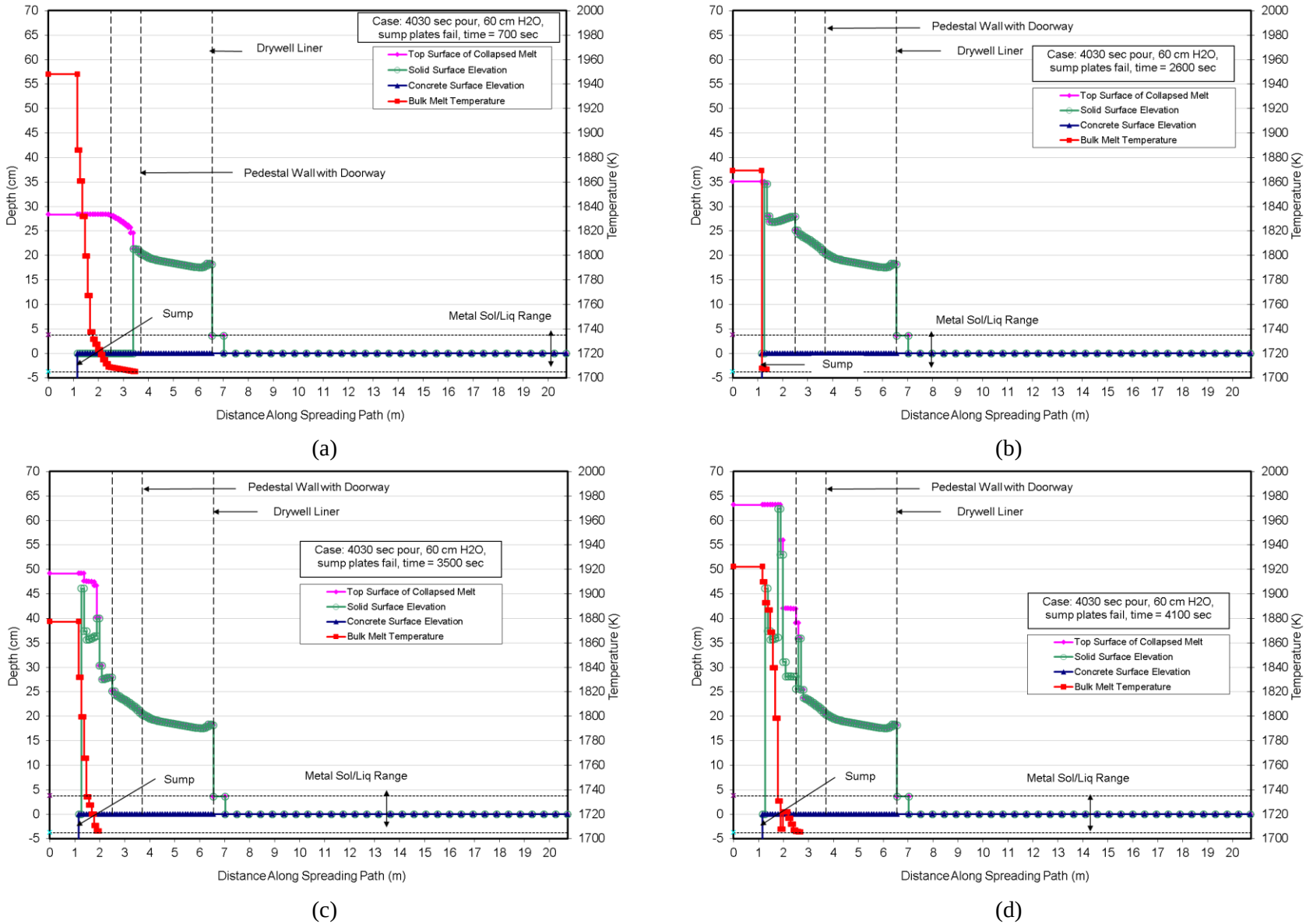

Fig. 15 (contd.). (a-d) Melt Temperature-Depth Profiles at 700, 2600, 3500, and 4100 sec for MELCOR Best Estimate Case.

Over the next 50 minutes, core debris gradually drains from the pressure vessel, and some of this material spreads out the pedestal doorway where it freezes over the previously frozen debris (see depth/temperature profiles in Figure 15 at 700, 2600, and 3500 seconds). However, the vast majority of this new material is retained as a molten pool inside the pedestal region. The final significant debris relocation transient of ~ 28 MT from 3500 to 4030 seconds leads to the accumulation of a mound of material in the pedestal that slightly exceeds the water height of 60 cm assumed for this scenario. The final debris configuration for the best-estimate MELCOR case is thus predicted to be a mound of material ~ 63 cm deep inside the pedestal, with a lesser amount of debris spread out the pedestal doorway and in contact with the drywell liner. As is shown in Figure 14 and Table 8, the final drywell floor area covered by core debris is ~ 33 m^2, which includes the sump.

The predicted core debris depth adjacent to the liner across from the pedestal doorway and the peak liner surface temperature are shown in Figures 13 and 16, respectively, for all six MELCOR cases. To provide additional detail regarding the liner heat up behavior, the liner surface temperature profiles for the best-estimate MELCOR-1 case are provided in Figure 17. (Recall that the liner is inclined at an angle of 45º with respect to vertical, and so the length along the liner covered by melt is equal to the square root of two times the local melt depth). Due to the low spreading velocity, the melt depth gradually increases adjacent to the liner. The liner surface temperature shows an early peak that is indicative of initial melt contact and crust growth to the quasi-steady equilibrium depth. Thereafter, the liner surface temporarily cools as heat is dissipated into the bulk of the steel. However, this heat sink is soon exhausted and the surface begins to heat up. Eventually, a quasi-steady condition is reached in which heat transfer from the melt is dissipated by conduction up along the liner where the heat is dumped to the overlying water by boiling heat transfer. The inflection point in the liner surface temperature response at ~330 seconds for the best estimate case (as well as the inflection points for the other cases) corresponds to the point where bulk solidification of the core debris next to the liner occurs. At this point, the heat transfer switches from convection from a melt pool to conduction-limited heat transfer from solidified debris, and so the liner surface temperature ramp is temporarily interrupted before reheating to a peak of ~1410 K at 850 seconds. Thereafter, the temperature steadily declines over the balance of the calculation. Thus, the liner is predicted to remain intact for this scenario by virtue of the fact that the melting point is not reached. However, this analysis does not consider other potential failure modes such as creep rupture.[3]

Examination of Figures 12 and 14 for the other three extended pour-duration MELCOR cases indicates that the overall spreading behavior is affected by the presence/absence of water on the drywell floor. For the dry cavity case, the final spreading area nearly doubles to 65.5 m^2 compared to the reference case. However, the depth of water in the range investigated (i.e. 30 cm vs. 60 cm) is not found to have a significant effect on the overall extent of spreading, although the depth of the debris retained in the pedestal was found to be reduced to ~ 50 cm for the MELCOR-4 (30 cm water depth) case. Somewhat surprisingly, the liner is predicted to remain intact for the dry cavity case, reaching a peak temperature of 1630 K at 2400 seconds (Figure 13). This is due to the fact that the debris depth adjacent to the liner is reduced to ~ 13 cm for the dry cavity case by virtue of the increased spreading area (Figure 16). For the case in which the plates are assumed to remain intact (MELCOR-2), the melt is predicted to make earlier contact with the liner (Figure 12), but the depth of the material adjacent to the liner (Figure 16) as well as the peak liner temperature (Figure 17) are quite close to the best estimate case. This is due to the fact that the spreading area is nearly doubled to 60.2 m^2 in this calculation, which apparently compensates for the lack of material retention in the sump.

[3] The liner creep rupture failure mode was investigated for a single accident scenario during the MARK-I liner attack study [3]. In this study, creep rupture occurred at a failure temperature of 1511 to 1583 K (95 percent confidence bounds), but the work was carried out for a single accident scenario. Creep is a function of time, temperature, and variations in heating rate, peak temperature, and extent of liner contact with core debris, which could affect the prediction of the liner failure temperature [3].

Table 8. Final Melt Spread Areas for MELCOR Cases

Case No.	Description/Rationale	Final spread area (m^2)
MELCOR-1	Water initially present on drywell floor and the level is limited by the vent line height of 60 cm. The thin (6.3 mm) sump plates are assumed to fail at pour inception, leading to early melt accumulation in the sump.	33.2
MELCOR-2	Same as case 1, but the sump plates remain intact during pour (MELTSPREAD analysis predicts insufficient thermal loading to fail the plates over the pour duration, but the code does not perform a mechanical load limit analysis).	60.2
MELCOR-3	Same as case 1, but the cavity is assumed to be dry at the time of vessel failure. It is not completely clear that there was coolant leakage into containment before RPV failure (aside from steam venting into torus through the SRVs).	65.5
MELCOR-4	Same as case 1, but the water level in the cavity is assumed to only be filled to half the vent line height (i.e. 30 cm) at the time of vessel failure.	33.2
MELCOR-5	Same as case 1, but melt assumed to accumulate in lower head and relocate in 10 seconds. Melt release rate from the vessel is a modeling uncertainty.	92.5
MELCOR-6	Same as case 2, but melt assumed to accumulate in lower head and relocate in 10 seconds.	111

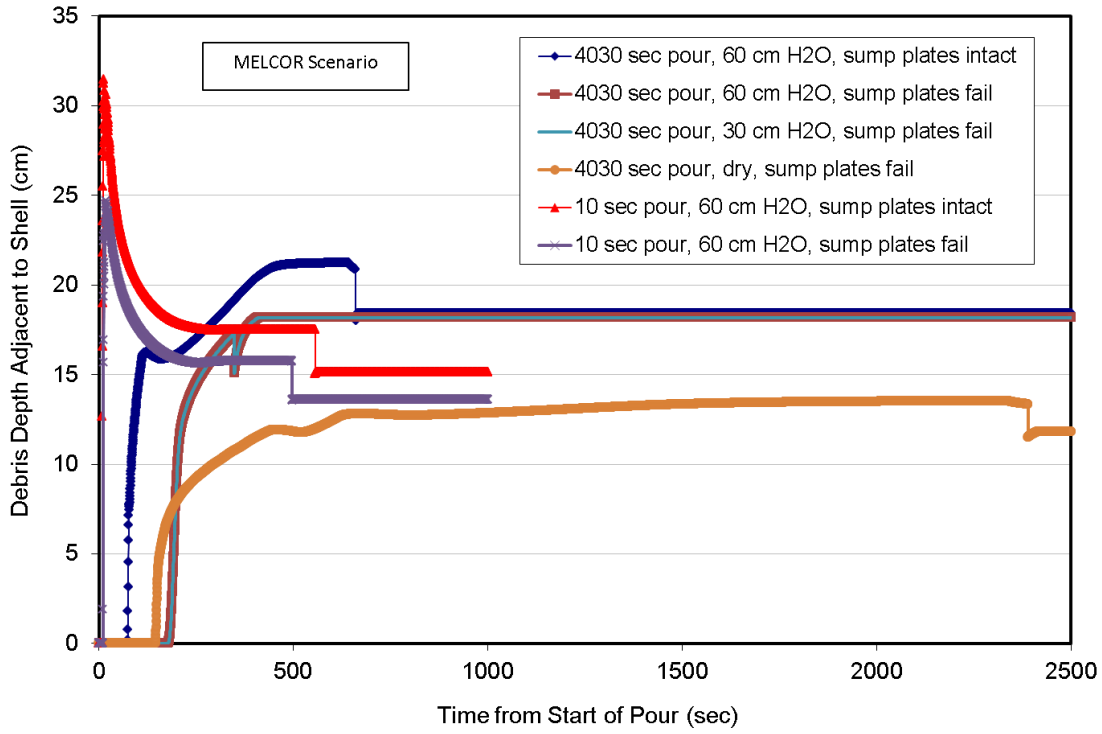

Fig. 16. Debris Depth Adjacent to the Drywell Liner Across from the Pedestal Doorway for the MELCOR Parametric Cases.

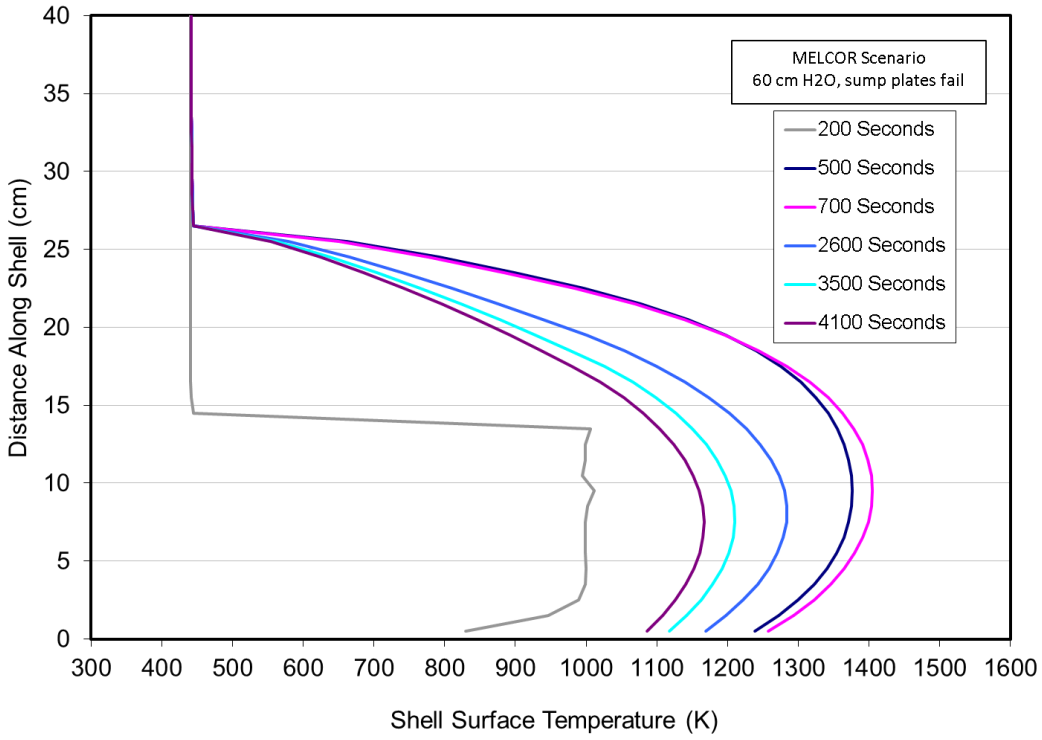

Fig. 17. Drywell Liner Surface Temperature Profiles for the Best Estimate MELCOR Case.

The results of the two cases performed to examine the effect of increased pour rate on spreading of low temperature debris (cases MELCOR-5 and -6) indicate that spreading area increases substantially relative to that seen for the low pour rate cases (Figure 14). For this case, inertial effects become important, causing the melt to splash up on the liner outside the pedestal doorway (Figure 16). This causes earlier peaks in the liner surface temperature, but the liner is predicted to remain below the melting point for both cases investigated. The high pour rate case without sump plate failure is the only MELCOR scenario in which the melt is predicted to fully cover the pedestal and drywell annulus floor areas.

As noted earlier, concrete ablation in the MELCOR cases was essentially negligible. Thus, the melt composition at the end of the spreading phase used as input to CORQUENCH for the long-term debris coolability studies was assumed to equal the initial composition (see Table 3). Additional details are provided in the next section.

3.3 MAAP LOW-PRESSURE SPREADING RESULTS

As a reminder, in this scenario the vessel fails at low pressure leading to rapid discharge of a predominately oxidic core melt into the drywell over a period of ~ 18 seconds; see Table 3 and Figure 10. The average pour rate is ~ 8 MT/sec (~1.1 m^3/sec). The pour stream is superheated by ~160 K relative to the oxide liquidus. According to the MELTSPREAD viscosity subroutine, the viscosity of the core debris is ~2 mPa·sec at the vessel exit temperature of 2751 K, which is the same order-of-magnitude as water. Thus, in this scenario the flow is expected to be dominated by inertial effects.

For this case, the MAAP analysis [2] indicates that the water depth on the drywell floor at the time of vessel failure is ~ 20 cm (Table 3). Thus, the best estimate calculation is selected to be the MAAP-LP-4 case (Table 6) in which the sump plates fail at initial contact with the core debris, and the material subsequently spreads under water at a depth that is ~½ the vent line height.

A series of plots showing the melt height and temperature distributions at various times following vessel failure for the MAAP-LP-4 case are provided in Figure 18. Additional plots that describe the melt leading edge location and cumulative floor area coverage as a function of time for all four MAAP-LP cases are provided in Figures 19 and 20, respectively. Due to the high pour rate and low viscosity, the melt rapidly fills the sump volume and then begins to spread out the pedestal doorway, making contact with the liner at ~12 seconds; see Figure 19. The core melt then begins spreading throughout the annulus, eventually covering the entire floor in ~ 30 seconds. By two minutes, sloshing has effectively ceased and the debris equilibrates at a uniform level in the pedestal/drywell at ~13 cm. The corresponding melt depth in the sump at the end of the spreading transient reaches ~ 133 cm. As is evident from Figure 18, a concrete erosion pocket forms inside the pedestal doorway and just outside this opening; the peak erosion depth reaches ~ 20 cm over two minutes. This localized ablation pocket is due to relatively high spreading velocities that are achieved (approaching 3 m/sec) as the material relocates through this narrow opening and into the annulus. The high velocities, in conjunction with the shallow melt depth and low viscosity, result in large convective heat transfer coefficients in this region.

Predicted core debris depth adjacent to the liner outside the pedestal doorway, as well as the peak liner surface temperature, are shown in Figures 21 and 22, respectively, for all four MAAP-LP cases. To provide additional detail regarding the liner heatup behavior, the crust thickness and liner surface temperature profiles for the best-estimate MAAP-LP-4 case are provided in Figures 23 and 24, respectively. (As noted earlier, the liner is inclined at an angle of 45º with respect to vertical, and so the length along the liner covered by melt is equal to the square root of two times the local melt depth). Due to the high flow rate and low viscosity, the code predicts that the melt initially washes up on the liner (Figure 21), leaving a residual crust higher up on the liner early in the transient (Figure 23). The liner surface temperature shows an early peak that is indicative of initial melt contact and crust growth to the quasi-steady equilibrium depth. Thereafter, the liner surface cools as heat is dissipated into the bulk of the steel. However, the heat sink is eventually exhausted and the surface begins to heat up. The liner continues to heat until a quasi-steady condition is reached at which heat transferred from the melt is dissipated by conduction up along the liner where it is dumped to the overlying water by boiling heat transfer. The inflection point in the surface temperature response at 540 seconds corresponds to the point where bulk solidification of the core debris next to the liner is predicted to occur. At this point, the heat transfer switches from convection from a melt pool to conduction-limited heat transfer from solidified debris, and so the liner begins to cool slightly after reaching a peak temperature of ~1720 K, which is below the steel melting point of ~1810 K. Thus, the liner is predicted to remain intact for this scenario since the melting point is not reached. However, as noted earlier, this analysis does not consider other potential failure modes such as creep rupture (see previous footnote).

Examination of Figures 19 and 20 for the other three MAAP-LP cases indicates that the overall spreading behavior is not sensitive to the presence or absence of water. This is due to the fact that the energy transport from the vessel during the melt relocation process for this high-pour rate, high temperature case overshadows achievable (i.e. CHF-limited) heat removal rates to overlying water, and so the melt is readily able to spread to a uniform melt depth. For the case in which the sump cover plates are assumed to be initially intact, the debris is able to propagate earlier into the drywell and annulus, but the plates are calculated to be ablated through by 4.37 seconds. After this time, a thin melt layer continues to spread outside the pedestal doorway, while material inside the pedestal on the floor begins to flow back into the sump as the sump fills with corium draining from the reactor vessel. The residual material in the annulus cools and seems to impede the spreading behavior later in the transient after the sump fills and material again spills out the doorway. The overall effect is found to be a slight reduction in peak liner temperature relative to that in which the sumps fail at initial melt contact.

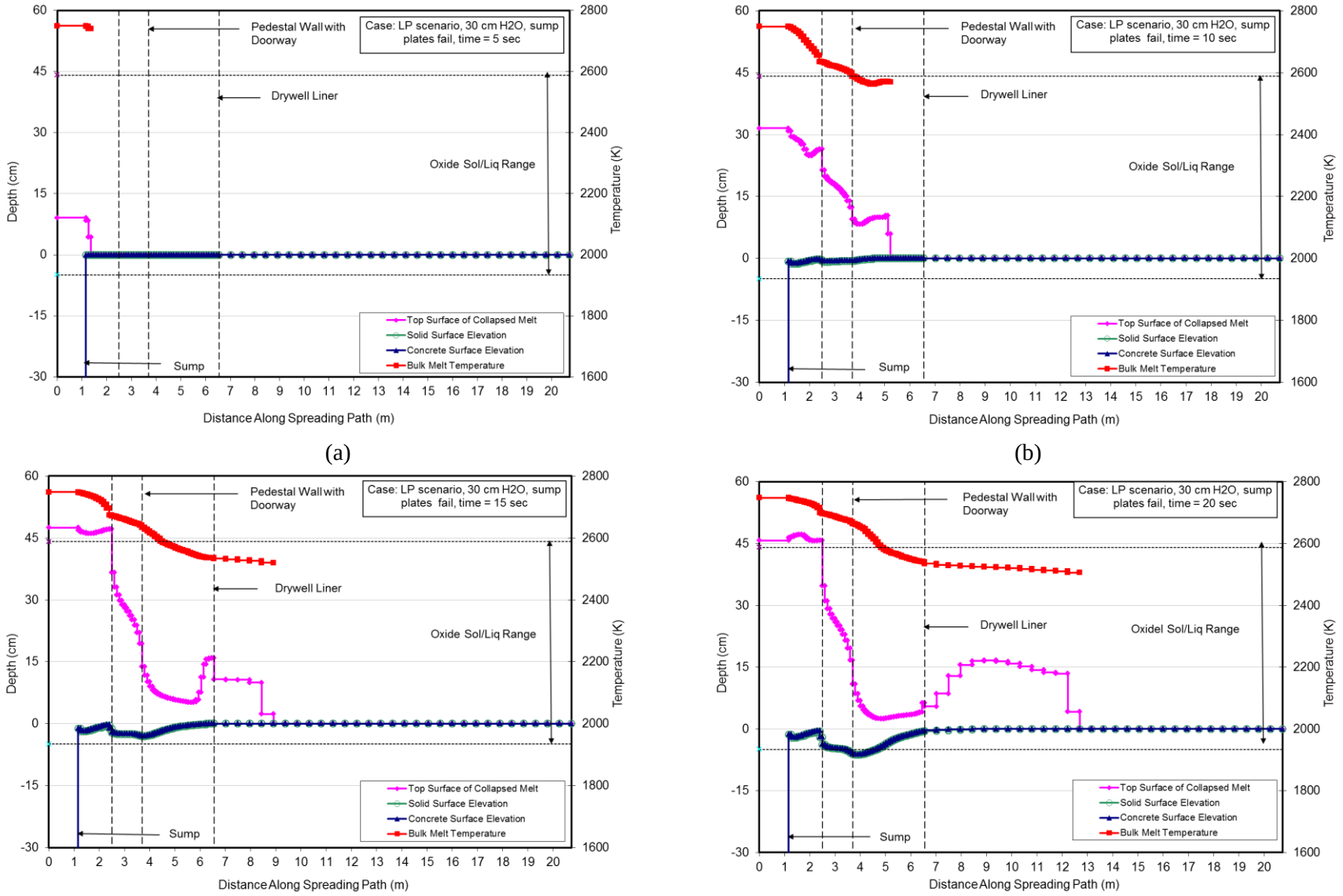

Fig. 18. (a-d) Melt Temperature-Depth Profiles at 5, 10, 15, and 20 sec for MAAP-LP Best Estimate Case.

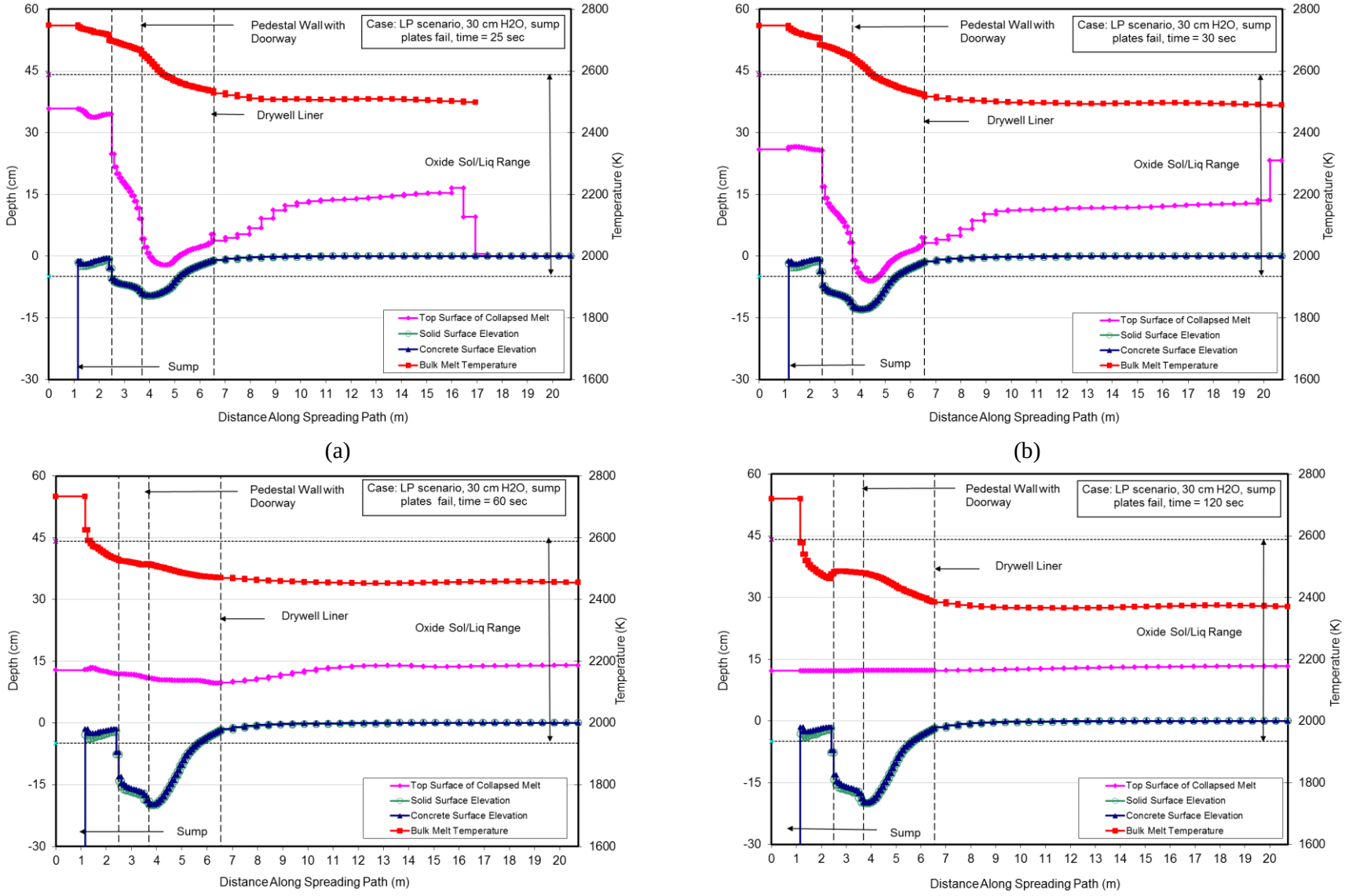

Fig. 18 (contd.). (a-d) Melt Temperature-Depth Profiles at 25, 30, 60, and 120 sec for MAAP-LP Best Estimate Case.

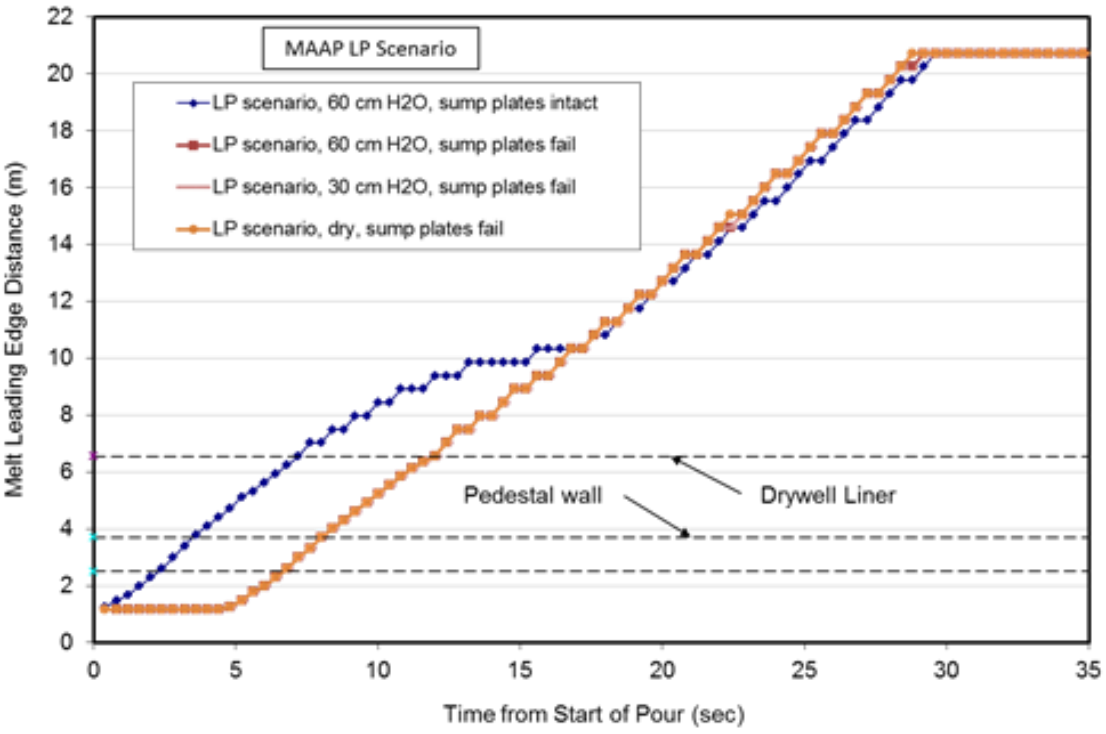

Fig. 19. Melt Leading Edge Penetration Rate for the MAAP-LP Parametric Cases.

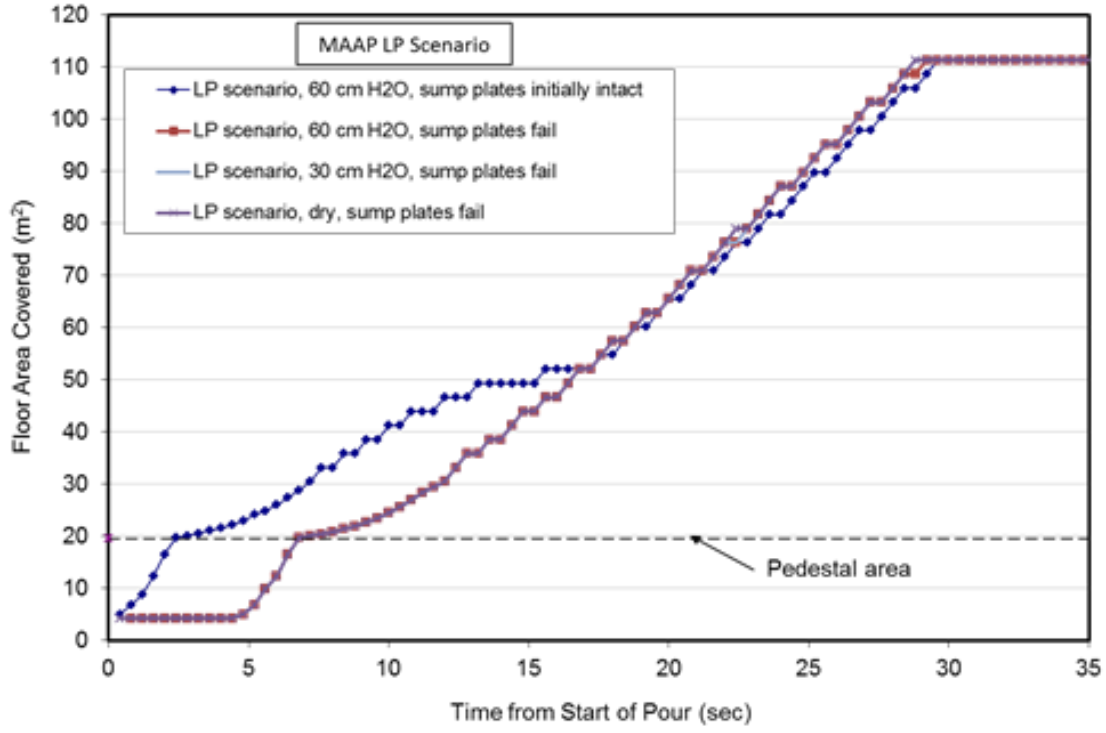

Fig. 20. Basemat Floor Area Covered by Melt for the MAAP-LP Parametric Cases.

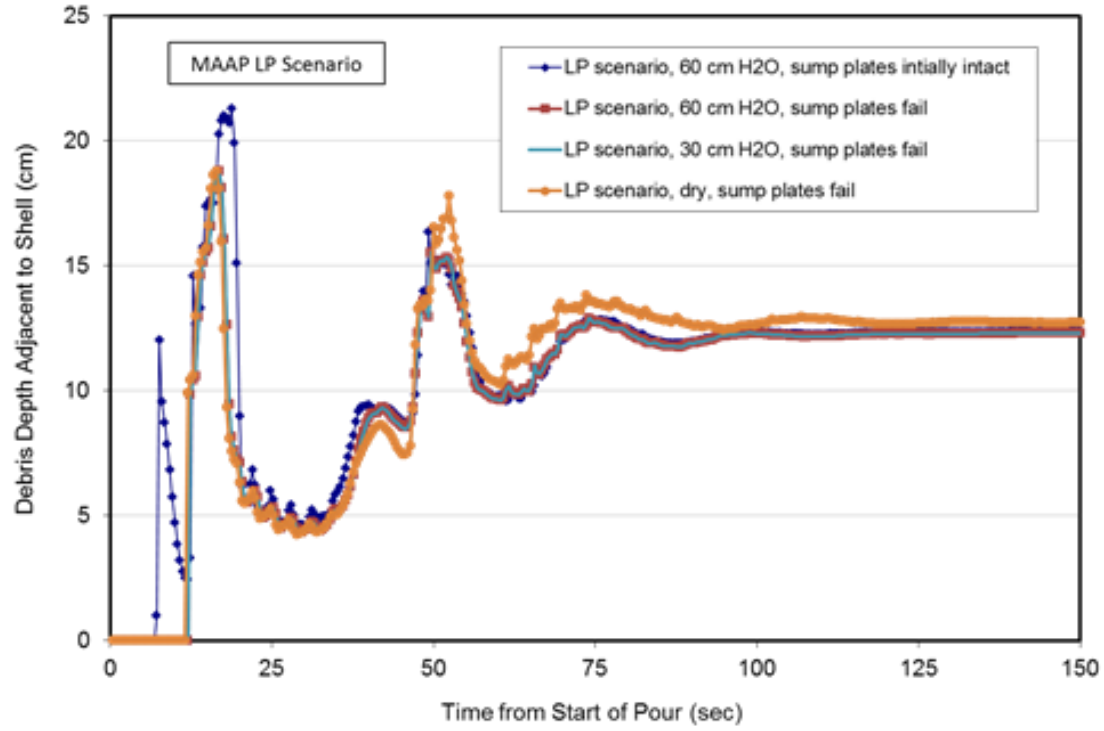

Fig. 21. Debris Depth Adjacent to the Drywell Liner Across from the Pedestal Doorway for the MAAP-LP Parametric Cases.

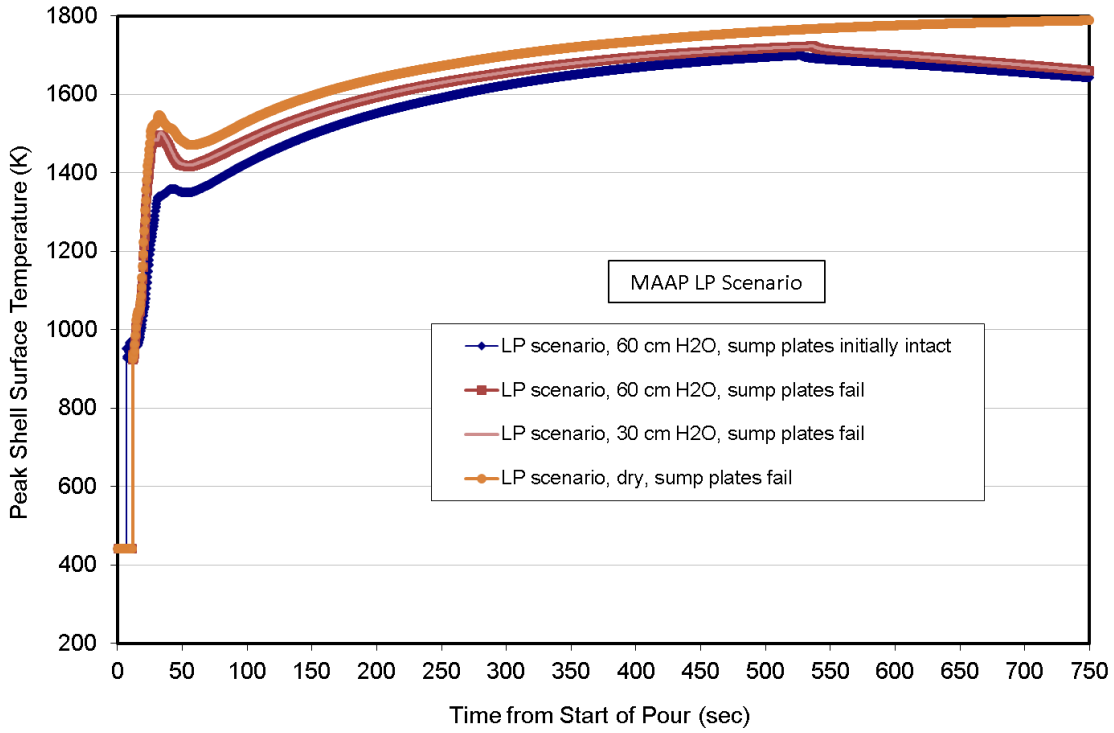

Fig. 22. Peak Liner Surface Temperatures for the MAAP-LP Parametric Cases.

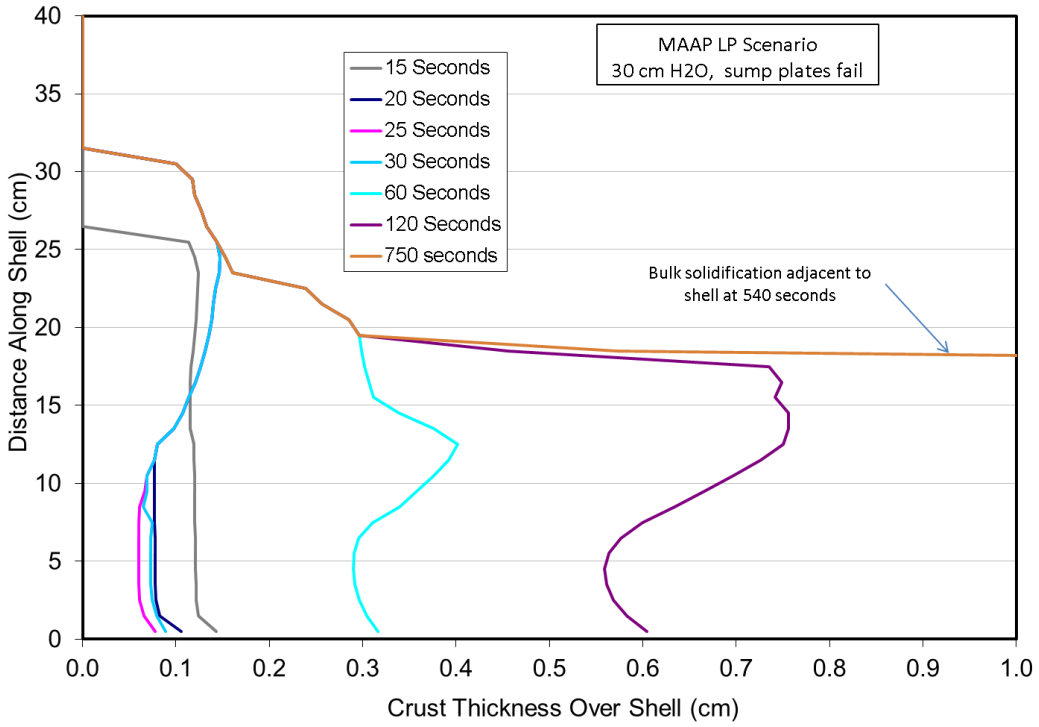

Fig. 23. Drywell Liner Crust Profiles for the Best Estimate MAAP-LP Case.

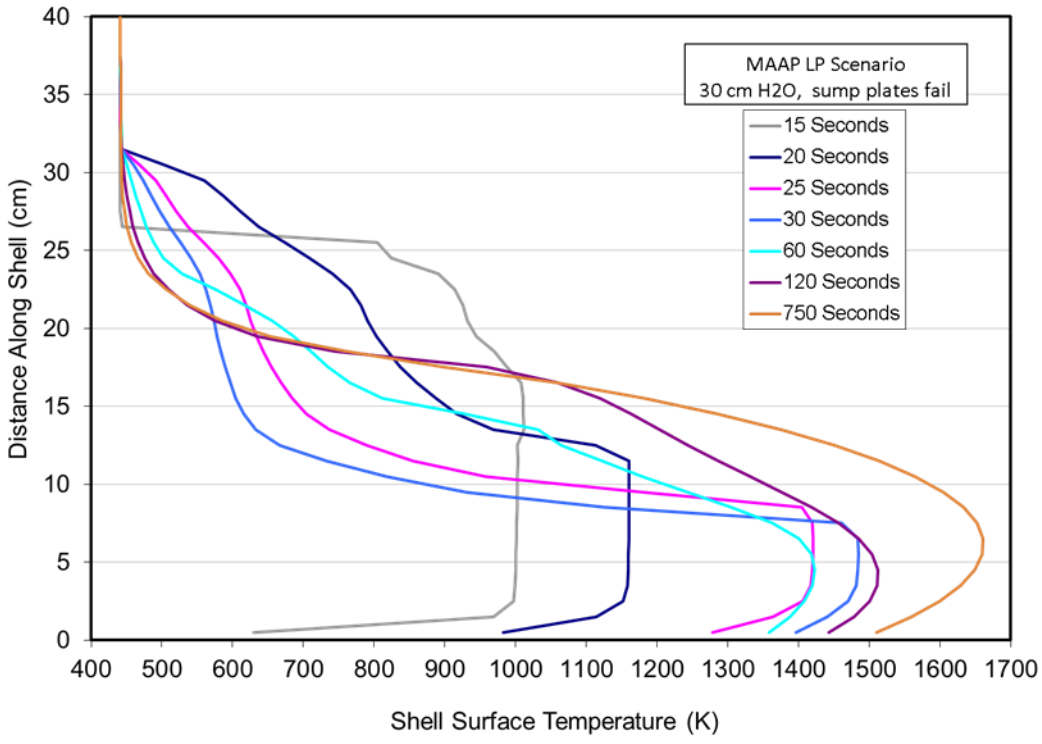

Fig. 24. Drywell Liner Surface Temperature Profiles for the Best Estimate MAAP-LP Case.

Aside from spreading behavior, the lack of water in the drywell is found to have an effect on liner heat up. For the dry case, the peak liner temperature had reached 1790 K at the end of the computed time interval (750 seconds), and is still rising. Thus, the current analysis predicts that liner failure would be likely for a dry low-pressure MAAP pour scenario.

For the MAAP-LP scenarios, the total mass of slag eroded into the melt over 120 seconds ranged from 3529 to 3553 kg (highest is dry case). Moreover, the amount of cladding oxidized ranged from 409 to 445 kg. These ranges are rather narrow, and as noted earlier this is due to the fact that the high enthalpy flux from the RPV during spreading effectively overshadows parameters that can affect the extent of spreading, such as presence/absence of water, or whether or not the sump plates ablate through. On this basis, an average melt composition for the LP scenario after spreading was defined (see Table 9) to simplify the long term debris coolability analyses with CORQUENCH that are described in the next section. Melt temperatures at various locations were extracted from the MELTSPREAD spatial distribution datasets for input into the CORQUENCH calculations.

Table 9. Average Post-Spreading Melt Compositions for All Scenarios

Constituent	MELCOR	MAAP-LP		MAAP-HP	
	Pour and Post-Spreading Melt Mass (kg)	Pour Mass (kg)	Post Spreading Melt Mass (kg)	Pour Mass (kg)	Post-Spreading Melt Mass (kg)
UO_2	69400	76153.2	76153.3	76153.4	76153.4
Zr	25800	16594.1	16166.0	16616.0	16165.0
ZrO_2	16600	14141.5	14713.0	14112.7	14714.0
Cr	5900	1135.9	1135.9	1099.4	1099.4
Cr_2O_3	30	2732.0	2732.0	2765.5	2765.5
Fe	20430	16095.1	16095.1	15928.4	15928.4
FeO	230	11210.5	11210.5	11369.5	11369.5
Ni	2530	555.7	555.7	534.8	534.8
NiO	30	1208.2	1208.2	1229.1	1229.1
B_4C	0	502.0	502.0	502.0	502.0
SiO_2	0	0.0	2523.0	0.0	2919.5
CaO	0	0.0	405.9	0.0	469.7
MgO	0	0.0	283.3	0.0	327.8
Al_2O_3	0	0.0	382.9	0.0	443.0
Total	140950	140328.3	144066.8	140310.8	144621.1

3.4 MAAP HIGH PRESSURE SPREADING RESULTS

As a review, in this scenario the vessel fails at elevated pressure leading to very rapid discharge of a predominately oxidic core melt into the drywell over a period of ~ 5 seconds; see Table 3 and Figure 11. The average pour rate is ~ 26.5 MT/sec (~3.6 m^3/sec). The pour stream is superheated by ~210 K relative to the oxide liquidus. According to the MELTSPREAD viscosity subroutine, the viscosity of the core debris is ~1.8 mPa·sec at the vessel exit temperature of 2797 K, which is the same order-of-magnitude as water.[1] Thus, as for the low-pressure scenario, the flow for this case is expected to be dominated by inertial effects.

The MAAP analysis [2] for this scenario indicates that the cavity was effectively dry at the time of vessel failure (Table 3). Thus, the best estimate calculation is selected to be the MAAP-HP-3 case (Table 7) in which the sump plates fail at initial contact with the core debris, and the material subsequently spreads into a dry cavity.

A series of plots showing the melt height and temperature distributions at various times following vessel failure for the MAAP-HP-3 case are provided in Figure 25. Additional plots that describe the melt leading edge location and cumulative floor area coverage as a function of time for all four MAAP-HP cases are provided in Figures 26 and 27, respectively. As for the low-pressure MAAP sequence, due to the high pour rate and low viscosity, the melt rapidly fills the sump volume and then begins to spread out the pedestal doorway, making contact with the liner at ~6 seconds; see Figure 26. The core melt then begins spreading throughout the annulus, eventually covering the entire floor area in ~ 21 seconds. By two minutes, sloshing has effectively ceased and the debris equilibrates at a uniform level in the pedestal/drywell at ~13 cm. The melt depth in the sump at the end of the spreading transient thus reaches ~ 133 cm. A concrete erosion pocket forms for this case also inside the pedestal doorway and just outside the opening; the peak erosion depth reaches ~ 20 cm by 120 seconds. As noted earlier, this localized ablation pocket is caused by high spreading velocities that are achieved as the material relocates through this narrow opening. These velocities, coupled with the shallow melt depth outside the doorway, produce large convective heat transfer coefficients in this region.

The predicted core debris depth adjacent to the liner outside the pedestal doorway and the peak liner surface temperature are shown in Figures 28 and 29, respectively, for all four MAAP-HP cases. For this case, the liner surface temperature rapidly rises to the steel melting point (taken as 1810 K in these analyses) and erosion of the liner commences (the plateaus seen in the surface temperatures at the melting point correspond to the time intervals for the latent heat of fusion to be removed from the surface mesh cells in the numerical solution scheme). For this scenario, the code predicts sustained ablation of the liner, and subsequent failure by melt-through at 165 seconds. The contrast between this prediction and that for the low-pressure scenario is principally due to the higher melt temperature (~ 50 K) coupled with the higher melt pour rate that results in significantly higher thermal loading on the liner.

Examination of Figures 26 and 27 for the other three MAAP-HP cases indicates that the overall spreading behavior is not sensitive to the presence/absence of water. As for the low-pressure scenario, this is due to the fact that the energy transport from the vessel during the melt relocation process for this pour overshadows practically achievable heat removal rates to overlying water, and so the melt is readily able to spread to a uniform melt depth. For the case in which the sump cover plates are assumed to be initially intact, the debris is able to propagate earlier into the drywell and annulus, but the plates are calculated to be ablated through by 3.58 seconds. By this time though, sufficient corium has accumulated in the pedestal to completely fill the sump, and so the fluid mechanics of the spreading process are not significantly perturbed after the material on top the plates is relocated (dropped by the code) down into the sump.

Aside from spreading behavior, the lack of water in the drywell is also found to not have a significant influence on the liner heat up and ablation rates. In particular, failure times for all cases were in the range of 162-168 seconds. Similar to the spreading behavior, this is due to the high impingement heat transfer on the liner in this sequence that dominates heat removal rates by fin cooling to overlying water.

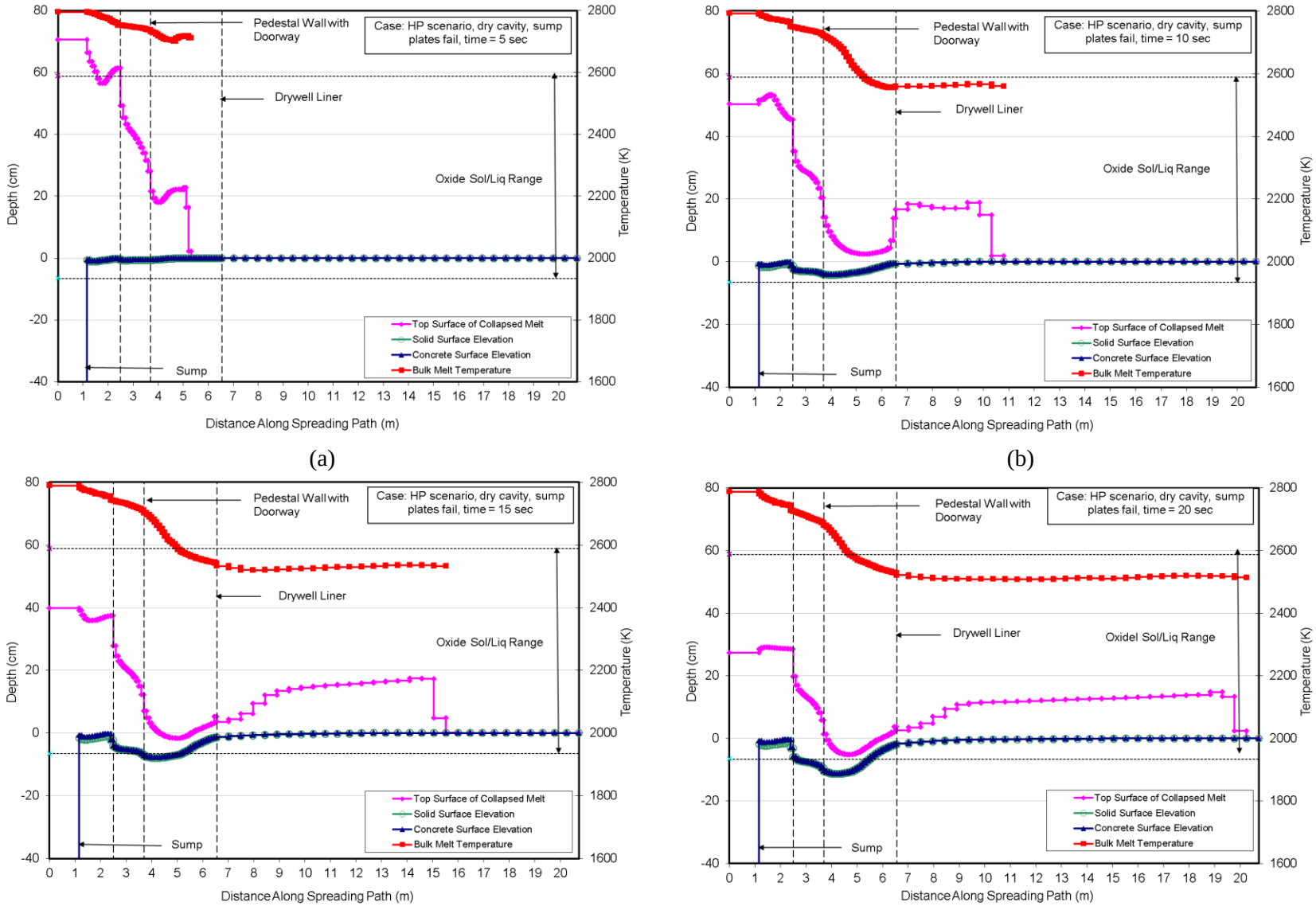

Fig. 25. (a-d) Melt Temperature-Depth Profiles at 5, 10, 15, and 20 sec for MAAP-HP Best Estimate Case.

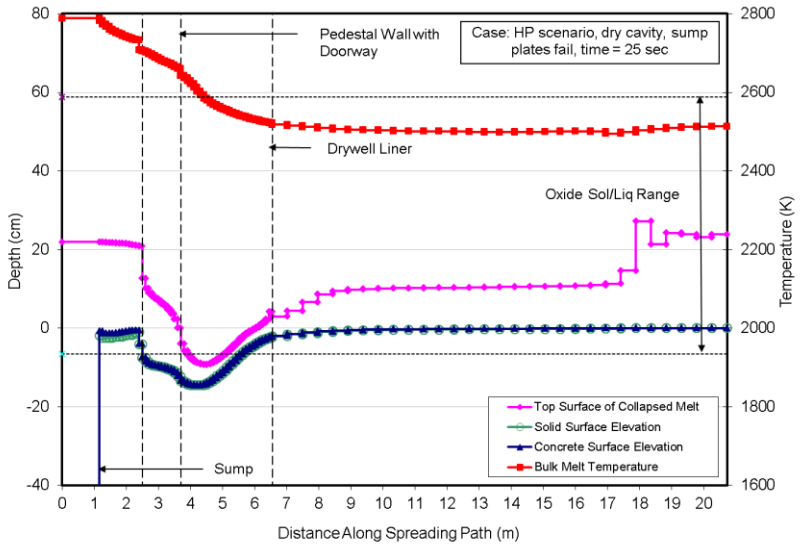

(a)

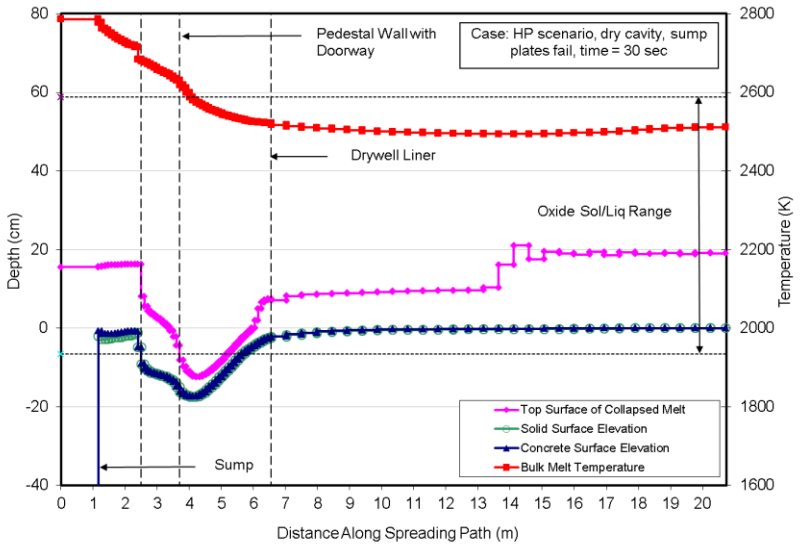

(b)

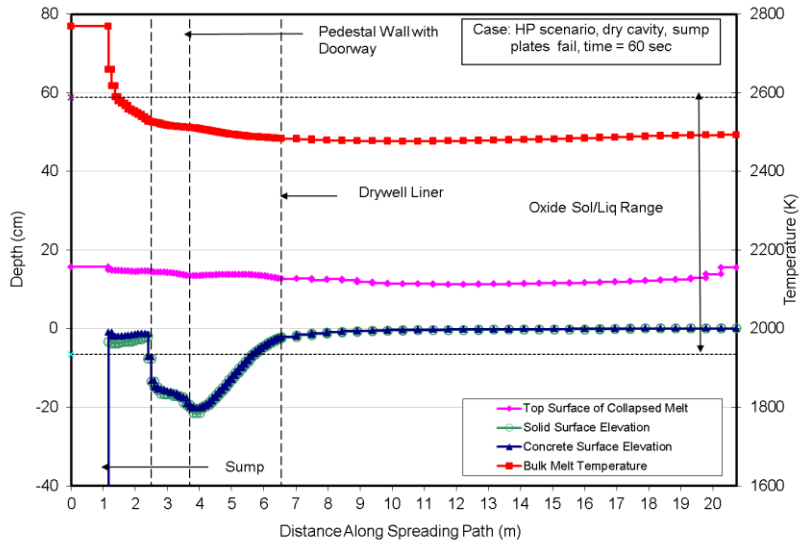

(c)

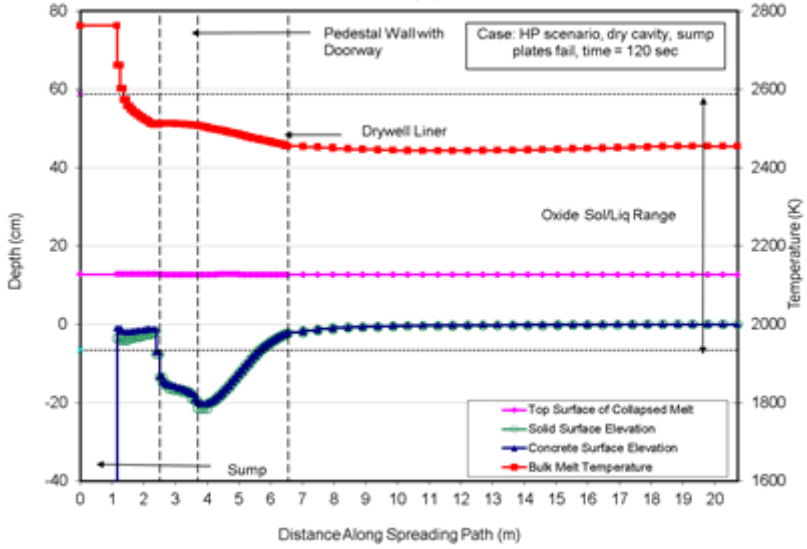

(d)

Fig. 25 (contd.) (a-d) Melt Temperature-Depth Profiles at 25, 30, 60, and 120 sec for MAAP-HP Best Estimate Case.

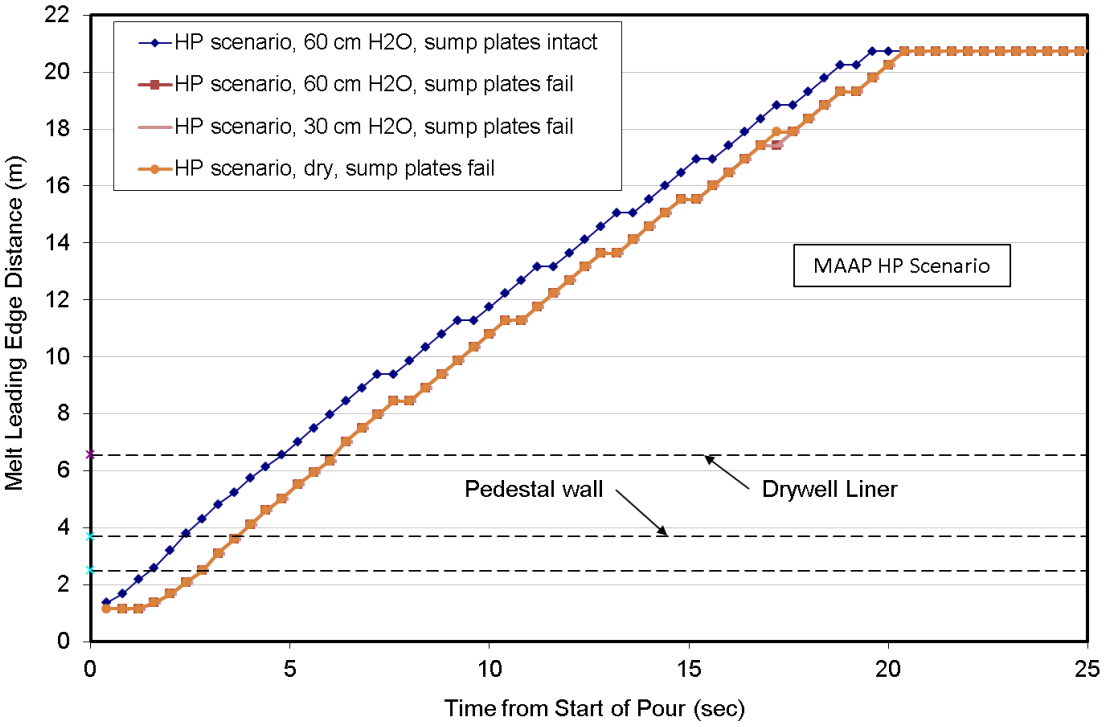

Fig. 26. Melt Leading Edge Penetration Rate for the MAAP-HP Parametric Cases.

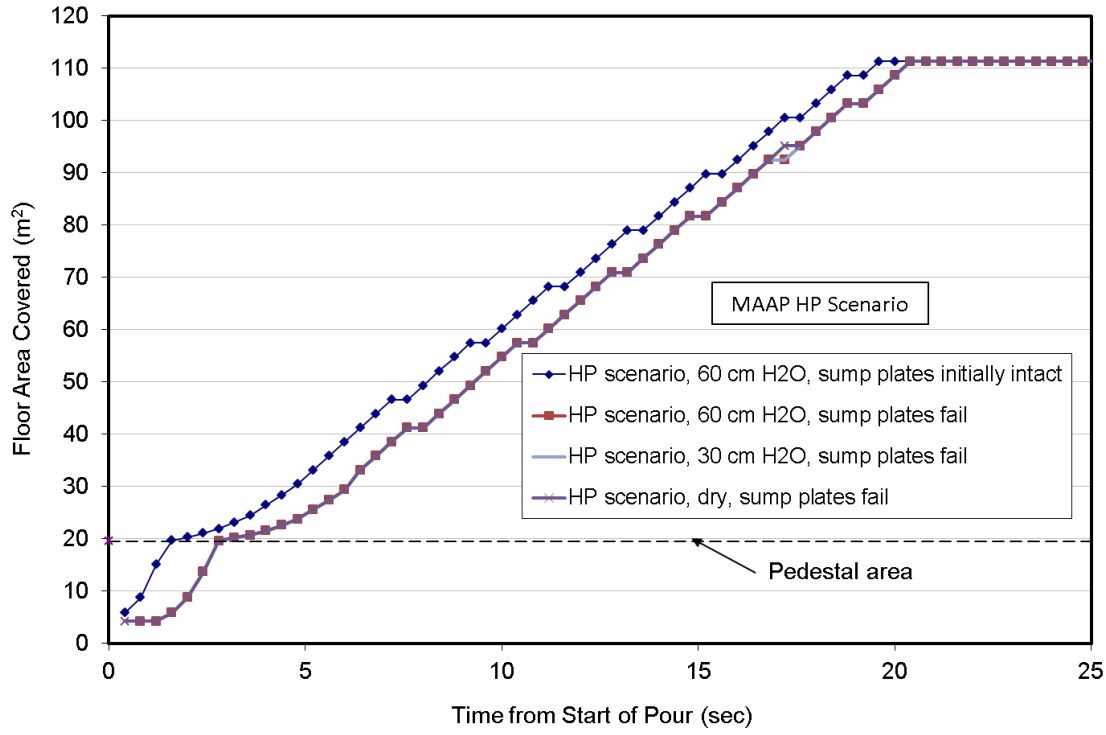

Fig. 27. Basemat Floor Area Covered by Melt for the MAAP-HP Parametric Cases.

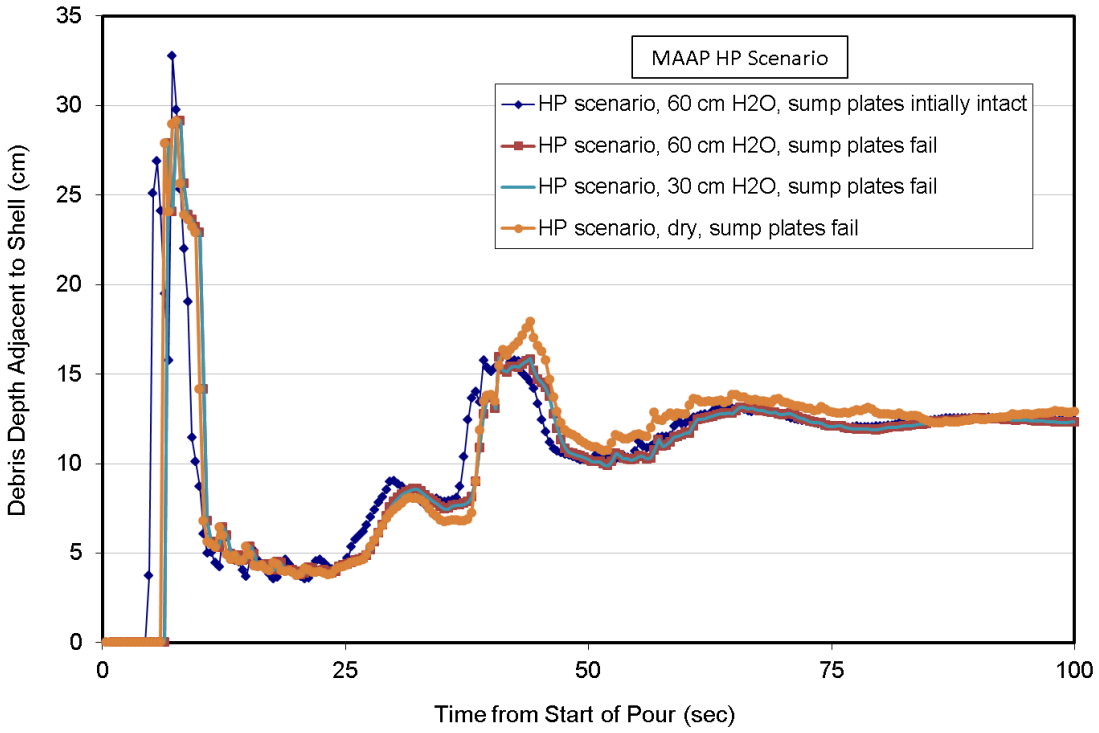

Fig. 28. Debris Depth Adjacent to the Drywell Liner Across from the Pedestal Doorway for the MAAP-HP Parametric Cases.

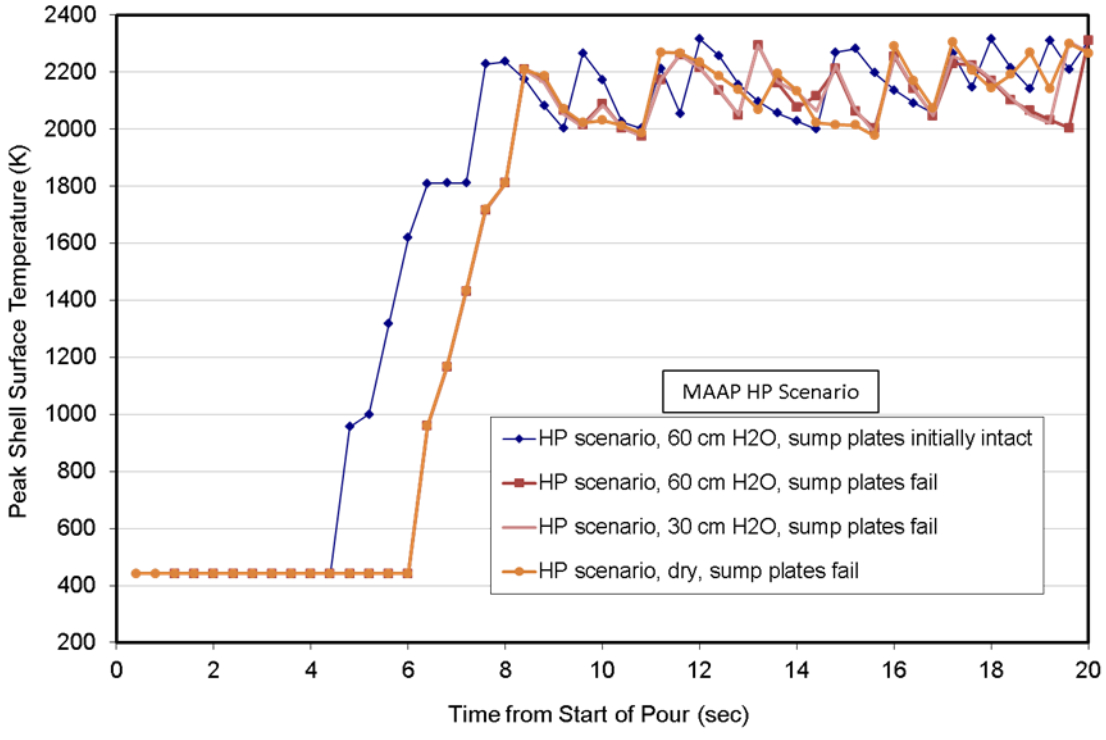

Fig. 29. Peak Liner Surface Temperatures for the MAAP-LP Parametric Cases.

For the MAAP-HP scenarios, the total mass of slag eroded into the melt over 120 seconds ranged from 4076 to 4323 kg (highest is dry case). These masses are noted to be modestly higher than those calculated for the MAAP-LP cases. The amount of cladding oxidized is also slightly higher, ranging from 443 to 459 kg. These ranges are rather narrow, and as noted earlier this is due to the fact that the high enthalpy flux from the RPV during spreading grossly overshadowed parameters that can affect the extent of spreading, such as presence/absence of water, or whether or not the sump plates fail. On this basis, an average melt composition for the HP scenario after spreading was defined (see Table 9) to simplify the long term debris coolability analyses with CORQUENCH that are described in the next section. Melt temperatures at various locations were also extracted from the MELTSPREAD spatial distribution datasets for input into the CORQUENCH studies.

This page intentionally left blank.

4. CORQUENCH ANALYSES OF CORE DEBRIS COOLABILITY

4.1 SUMMARY OF CASE SCENARIOS AND MODELING ASSUMPTIONS

4.1.1 Containment Nodalization

CORQUENCH has three basic geometric modeling options that are summarized in Table 10. To capture the spatial variation in melt depth and concrete ablation, the containment was divided into six regions: the sumps (1), inner pedestal (2), inside edge of the pedestal (3), doorway (4) between the drywell and pedestal, an area extending from the doorway to the drywell liner (5) and the far field drywell (6). These regions are numbered and illustrated in Figure 30.

The division of containment into computational regions for CORQUENCH simulations has not previously been performed, and the methodology was developed as part of this work. To accomplish this with the code, each region is modeled independently; i.e., there is no heat or mass transfer between regions as time progresses. The methods used to model each region are summarized below.

The sumps (1) are modeled as 2-D cylindrical cavities with walls that are higher than the melt. In reality, the sumps are square and the accumulated melt depth above the height of the sumps will not be in direct contact with the sump walls. The initial collapsed melt depth in the sumps for the MELCOR cases ranged from 0.2-1.9 m while all the MAAP cases were 1.4 m deep. The sumps are 1.2 m deep, and so the majority of the melt was in contact with the sump walls for all cases. The floor areas of the sumps (2.1025 m^2 each) are conserved such that the melt height is conserved. Only one sump is simulated and the results are assumed to be the same for the other sump.

The inner pedestal region (2) includes 10.851 m^2 of area between and around the sumps. This region is modeled using the 1-D geometry option.

The pedestal edge (3) region is modeled using a 2-D cylindrical geometry similar to the sumps. The diameter of the cavity is the same as the actual pedestal, 5.0 m. The amount of melt per unit area in the edge region, as determined from the MELTSPREAD results, is extrapolated to fill the inner portion of the 2-D cylinder. This conserves the melt height at the pedestal walls and the pedestal curvature. These parameters were conserved in order to conserve the heat and mass transfer at the walls. However, the approach also requires scaling of other important parameters such as combustible gas generation during core-concrete interaction; the methodology for accomplishing this is described later in this section.

Table 10. CORQUENCH geometry modeling options

Geometry Option	Ablatable Surfaces	Adiabatic Surfaces
1-D Floor area	Bottom	All sidewalls
2-D Cylinder	Bottom and sidewalls	None
2-D Rectangular notch	Bottom and two sidewalls	Other two sidewalls

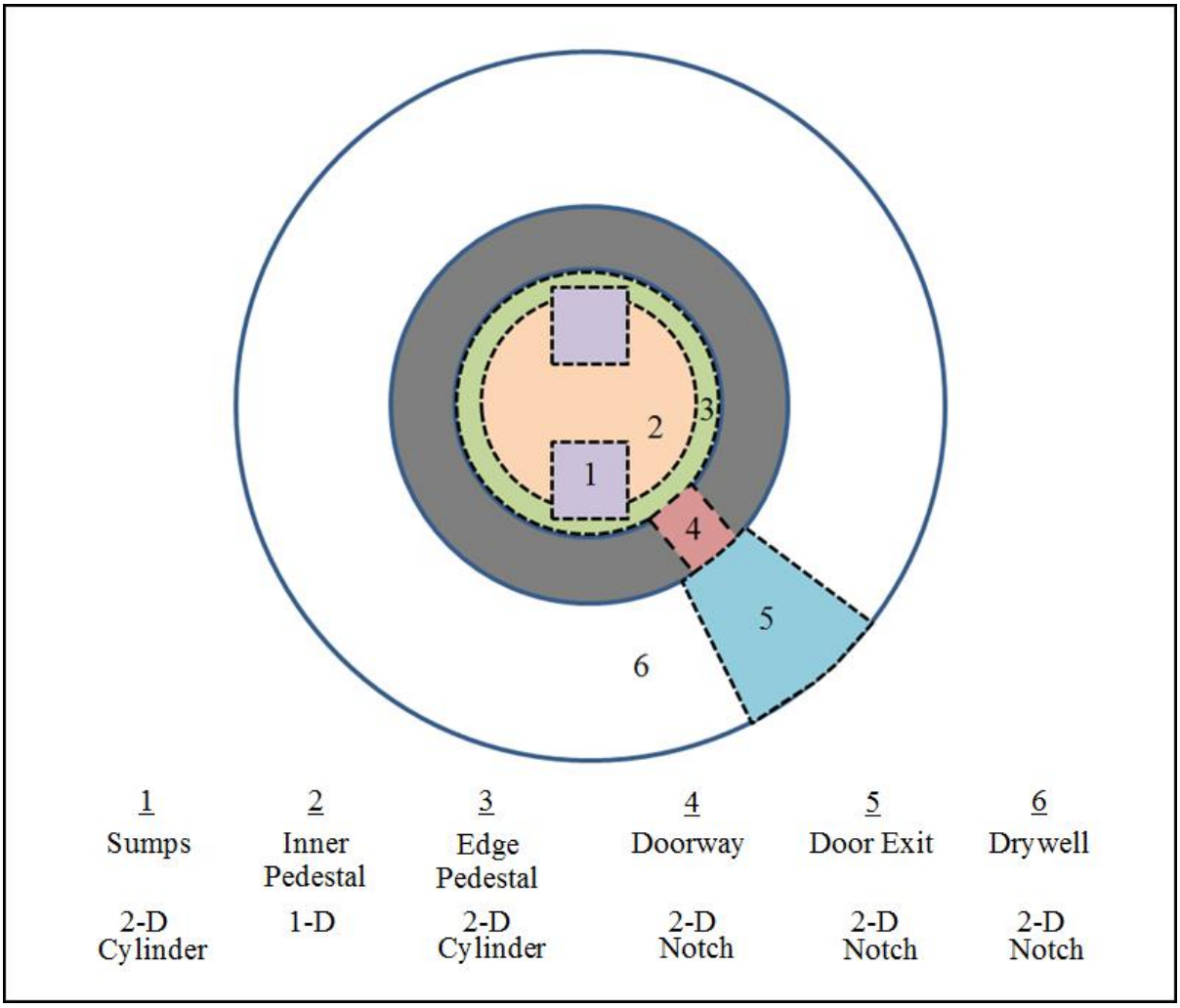

Fig. 30. Containment Discretization.

The doorway region (4), the area outside the doorway (5), and the far-field drywell (6) are modeled as 2-D notch geometries. The doorway region (4) is modeled as a rectangular area (1.2 m^2) with two 1.2 m long concrete walls and two 1.0 m long adiabatic walls. The 90º spreading sector outside the pedestal door exit region (5) is modeled as a rectangular area (9.69 m^2) with two 3.4 m long concrete walls and two 2.85 m long adiabatic walls. The drywell (6) region includes all of the drywell floor area except for the doorway exit region which is covered in melt. The drywell is modeled as a rectangular area with two adiabatic walls that are 2.85 m in length (width between pedestal and drywell liner). The floor area and concrete wall lengths are specified for each case in order to conserve the spread area predicted by MELTSPREAD.

While the method used to discretize the containment for CORQUENCH simulations enables spatial variations of ablation to be evaluated, there are a few compromises and limitations associated with the technique.

The heat transfer between regions is not captured. However, the cross-sectional area of melt in neighboring regions is much lower than that in contact with concrete and water (or the containment atmosphere). In addition, after spreading, lateral heat transfer between neighboring regions would be much lower than the heat transfer to the water (or atmosphere) and concrete.

Mass transfer between regions is also not modeled. The swelling of the melt by the gases released during concrete ablation may cause regions of the melt to rise and spread to other regions. This effect is expected to be small over the majority of the spreading area. However, the effect may be more pronounced in the sumps where there is a larger column of melt and the concrete ablation is generally higher. When combined, these two effects result in greater changes in melt elevation due to voiding. All melt that is initially in the sump is assumed to stay there. This results in a less coolable melt configuration.

Radial ablation may cause regions to expand into one another (recall again that no interaction between regions is modeled). For instance, if the predicted radial ablation in the sumps is greater than 0.75 m (the sumps are 1.5 m apart), then the modeling approach will result in subsequent distortions to the predicted cavity ablation behavior. Clearly this effect will increase with the extent of radial ablation, but for most regions this influence is expected to be negligible.

In the 2-D notch geometry modeling option, CORQUENCH does not currently possess the ability to independently specify each wall material. Therefore, the liner wall is modeled as concrete. Concrete ablation starts at 1500 K which is lower than the melting point of the liner (~1810 K). In addition, CORQUENCH does not contain a detailed liner heat transfer model like that implemented in MELTSPREAD. Therefore, the ablation predictions by CORQUENCH, near the liner, are conservative. A more rigorous investigation of the melt-liner interface with the MELTSPREAD code was presented in Section 3.

4.1.2 Mapping MELTSPREAD Results into CORQUENCH

The MELTSPREAD simulations provide detailed melt locations, compositions, and temperature as well as the concrete ablation depths as functions of time and position. The output at the end of the MELTSPREAD simulations were used as input for the CORQUENCH simulations.

For the MELCOR cases, MELTSPREAD predicted essentially no concrete ablation or additional cladding oxidation during the spreading phase. Thus, the melt compositions at the end of the MELCOR spreading phase were assumed to be identical to the pour composition; see Table 9.

For the MAAP cases, MELTSPREAD predicted a modest amount of concrete ablation during the spreading phase (~2 m^3 in volume principally located in the pedestal doorway and just outside the door). The MAAP-LP and -HP scenarios yielded similar amounts of ablation (i.e., average slag content in the melt was 2.5 and 2.8 wt %. for the LP and HP scenarios, respectively). The average melt compositions at the end of the spreading phase for these two cases are provided in Table 9.

The three sets of melt compositions shown in Table 9 were used for all CORQUENCH simulations of the MELCOR, MAAP-HP, MAAP-LP scenarios. The relative fraction of oxide to metallic components in each of the six CORQUENCH computation regions (taken from the MELTSPREAD output), were conserved in the CORQUENCH simulations. The melt mass and composition in each of the six CORQUENCH regions for each case were determined in the following way. The melt constituents (in Table 9) were binned into two groups, a metallic and an oxidic group. The mass of the oxide and metal in each region was then determined from the MELTSPREAD output based on the total mass (in each region) in conjunction with the weight fractions for the oxide and metal phases for each case. These fractions were then used to determine the oxide and metal component masses in each region, based on the melt compositions in Table 9. As previously noted, in the 2-D cylindrical pedestal edge region (see Figure 30) the melt mass was extrapolated to fill the inner portion of the 2-D cylinder.

Table 11 summarizes the initial, area averaged, collapsed melt thicknesses in each of the discretized cavity regions for the MELCOR and MAAP cases described in Table 9. All the MAAP cases are noted to be similar, while each MELCOR case is unique. For the MAAP cases, the melt thicknesses in the doorway and door exit regions are greater than neighboring regions. This is due to concrete ablation occurring in the doorway and door exit regions during the spreading process.

Table 11. Initial Collapsed Melt Thickness

Case	Initial Collapsed Melt Thickness (cm) in each Region					
	1 Sumps	2 Inner Pedestal	3 Edge Pedestal	4 Doorway	5 Door Exit	6 Drywell
MELCOR-1	187	63	46	29	21	4
MELCOR-2	69	60	47	26	22	18
MELCOR-3	166	44	39	16	13	12
MELCOR-4	177	58	60	53	21	4
MELCOR-5	139	17	16	16	16	15
MELCOR-6	18	18	18	17	18	17
MAAP-HP-1	140	16	16	29	21	13
MAAP-HP-2	139	17	16	28	21	13
MAAP-HP-3	140	16	17	29	22	13
MAAP-HP-4	140	16	16	29	21	13
MAAP-LP-1	139	15	16	29	20	13
MAAP-LP-2	140	17	16	28	19	13
MAAP-LP-3	139	16	17	30	21	13
MAAP-LP-4	139	15	16	29	20	13

For the MELCOR cases, a large fraction of the melt was predicted to be solidified by the end of the MELTSPREAD simulation (see Table 12). CORQUENCH currently does not have the ability to model re-melting of solid debris when the debris is completely solid at the start of the simulation. Thus, in order to investigate the long term coolability of the melt for this scenario, the initial melt temperature in CORQUENCH was artificially increased to a few degrees above the average core debris solidus temperature for the oxide-metal mixture predicted by the CORQUENCH property subroutines [12]. In particular, the initial temperature of the debris was assumed to be 2110 K, which can be compared with the solidus temperature of 2108 K predicted for the MELCOR composition shown in Table 9. CORQUENCH was then utilized to determine the long term coolability of the melt with its advanced coolability and concrete ablation models. Thus, with this assumption CORQUENCH evaluates the cooling behavior of a highly viscous melt interacting with concrete with an initial solid content of ~78%.

For the MAAP-HP and MAAP-LP cases, the temperature of the melt at the end of the spreading phase was still relatively high. The initial temperature in each of the CORQUENCH computational regions was specified based on the local temperatures predicted by MELTSPREAD at the end of the spreading phase (taken to be 120 seconds). These temperature distributions are summarized in Table 13.

Table 12. Percentage of Melt Mass Frozen at End of MELTSPREAD Simulation

Cases	Percent Frozen
MELCOR-1	45%
MELCOR-2	85%
MELCOR-3	36%
MELCOR-4	41%
MELCOR-5	70%
MELCOR-6	100%
MAAP-HP-(all)	0%
MAAP-LP-(all)	0%

Table 13. Initial Melt Temperature for CORQUENCH Simulations

Cases	Region Initial Temperature [K]					
	1 Sumps	2 Inner Pedestal	3 Edge Pedestal	4 Doorway	5 Door Exit	6 Drywell
MELCOR-(all)	2110	2110	2110	2110	2110	2110
MAAP-HP-1	2759	2759	2476	2487	2443	2358
MAAP-HP-2	2743	2743	2474	2482	2439	2357
MAAP-HP-3	2763	2763	2523	2512	2485	2443
MAAP-HP-4	2759	2759	2477	2487	2443	2358
MAAP-LP-1	2759	2759	2476	2487	2443	2358
MAAP-LP-2	2709	2709	2474	2476	2430	2368
MAAP-LP-3	2725	2725	2520	2508	2482	2445
MAAP-LP-4	2720	2720	2474	2485	2438	2366

4.1.3 Additional Initial and Boundary Condition Assumptions

Additional modeling details based on the Fukushima Daiichi Unit 1 accident progression were also prescribed in order to carry out the CORQUENCH simulations. These details are summarized here. The CORQUENCH cases were started at the end of the MELTSPREAD simulations. The start times for the various scenarios are summarized in Table 14.

Table 14. Summary of Default Initial and Boundary Conditions

Parameter	**MELCOR**	**MAAP-HP**	**MAAP-LP**
Simulation Start Time (h after SCRAM)	15.34 h Cases 1-4 14.48 h Cases 5-6	8.14 h	10.11 h
Initial Melt Temperature	Specified to be 2110 K	From MELTSPREAD results (see Table 13)	
Melt Mass Location	From MELTSPREAD results		
Decay Heat	100% based on values provided by TEPCO (see Figure 31)		
Concrete Type	CORCON-Basaltic (see Table 4 for composition)		
Initial Concrete Temperature	322 K		
Cavity Temperature (thermal radiation sink)	322 K		
Cavity Emissivity	0.6		
Water Addition & Timing	Cavity assumed to be flooded 15 hours after SCRAM		
Containment Pressure	Held constant at 0.75 MPa absolute		
Water Saturation Temp.	440.9 K (saturation temperature at 0.75 MPa)		

Decay heat data as a function of time for Unit 1 was provided by TEPCO. The total decay heat was normalized by an assumed total fuel mass of 78000 kg of UO_2 in Unit 1. The decay heat was then defined in CORQUENCH on a per unit fuel (UO_2) mass basis (W/kg UO_2); see Figure 31. The heat generation in the melt, crust, and particle bed debris regions is then determined in CORQUENCH based on the mass of UO_2 in those regions. The decay heat data was specified in 1-2 hour increments; CORQUENCH linearly interpolates between these data points.

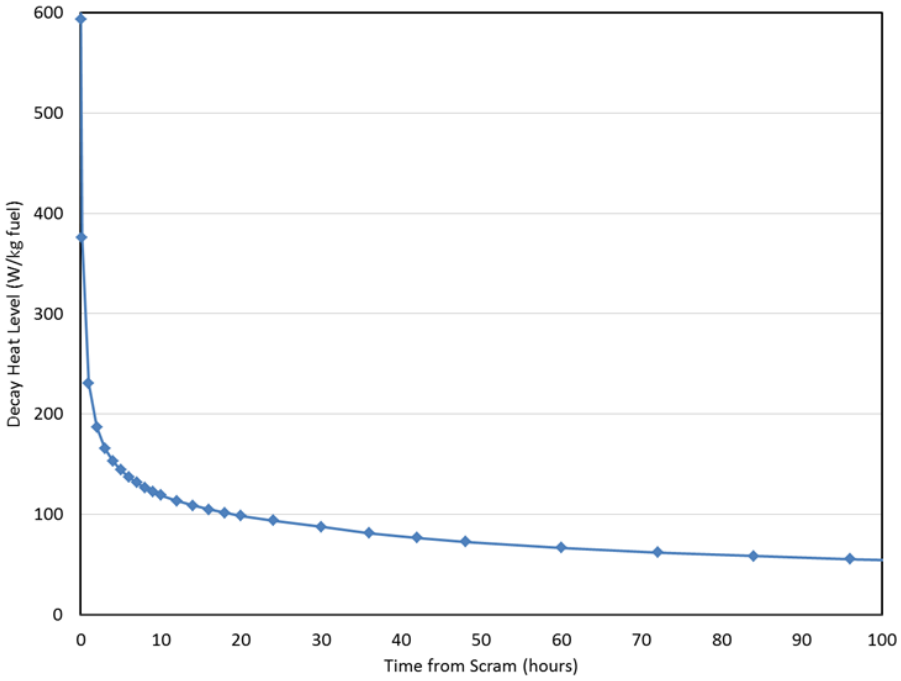

Fig. 31. Debris Decay Heat Curve Used in CORQUENCH Simulations.

CORQUENCH currently does not model the containment free volume. The containment pressure, far field structural temperature (for thermal radiation), and water condition above the melt are prescribed. CORQUENCH can track the mass of water over the debris and the user can specify the water addition rate; however, there is no modeling of condensation on the upper containment walls or the pressurization of containment by non-condensable gases.

In terms of water inlet conditions, TEPCO indicates that water was injected starting 15 hours after SCRAM [73]. TEPCO has also released estimates of the rate and cumulative water injection [74]. Thus, two long term containment conditions were investigated. In the first case, the cavity is assumed to remain dry until 15 hours after SCRAM. At this point the cavity is then assumed to be flooded. As a bounding scenario, a case without water addition was also evaluated as part of the CORQUENCH parametric study. These two long-term containment conditions are felt to bound the melt progression envelope.

Scoping calculations with CORQUENCH have indicated that the reported water injection rates [74] were insufficient to keep the debris completely covered with water (i.e., the water inventory would have been completely evaporated) early in the debris cooling transient. However, as noted above, the code does not calculate steam condensation on overlying structure which would then be available to further cool the melt. Thus, the debris was assumed to be completely covered with water after 15 hours in these simulations for the wet cavity cases.

The containment pressure was assumed to be 0.75 MPa throughout the duration of the simulation. The containment pressure impacts the water saturation temperature, melt sparging rate due to core-concrete interaction, as well as the top crust dryout limit due to water ingression. The dry out of free water in the concrete was assumed to occur at the containment saturation temperature.

In terms of CORQUENCH modeling options, all cases were executed using the concrete transient heat up and decomposition (dry out) model [12, 48]. Any melt-concrete interstitial crusts were assumed to be porous, allowing slag to flow through the crusts into the melt. Based on validation calculations [12], the critical heat flux multipliers for determination of bulk cooling and film boiling breakdown were set at 0.5. The ANL correlation was used to model melt eruptions [58]. For cases in which particle beds formed, the bed porosity and average particle diameter were set to 40% and 2.8 mm, respectively; these

values are based on posttest examination results reported as part of the MACE program [75]. Water ingression was calculated using the Lomperski-Farmer correlation developed as part of the OECD/MCCI program [54]. The empirical constant C in this model was set to 9.0 based on previous code validation work [76]. The crust anchoring modeling option was disabled. The impact of the crust anchoring phenomenon is investigated in the CORQUENCH parametric study (Section 3.3).

The Zr was assumed to be in solution with the core oxide phase, and condensed phase chemical reactions between Zr and SiO_2 were modeled. The top crust thermal conductivity was calculated using the code property subroutines. The effect of solids buildup in the melt was modeled with the Ishii-Zuber correlation with the maximum solids fraction set at 1.0. The effective melt freezing temperature was based on the solidus temperature for the metal and oxide phases. Melt void fraction was modeled using the correlation by Brockmann [45].

All cases were performed with a uniform time step of 0.05 seconds. The low time step was required for some cases to capture the transient growth of the thermal boundary layer in the concrete. A number of cases were performed with smaller time steps to check that the solutions were converged. The cases ended when either 2 days of real time simulation had passed, or the melt was completely solidified

4.1.4 Summary of Case Scenarios

For each of the 14 MELTSPREAD cases summarized in Table 5-Table 7, a CORQUENCH case was executed for each of the six computational regions. In addition, a parameter study was performed by varying several setup and initial conditions, see Table 15. To indicate which set of CORQUENCH modeling options are used, a number is added to the end of the MELTSPREAD case nomenclature. For example, MAAP-HP-1-2, corresponds to the 'MAAP-HP-1' MELTSPREAD scenario from Table 7 and the '-2' refers to the variant CORQUENCH setup indicated in Table 15 (no water addition).

Table 15. Summary of CORQUENCH Simulation Scenarios

ID	Description/Rationale	Parametric Effect Investigated
1	CORQUENCH best estimate models and conditions	None – base case
2	Same as case 1 except there is no water addition	Worse case – no water injection
3	Same as case 1 except the containment pressure is 0.35 MPa instead of 0.75 MPa	Containment pressure
4	Same as case 1 except the melt-concrete crust formation is prohibited and the quasi-steady concrete ablation model is used	Effect of the interstitial crusts and transient conduction on concrete ablation
5	Same as case 1 except the melt decay heat is 25% lower	Reduction of decay heat due to the volatilization and removal of radionuclides
6	Same as case 1 except crust anchoring to the cavity walls is allowed	Impact of possible crust anchoring and separation from the melt pool
7	Same as case 2 except the melt-concrete crust formation is prohibited and the quasi-steady concrete ablation model is used	Effect of the interstitial crusts and transient conduction on concrete ablation

4.2 COOLABILITY RESULTS

In total, 588 CORQUENCH simulations were executed. The post-simulation processing of the data are discussed first, followed by the presentation of the CORQUENCH results for the best estimate cases. The CORQUENCH results for the other MELTSPREAD cases are then described. Finally, the results of the parametric study are summarized. Detailed data for all CORQUENCH simulations are provided in Appendix A.

4.2.1 Post-Processing of Simulation Results

The simulations were terminated when: i) the melt was quenched and stabilized by debris cooling mechanisms, or ii) two days of real time simulation had elapsed. At the end of each case, the total axial and radial ablation, the total simulated time (to quench or two days, whichever came first), and the total amount of concrete decomposition gases released into containment were recorded. The tabulated results for all CORQUENCH simulations are compiled in Appendix A.

The total gas released during concrete decomposition was determined by the summation over all six discretized regions for each case. Since only one of the two sumps were simulated, the amount of gas released by that sump was doubled (symmetry is assumed). Due to the discretization of containment and the limitations of CORQUENCH, the pedestal edge computation region was modeled using a full cylindrical geometry with the same dimensions of the pedestal. However, the concrete ablation and gas released in the inner pedestal region and sump region are simulated and accounted for separately. To prevent double-counting the gases released, the amount of gas released by the pedestal edge region was scaled. The scale factor was determined based on the initial melt-concrete contact area in the full cylinder geometry of the edge region and the contact area already accounted for in the sumps and inner pedestal regions.

The containment ablation profile for each case is reconstructed through superposition of the predicted ablation in each of the six CORQUENCH computational regions. Debris ablation profiles through two cross sections of containment are provided for some cases. The cross sections are illustrated in Figure 32 where cross section A contains the inner pedestal, sump, edge pedestal and drywell regions, while section B contains the inner pedestal, edge pedestal, doorway and door exit regions.

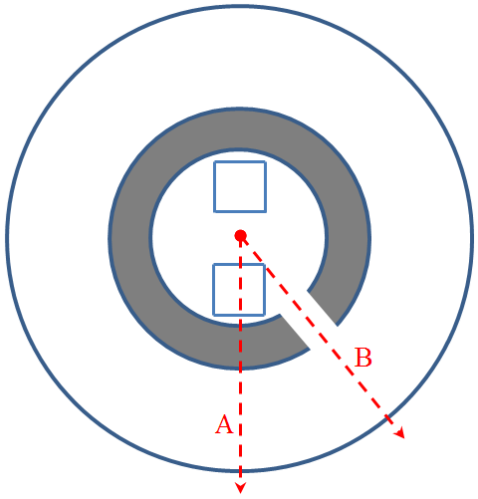

Fig. 32. Cross Sections of Containment Ablation.

For the MELCOR cases, the low temperature, highly viscous, melt pours resulted in negligible concrete ablation during the spreading phase. As no concrete was ablated during spreading, the total ablation is that predicted by CORQUENCH.

For the MAAP cases, the high temperature, low viscosity, melt pours resulted in a modest amount of concrete ablation during the spreading process in the doorway and doorway exit regions, see Figures 18 and 25. The geometric representation in CORQUENCH cannot capture the detailed spatial variation of the cavity. The average amount of concrete slag at the end of the MELTSPREAD simulations for the MAAP-HP and MAAP-LP cases were 4160 kg and 3595 kg, respectively. The assumed concrete composition has a density of 2367 kg/m^3 and contains 7.36 wt% of carbon dioxide and water. Thus, 4160 kg and 3595 kg of slag correspond to 1.9 m^3 and 1.64 m^3 of concrete ablation during the spreading process. If the concrete ablation during spreading are averaged over the combined 1.2 m^2 doorway and 9.69 m^2 doorway exit region floor area, it would represent 17.4 cm of ablation for the MAAP-HP cases and 15.1 cm of ablation for the MAAP-LP cases the in these regions. To account for the ablation during spreading, an additional 17.4 cm (MAAP-HP) and 15.1 cm (MAAP-LP) of concrete ablation should be added to the final ablation predicted by CORQUENCH in the doorway and door exit regions. Note, that the initial depth of each region does not impact the CORQUENCH simulation. The top elevation of the melt in these regions is sufficiently below the height of the drywell-to-wetwell vents such that a water pool, if present in the drywell, would still cover the top of the melt.

4.2.2 Context for Results

Based on previous sensitivity studies [16], the coolability is largely influenced by the melt depth and the presence of water. In addition, as supported by experiments, coolability is largely decreased if crust anchoring to the sidewalls occurs [68]. Other parameters, such as pressure, initial melt temperature, melt composition, etc., have been shown to have a secondary impact on coolability [16].

There is a minimum of approximately 1.4 m of concrete between the bottom outer corner of the sumps and the liner. If the corners of the sumps are filleted, the distance may be greater than 1.4 m. Combined radial and axial concrete ablation in the sumps greater than 1.4 m would suggest the possibility of liner failure in this location.

Radial concrete ablation in the edge pedestal, doorway, door exit and drywell regions can undercut the reactor pedestal. In addition to concrete ablation, CORQUENCH predicts the transient thermal boundary layer thickness in the concrete using a 1-D approximation and the assumption of a parabolic temperature profile [12]. This is of interest as concrete loses compressive strength at elevated temperatures [77]. Based on the parabolic temperature profile assumption, the position, x, relative to the debris-concrete interface, of a temperature isotherm, T(x), can be determined with the following equation, where T_{dc} is the concrete decomposition temperature (specified as 1500 K), T_i is the initial concrete temperature (specified as 322 K) and δ_{bl} is the boundary layer thickness.

$$x = \delta_{bl} \cdot \left(1 - \sqrt{\frac{T(x) - T_i}{T_{dc} - T_i}} \right)$$

Based on this formula, approximately half the boundary layer thickness is above 615 K and a quarter of the boundary layer thickness is greater than 985 K. CORQUENCH does not include any models to predict the structural integrity of the pedestal. However, prediction of significant concrete ablation and a large heat affected zone would suggest additional detailed modeling of the pedestal structural integrity may be warranted.

The total amount of non-condensable gases released by the decomposed concrete is of interest for containment pressurization and failure predictions. The timing and total generation of flammable gases is also of interest in understanding the overall Fukushima Daiichi Unit 1 accident progression. Note, that the

amount of gas released by the concrete is influenced by the concrete composition for which uncertainty exists. In addition, the total amount of flammable gases generated during the ex-vessel concrete ablation phase can be limited by the amount of non-oxidized material that relocates during the melt pour. However, for all plants known to the authors the concrete basemats contain extensive steel reinforcing (rebar), and so a constant source of oxidizable metal will be available as long as core-concrete interaction continues.

4.2.3 Base Case Results

The results from the MELTSPREAD cases, MELCOR-1, MAAP-HP-3, and MAAP-LP-4, were selected as the base case inputs for the CORQUENCH analysis. For each scenario, the RPV was predicted to fail at different times. These cases were selected based on the initial water level predicted to be in the containment at the time of corresponding RPV failure. Table 16-Table 20 summarize the results from the CORQUENCH MELCOR-1-1, MAAP-HP-3-1, and MAAP-LP-4-1 cases.

Table 16. Total CORQUENCH Simulation Time until Melt Solidification

	Simulation Time until Melt Solidification (min) in Region					
Case	1 Sump	2 Inner Pedestal	3 Edge Pedestal	4 Doorway	5 Door Exit	6 Drywell
MELCOR-1-1	151	63	42	24	18	2
MAAP-HP-3-1	1362	476	458	500	483	440
MAAP-LP-4-1	1176	349	333	376	352	319

Table 17. Melt Solidification Timing for Sump Region

	Time Elapsed between Events (hr)			
Case	Pour Initiation and SCRAM	Melt Solidification and SCRAM	Melt Solidification and Pour Initiation	Melt Solidification* and Water Addition
MELCOR-1-1	14.27	17.9	3.6	2.9
MAAP-HP-3-1	8.14	30.9	22.8	15.9
MAAP-LP-4-1	10.11	29.7	19.6	14.7

*Water addition at 15 hours after SCRAM

Table 18. Total Axial Concrete Ablation

	Total Axial Concrete Ablation (cm) in Region					
Case	1 Sump	2 Inner Pedestal	3 Edge Pedestal	4 Doorway	5 Door Exit	6 Drywell
MELCOR-1-1	13.4	8.9	6.9	5.1	4.4	1.3
MAAP-HP-3-1	64.1	23.4	16.2	21.5	22.5	11.4
MAAP-LP-4-1	58.8	21.1	14.4	20.2	19.1	10.1

Table 19. Total Radial Concrete Ablation

Case	Total Radial Concrete Ablation (cm) in Region					
	1 Sump	2 Inner Pedestal	3 Edge Pedestal	4 Doorway	5 Door Exit	6 Drywell
MELCOR-1-1	19.9	n/a	2.2	0.7	0.2	0.0
MAAP-HP-3-1	64.1	n/a	16.3	21.7	22.6	11.5
MAAP-LP-4-1	58.8	n/a	14.6	20.2	19.2	10.3

Table 20. Total Gas Release

Case	H_2 (moles)	CO (moles)	CO_2 (moles)	SiO_2 (moles)
MELCOR-1-1	37400	3690	10	0
MAAP-HP-3-1	348000	26900	11200	0
MAAP-LP-4-1	345000	26300	7310	0

4.2.4 MELCOR (MELCOR-1-1)

In the MELCOR-1-1 case, the melt quickly forms crusts at the melt-concrete interface, illustrated in Figure 33 for the sump region, where 0 cm elevation corresponds to the bottom of the sump. The interstitial crust acts to insulate the concrete from the melt and reduces or eliminates early concrete ablation. At the start of the CORQUENCH simulation, it is assumed water had already flooded the containment at 15 hours after SCRAM. The melt is readily quenched by the overlying water. The sump region, where the melt pool is the deepest, undergoes the most concrete ablation (13 cm axial, 20 cm radial) and takes the longest (151 minutes) to solidify. The other regions (inner pedestal, pedestal edge, doorway, door exit, and drywell) experience minor concrete ablation and the melt is readily cooled within 63 minutes of CORQUENCH simulation time (Figures 34 and 35).

The radial ablations of the edge pedestal and drywell regions were 2.2 cm and 0.0 cm, respectively. Compared to the pedestal wall thickness, 1.2 m, the predicted undercutting of the pedestal is very minor. Minor concrete ablation is also predicted to have occurred in the doorway region. The thermal boundary layer thickness in the pedestal wall at the end of the simulation is 5.9 cm on the interior wall of the pedestal and 1.6 cm on the outside wall of the pedestal. Thus, the thermal affected zone of the pedestal wall is also minor.

Approximately 37400 moles of hydrogen gas (75.5 kg) and 3690 moles of carbon monoxide (103 kg) are estimated to be produced during the CORQUENCH simulation, Figure 36.

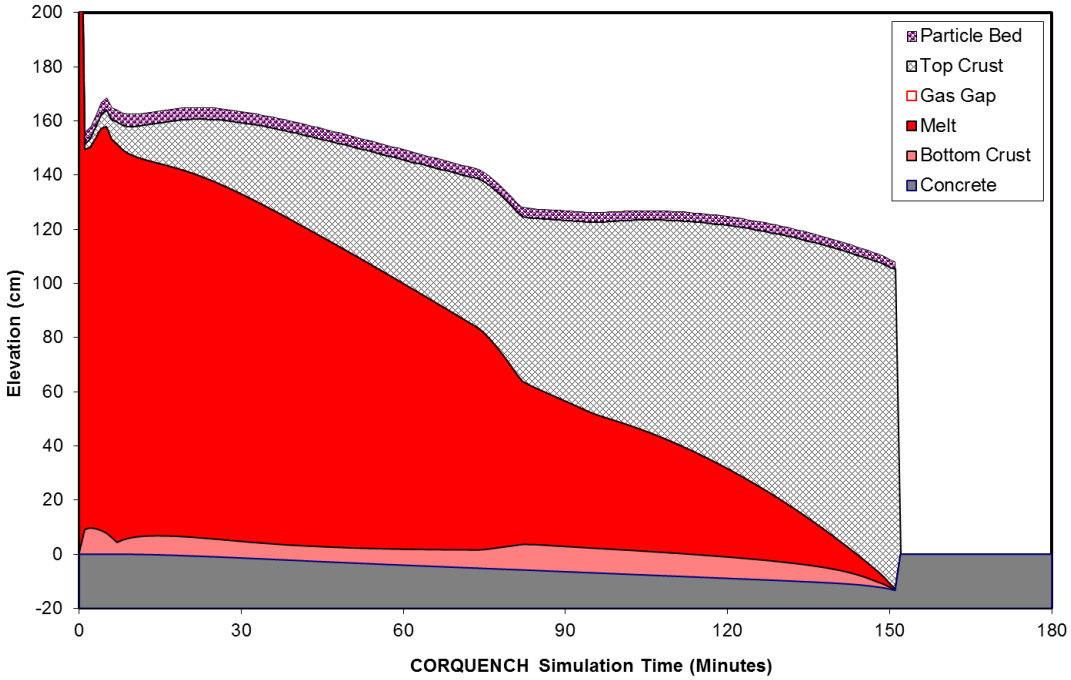

Fig. 33. MELCOR-1-1 Axial Progression and Melt Configuration in Sump Region versus Time.

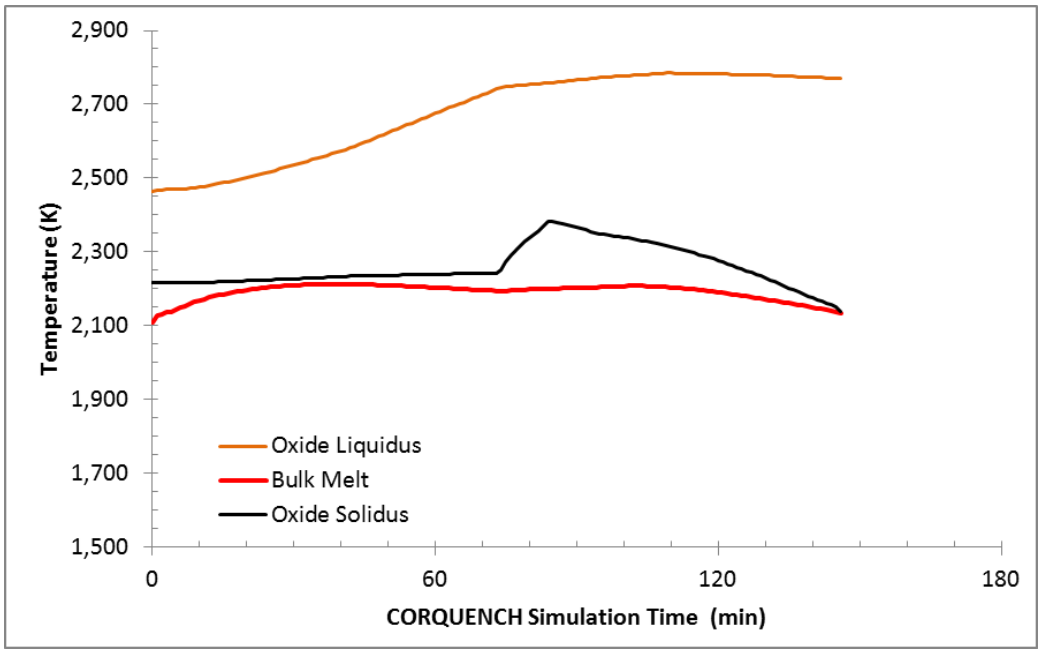

Fig. 34. MELCOR-1-1 Melt Temperature in Sump Region versus Time.

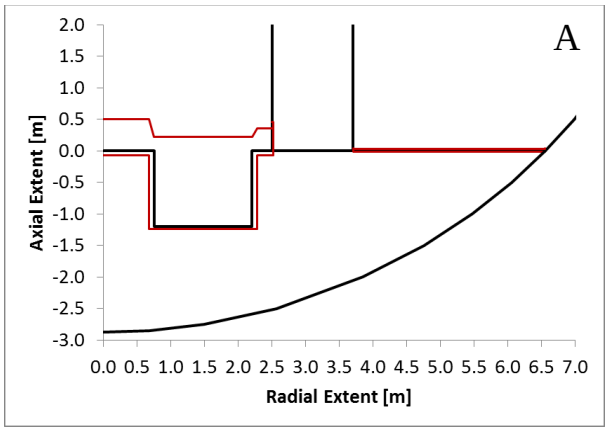

(a) Time = 984.5 min after SCRAM

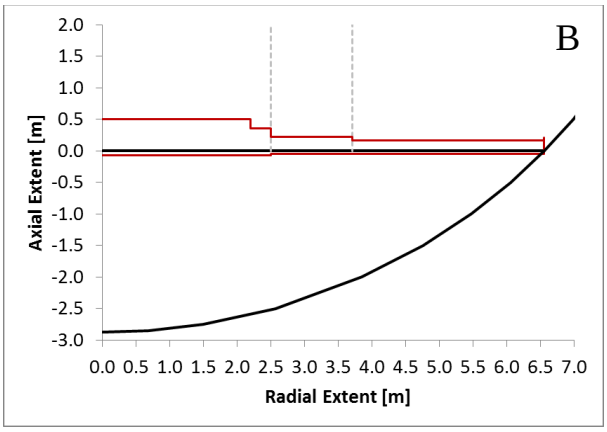

(b) Time = 984.5 min after SCRAM

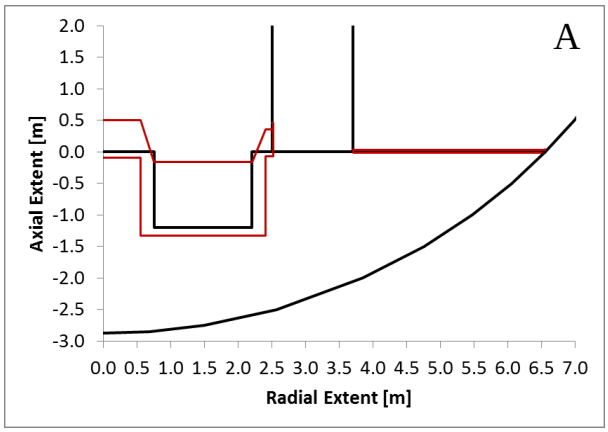

(a) Time = 1075.5 min after SCRAM

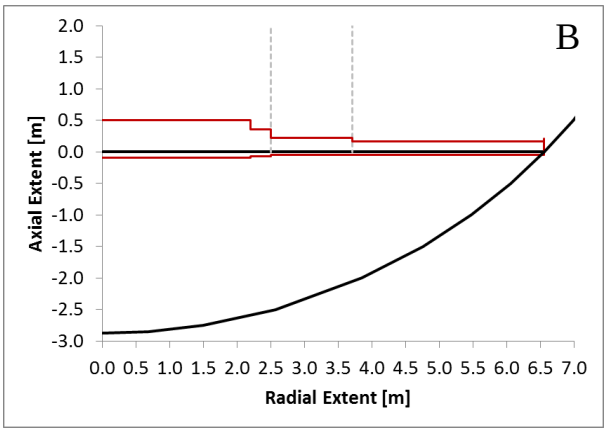

(b) Time = 1075.5 min after SCRAM

Fig. 35. MELCOR-1-1 Cavity Profile for Cross Section A and B after 60 min. of CORQUENCH simulation time and end of simulation.

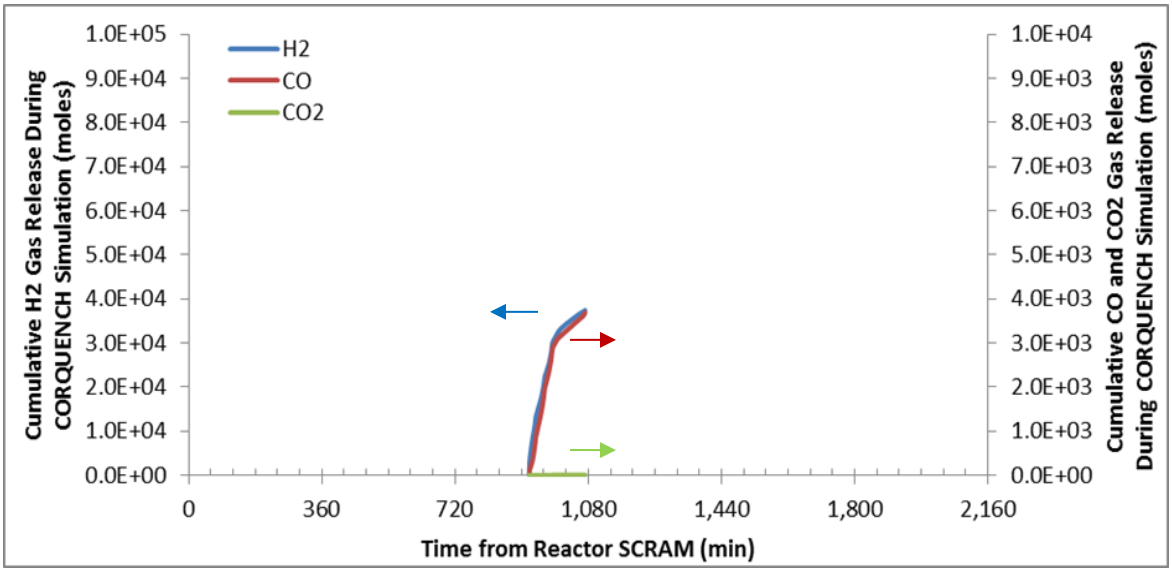

Fig. 36. MELCOR-1-1 Cumulative Gas Released versus Time.

4.2.5 MAAP-HP (MAAP-HP-3-1)

The MAAP-HP case resulted in greater concrete ablation than the MELCOR case. All regions are predicted to be coolable and eventually solidify.

The high initial melt temperature (2443-2763K) prohibits early crust formation at the melt-concrete interface. The sump region is predicted to experience approximately 64 cm of axial and radial concrete ablation before the melt solidifies (Figure 37). This is within the 1.4 m of concrete between the sumps and the steel liner. The melt in the sumps takes nearly 23 hours to solidify after the onset of the melt pour (Figure 38).

The melt in the regions other than the sump are predicted to solidify within 28-88 minutes after water addition at 15 hours. Moderate amounts of concrete ablation, 11.4-23.4 cm, are predicted in these regions (Figure 39).

The radial ablations of the edge pedestal and drywell regions were 16.3 cm and 11.5 cm, respectively. Thus, 23% of the pedestal wall thickness at the base is predicted to have been undercut by concrete ablation. Additional concrete ablation is predicted to have occurred in the doorway region. The thermal boundary layer thicknesses in the pedestal wall at the end of the simulation are 39.9 cm on the interior wall of the pedestal and 38.1 cm on the outside wall of the pedestal. If half of the boundary layers are assumed to be a heat affected zone, then a total of 66.8 cm at the base of the 1.2 m pedestal wall is predicted to have been either ablated away or in a heat affected zone.

A substantial amount of concrete decomposition gases are predicted to have been produced. Approximately 348000 moles of hydrogen gas (703 kg), 26900 moles of carbon monoxide (753 kg), and 11200 moles of carbon dioxide (493 kg) are estimated to have been released into containment during the CORQUENCH simulations, Figure 40.

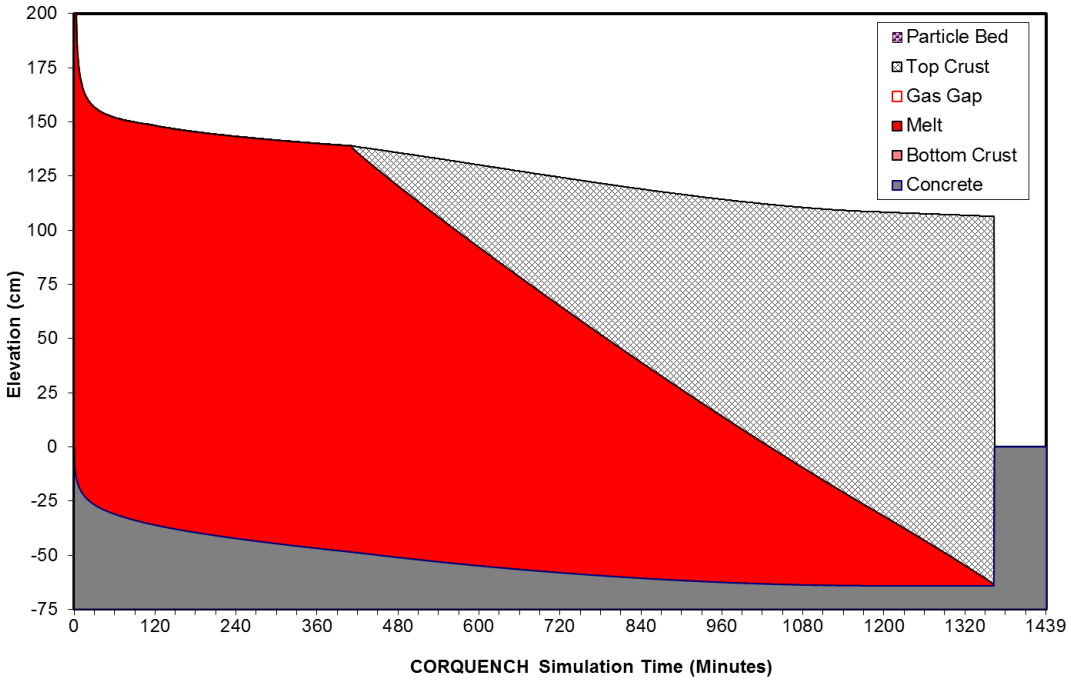

Fig. 37. MAAP-HP-3-1 Axial Progression and Melt Configuration in Sump Region versus Time.

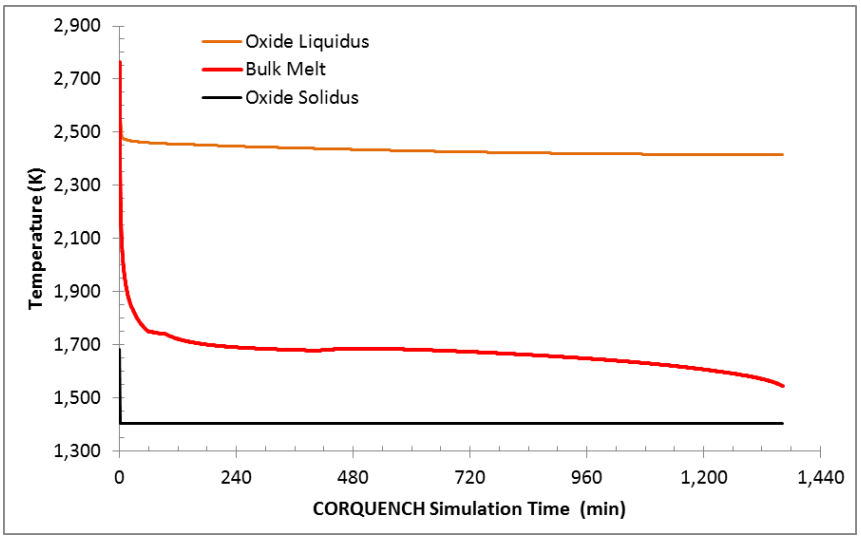

Fig. 38. MAAP-HP-3-1 Melt Temperature in Sump Region versus Time

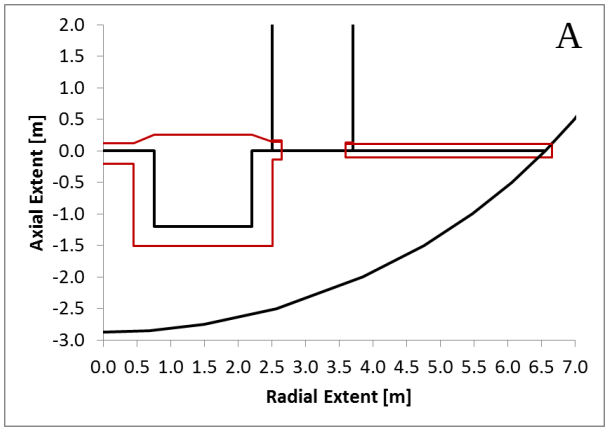

(a) Time = 550.4 min after SCRAM

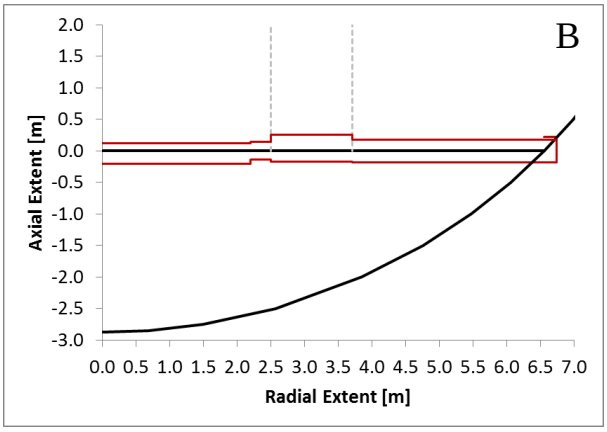

(b) Time = 550.4 min after SCRAM

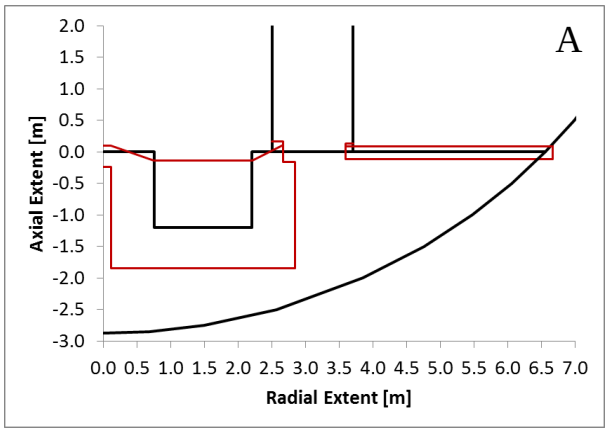

(a) Time = 1852.5 min after SCRAM

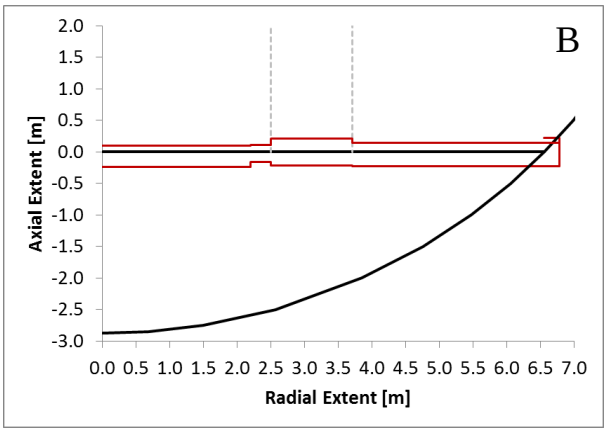

(b) Time = 1852.5 min after SCRAM

Fig. 39. MAAP-HP-3-1 Cavity Profile for Cross Section A and B after 60 min. of CORQUENCH simulation time and end of simulation. *These profiles do not take into account the concrete ablation that occurred during the spreading process as shown in Figure 25.

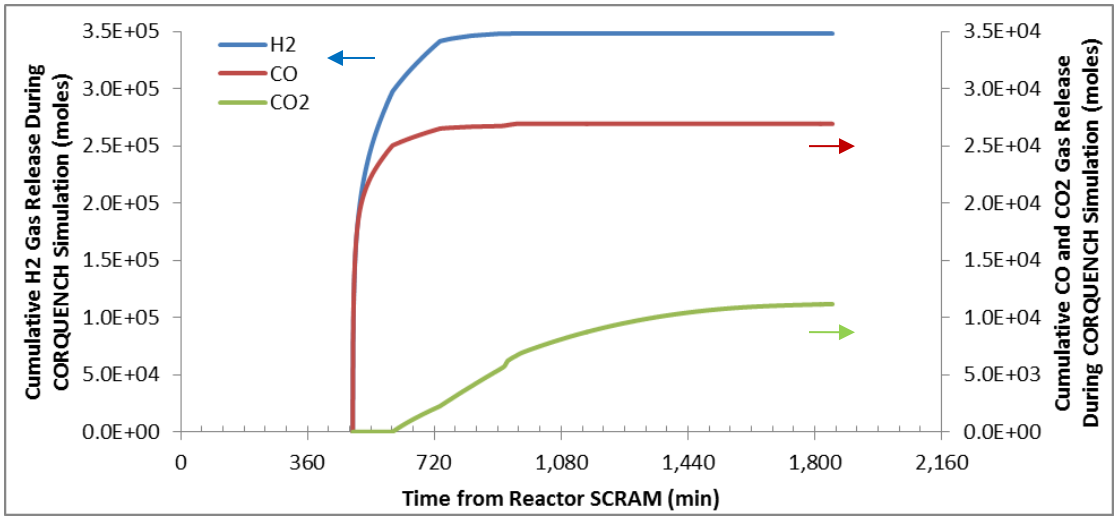

Fig. 40. MAAP-HP-3-1 Cumulative Gas Released versus Time.

4.2.6 MAAP-LP (MAAP-LP-4-1)

The MAAP-LP-4-1 case results are very similar to the MAAP-HP-3-1 case. However, the melt was released approximately 2 hours later than the MAAP-HP case. The reduced time between melt pour and water addition at 15 hours, results in slightly less concrete ablation than the MAAP-HP case. Similar to the MAAP-HP case, all regions are predicted to be coolable and eventually solidify.

The high initial melt temperature (2366-2720 K) prohibits early crust formation at the melt-concrete interface. The sump region is predicted to experience approximately 59 cm of axial and radial concrete ablation before the melt solidifies, Figure 41. This is within the 1.4 m of concrete between the sumps and the steel liner. The melt in the sumps take a little over 19.5 hours to solidify after the onset of the melt pour (Figure 42).

The melt in the regions other than the sump are predicted to solidify within 25-83 minutes after water addition at 15 hours. Moderate amounts of concrete ablation, 10-21 cm, are predicted in these regions.

The radial ablations of the edge pedestal and drywell regions were 14.6 cm and 10.3 cm, respectively. Thus, 21% of the pedestal wall thickness at the base is predicted to have been undercut by concrete ablation. Additional concrete ablation is predicted to have occurred in the doorway region. The thermal boundary layer thickness in the pedestal wall at the end of the simulation is 36.2 cm on the interior wall of the pedestal and 33.8 cm on the outside wall of the pedestal. If half of the boundary layers are assumed to be a heat affected zone, then a total of 59.9 cm at the base of the 1.2 m pedestal wall is predicted to have been either ablated away or in a heat affected zone.

A substantial amount of concrete decomposition gases are predicted to have been produced. Approximately 345000 moles of hydrogen gas (697 kg), 26300 moles of carbon monoxide (737 kg), and 7310 moles of carbon dioxide (322 kg) are estimated to have been released into containment during the CORQUENCH simulations, Figure 43 and 44.

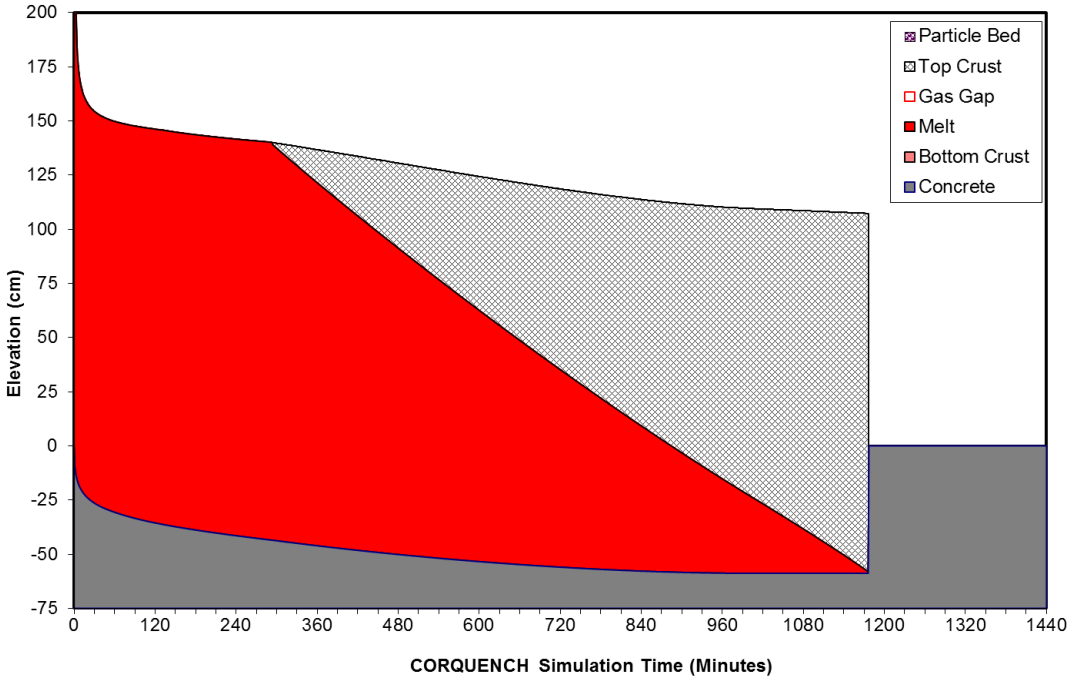

Fig. 41. MAAP-LP-4-1 Axial Progression and Melt Configuration in Sump Region versus Time.

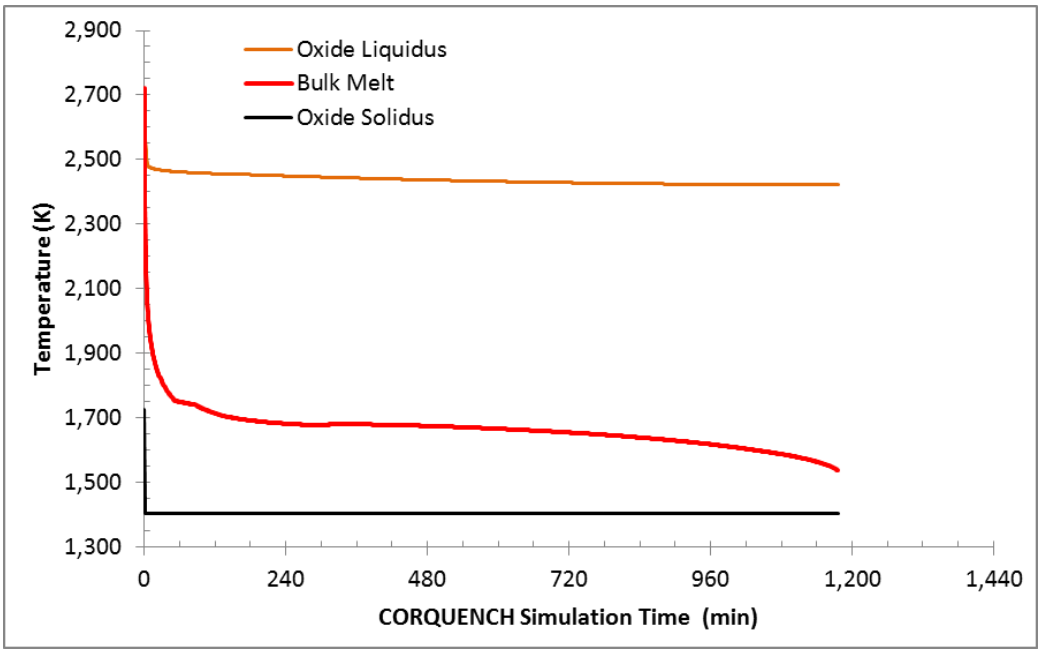

Fig. 42. MAAP-LP-4-1 Melt Temperature in Sump Region versus Time.

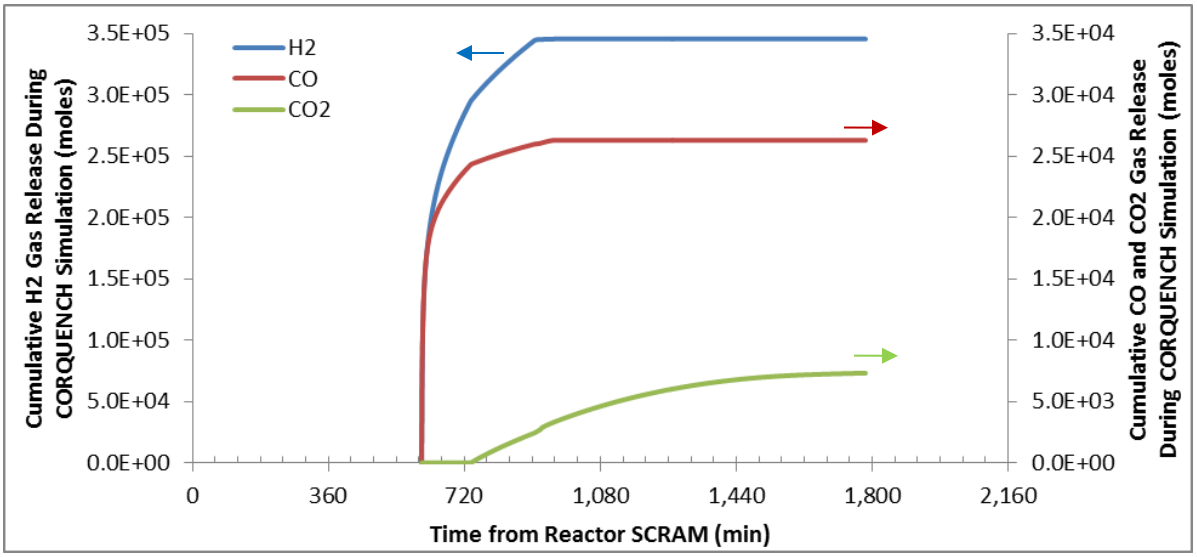

Fig. 43. MAAP-LP-4-1 Cumulative Gas Released versus Time.

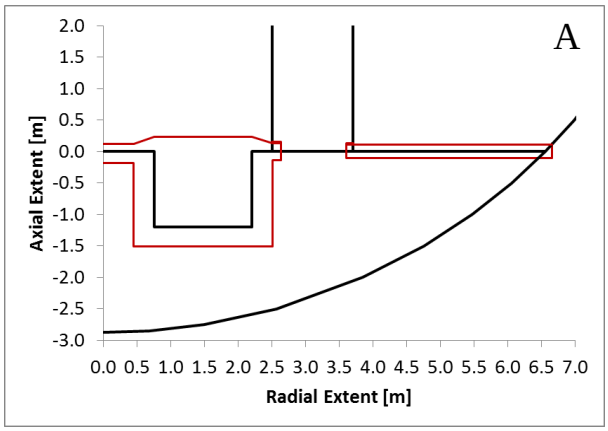

(a) Time = 668.6 min after SCRAM

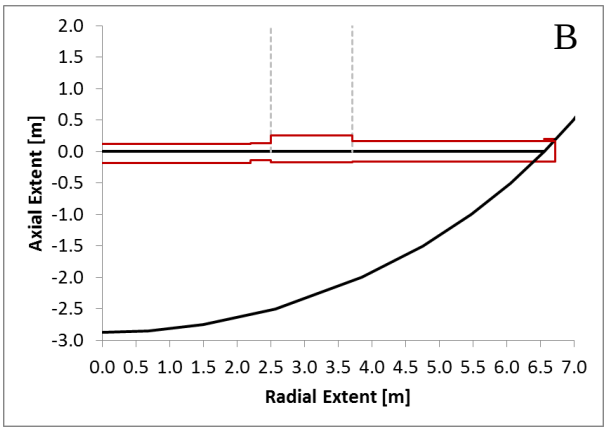

(b) Time = 668.6 min after SCRAM

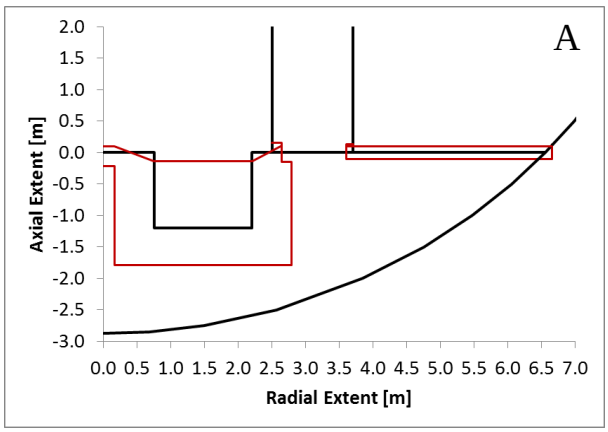

(a) Time = 2068.4 min after SCRAM

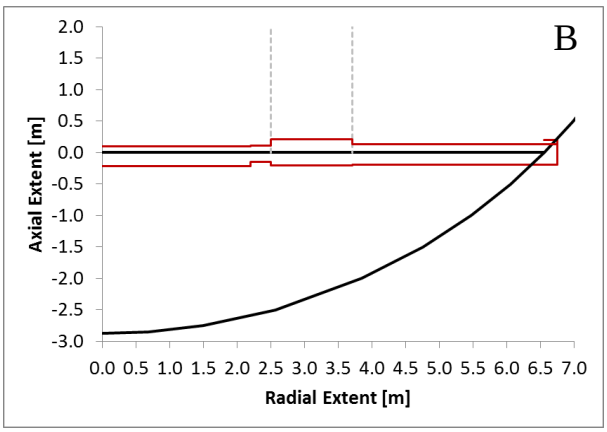

(b) Time = 2068.4 min after SCRAM

Fig. 44. MAAP-LP-4-1 Cavity Profile for Cross Section A and B after 60 min. of CORQUENCH simulation time and end of simulation. *These profiles do not take into account the concrete ablation that occurred during the spreading process as shown in Figure 18.

Melt eruption activity, as evident by a buildup of a particle bed, is predicted to be minor in the MELCOR case and not present in the MAAP cases. Like all siliceous concretes, the basaltic concrete, does not release much gas upon decomposition in comparison to limestone-limestone or limestone-common sand concretes. The reduction in melt eruption activity for low gas containing concretes is consistent with experiment observations [65]. Furthermore, the cavity pressure for these scenarios was quite high (7.5 MPa), which further reduced the melt sparging rate and, thereby, the potential for melt eruptions to occur.

4.2.7 CORQUENCH results for base case simulations

All the MELTSPREAD cases were simulated in CORQUENCH using the base case CORQUENCH options (MELCOR-(1-6)-1, MAAP-HP-(1-4)-1, and MAAP-LP-(1-4)-1). All the MELTSPREAD MAAP cases, including the high pressure and low pressure cases, resulted in similar final configurations. Since the initial conditions in CORQUENCH for each case were similar, the results for MAAP-HP-(1-4)-1 and MAAP-LP-(1-4)-1 cases are very similar to the results presented for the MAAP-HP-3-1 and MAAP-LP-4-1 cases. However, MELTSPREAD predicted different final debris configurations for each of the MELCOR cases.

Previous sensitivity work has shown melt coolability and the total amount of concrete ablation is sensitive to the initial melt depth [16]. Figure 45 illustrates the initial collapsed melt thicknesses presented in Table 11. Among the MELCOR cases, MELCOR-1 had the deepest melt pool in the sump and inner pedestal regions and resulted in the largest amount of concrete ablation in those regions. Similarly, MELCOR-4 had the deepest melt pool the in pedestal edge and doorway regions and resulted in the largest amount of concrete ablation in those regions. The relationship between the initial melt depth and total concrete ablation is illustrated in Figure 46.

By comparing the MELCOR results to the MAAP results in Figure 46, it is clear other factors also impact the total amount of ablation before solidification. Table 21 compares the total axial concrete ablation, as predicted by CORQUENCH, for MELCOR and MAAP cases with similar initial melt depths. The MAAP cases (with initially hotter melt; higher decay heat; and longer time between melt pour and water addition) result in much more ablation than the MELCOR cases. The major difference between the MAAP-HP and MAAP-LP cases is the two hour difference between melt pour timing. The extra two hours between the melt pour and water addition is the primary cause for the slightly higher concrete ablation for the MAAP-HP case.

Table 21. Comparison of Total Axial Concrete Ablation Predicted by CORQUENCH for cases with Similar Initial Melt Depths

	Total Axial Concrete Ablation (cm) in Region					
Case	1 Sump	2 Inner Pedestal	3 Edge Pedestal	4 Doorway	5 Door Exit	6 Drywell
MELCOR-**-1	12.9	7.4	6.9	7.2	4.4	3.2
MAAP-HP-3-1	64.1	23.4	16.2	21.5	22.5	11.4
MAAP-LP-4-1	58.8	21.1	14.4	20.2	19.1	10.1

**sump MELCOR-5-1, inner pedestal MELCOR-5-1, edge pedestal MELCOR-5-1, doorway MELCOR-4-1, door exit MELCOR-4-1, drywell MELCOR-3-1

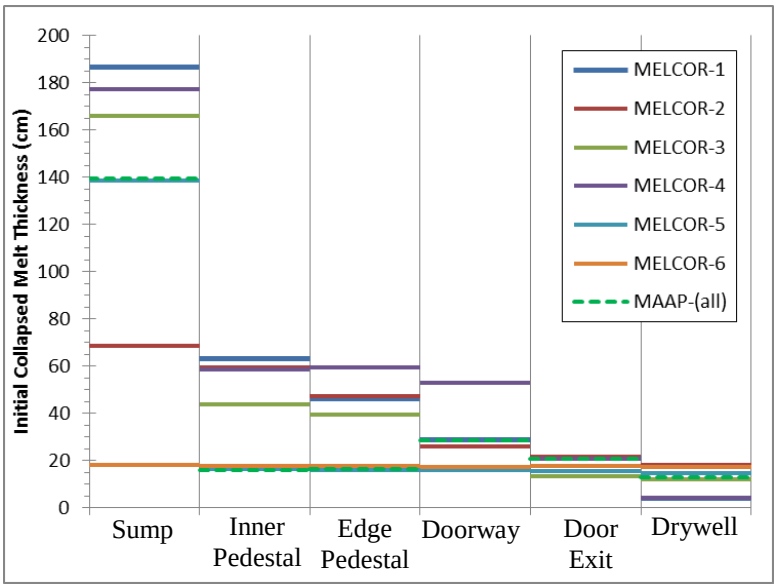

Fig. 45. Initial Collapse Melt Thickness for CORQUENCH MELCOR Scenarios.

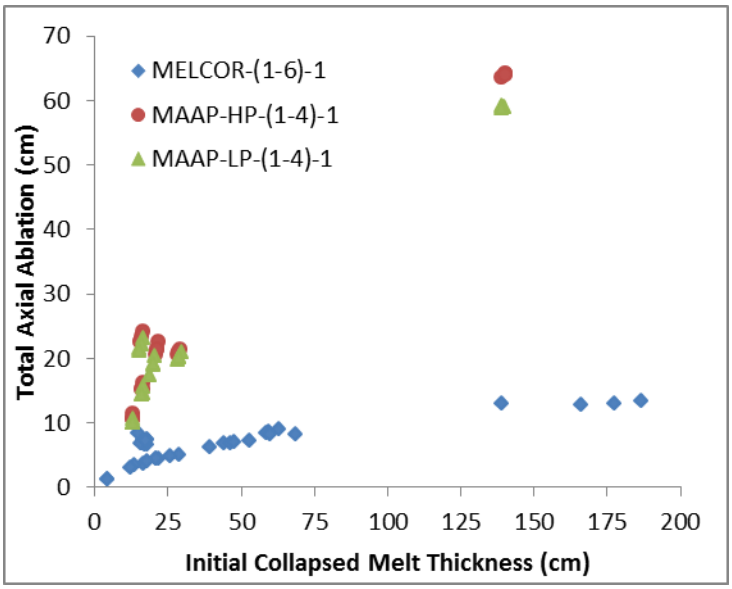

Fig. 46. Total Ablation Depth vs. Initial Melt Thickness.

4.3 PARAMETRIC STUDY RESULTS

Large uncertainties exist for a variety of parameters that would impact the coolability of the melt. This section examines the effects of water addition and ingression, containment pressure, decay heat, and crust anchoring. Furthermore, CORQUENCH has a variety of differing concrete ablation models that will be examined.

4.3.1 Water Addition and Ingression

The base case CORQUENCH results assumed the containment was flooded at 15 hours after SCRAM. It was also assumed that water addition was high enough to keep the debris covered with water. To bound the analysis, the case of no water addition was simulated.

As expected, with no water addition, the melt was predicted not to solidify within the two days of simulation time in CORQUENCH, Table 22. There is considerable ablation in the sump region as well as the other regions. However, the concrete ablation rate in all the regions besides the sump were quite low or zero at the end of the simulation. In the sump region, the ablation rate had slowed to 0.12 mm/min (0.72 cm/hr) by the end of the simulation, Table 23.

Table 22. Impact of Water Injection on Core Melt Progression

Case	Long Term Containment Condition	In Sump Region			Total H_2 Gas Released (kmoles)
		Time to Solidification (min)	Axial Ablation (cm)	Radial Ablation (cm)	
MELCOR-1-1	wet	151	13.4	19.9	37.4
MELCOR-1-2	dry	**2879**	**81.4**	**96.3**	**613**
MAAP-HP-3-1	wet	1362	64.1	64.1	348
MAAP-HP-3-2	dry	**2880**	**87.9**	**87.9**	**348**
MAAP-LP-4-1	wet	1176	58.8	58.8	345
MAAP-LP-4-2	dry	**2879**	**86.6**	**86.6**	**350**

Table 23. Concrete Ablation Rates and the End of Dry Case Simulations

Case	Axial/Radial Ablation Rate at the End of Simulation for Dry Case (mm/min)					
	1 Sump	2 Inner Pedestal	3 Edge Pedestal	4 Doorway	5 Door Exit	6 Drywell
MELCOR-1-2	0.12/0.10	0.00/NA	0.09/0.09	0.02/0.02	0.03/0.03	0.00/7.7*
MAAP-HP-3-2	0.11/0.11	0.00/NA	0.01/0.00	0.01/0.00	0.04/0.00	0.00/0.00
MAAP-LP-4-2	0.11/0.11	0.00/NA	0.01/0.00	0.01/0.00	0.04/0.00	0.00/0.00

*This region contained 4 cm of melt and cooled quite rapidly, the final ablation rate reported during this rapid transient is not representative of the final state

For cases where the cavity is flooded, the deep melt pool in the sump is predicted to quench primarily due to water ingression into the top crust. Without water ingression, a conduction limited crust would form on top the melt. The maximum conduction limited crust thickness, δ_{cl}, can be estimated by the following equation where k_{cr} is the crust thermal conductivity, ΔT is the temperature difference across the crust and $\dot{q}$ is the volumetric heat generation in the melt [78].

$$\delta_{cl} = \left(\frac{2 \cdot k_{cr} \cdot \Delta T}{\dot{q}}\right)^{1/2}$$

The estimated conduction limited crust thicknesses for the sump region are given in Table 24. Codes such as CORCON-Mod3 (in MELCOR) that do not model the water ingression phenomenon cannot quench deep melt pools without modifying the melt properties, e.g. increasing the thermal conductivity by an order of magnitude. Although not included in the parameter study, simulations performed with an impervious crust would be bound by the wet and dry cases.

Table 24. Conduction Limited Crust Thickness Estimates

Case	Melt Decay Heat at Time after SCRAM (W/kg UO_2) @ (hr)	Melt Decay Heat (kW/m^3)	Conduction Limited Crust Thickness* (cm)
MELCOR	106 @ 15	380	16.3
MAAP-HP	125 @ 8.5	447	15.0
MAAP-LP	118 @ 10.5	427	15.4

*Estimated based on ΔT of 1259 K [1700 K (assumed melt freezing temperature) – 441 K (saturation temperature)] and a crust thermal conductivity of 4 W/m K

4.3.2 Containment Pressure

The Unit 1 containment pressure varied between 0.84 and 0.74 MPa absolute from 12-22 hours after SCRAM [79]. In the long term, 168-270 hours after SCRAM, the pressure decreased to 0.17 MPa absolute [79]. As noted earlier, the containment pressure impacts the water saturation temperature, melt gas sparging rate due to core-concrete interaction, as well as the top crust dryout limit due to water ingression. In terms of the debris coolability models, increasing pressure reduces the potential for, and intensity of, the melt eruption cooling mechanism [12], while the effectiveness of the water ingression cooling mechanism increases with increasing pressure.[4] Thus, changes in containment pressure during the sequence will cause the relative contributions of these two cooling mechanisms to fluctuate in opposing directions.

CORQUENCH uses a constant, user specified, containment pressure throughout the duration of a simulation. Thus, the time dependent variation of the containment pressure and the variation in the contribution of these two cooling phenomena are not captured as part of this study. This analysis also does not take into account the influence of the containment pressure on phenomena beyond the debris, such as the condensation rate on the drywell liner. To investigate the impact of the containment pressure on melt coolability, cases were performed with a containment pressure of 0.35 MPa absolute.

Table 25 illustrates the impact of containment pressure on the MCCI. A reduction in containment pressure slightly decreased the melt coolability delaying the time to melt solidification and increasing the total amount of concrete ablation. The results suggest that as the Unit 1 accident progressed and the containment pressure decreased, the dry-out heat flux of the debris would decrease resulting in less favorable conditions for debris stabilization. However, the debris is still predicted to be coolable.

[4] Based on the Ricou-Spalding melt entrainment model [12], the melt entrainment rate due to eruptions scales roughly with the inverse of the square root of containment pressure. According to the Lomperski-Farmer water ingression model [54], the crust dry out limit scales roughly with containment pressure raised to the 5/13 power.

Table 25. Impact of Containment Pressure on Core Melt Progression

Case	Pressure (MPa abs.)	In Sump Region			Total H_2 Gas Released (kmoles)
		Time to Solidification (min)	Axial Ablation (cm)	Radial Ablation (cm)	
MELCOR-1-1	0.75	151	13.4	19.9	37.4
MELCOR-1-3	0.35	174	21.2	24.6	45.1
MAAP-HP-3-1	0.75	1362	64.1	64.1	348
MAAP-HP-3-3	0.35	1739	67.0	67.0	346
MAAP-LP-4-1	0.75	1176	58.8	58.8	345
MAAP-LP-4-3	0.35	1529	61.7	61.7	337

4.3.3 Melt-Concrete Crust Formation and Concrete Ablation Modeling

CORQUENCH contains three concrete ablation models [12]. The first is a quasi-steady ablation model where all the heat transferred to the concrete is applied towards decomposing the concrete. This model is the same as that employed in CORCON-Mod3 (MELCOR). The second model tracks the thermal boundary layer in the concrete, liberating water and other concrete decomposition products in the concrete as the thermal boundary layer passes through. In this model, the thermal boundary layer is initialized as fully developed. The third model tracks the transient development of the thermal boundary layer in the concrete. The third model also models crust formation at the melt-concrete interface. Predicting this interstitial crust has been essential in validation efforts against experimental data [12].

Table 26, for wet conditions, and Table 27, for dry conditions, compare the melt progression results in the sump region for the quasi-steady ablation model (Model 1) and the transient model with interstitial crust formation (Model 3). The high initial melt temperature of the MAAP cases prevented the formation of interstitial crusts. Therefore, the difference between the MAAP cases is due to the difference in ablation model. The quasi-steady ablation model results in 11%-18% greater ablation. However, only

Table 26. Impact of Interstitial Crust Formation and Ablation Model on Core Melt Progression – Wet Cases

Case	Crust and Ablation Model	In Sump Region			Total H_2 Gas Released (kmoles)
		Time to Solidification (min)	Axial Ablation (cm)	Radial Ablation (cm)	
MELCOR-1-1	Model 3	151	13.4	19.9	37.4
MELCOR-1-4	Model 1	131	28.9	28.5	141
MAAP-HP-3-1	Model 3	1362	64.1	64.1	348
MAAP-HP-3-4	Model 1	1388	75.0	75.0	293
MAAP-LP-4-1	Model 3	1176	58.8	58.8	345
MAAP-LP-4-4	Model 1	1206	69.5	69.5	271

Table 27. Impact of Interstitial Crust Formation and Ablation Model on Core Melt Progression – Dry Cases

Case	Crust and Ablation Model	In Sump Region			Total H_2 Gas Released (kmoles)
		Time to Solidification (min)	Axial Ablation (cm)	Radial Ablation (cm)	
MELCOR-1-2	Model 3	**2879**	**81.4**	**96.3**	**613**
MELCOR-1-7	Model 1	**2879**	**106.2**	**106.2**	**623**
MAAP-HP-3-2	Model 3	**2880**	**87.9**	**87.9**	**348**
MAAP-HP-3-7	Model 1	**2880**	**97.6**	**97.6**	**334**
MAAP-LP-4-2	Model 3	**2879**	**86.6**	**86.6**	**350**
MAAP-LP-4-7	Model 1	**2879**	**96.2**	**96.2**	**335**

the gases in ablated concrete are released in the quasi-steady ablation model which results in less oxidation of the melt and less flammable gas generation. The relatively cool melt of the MELCOR case results in the formation of interstitial crusts when this modeling option is used. These interstitial crusts act to insulate the concrete early in the transient. Eventually the interstitial crust re-melts and concrete ablation progresses uninhibited. The combined effect of the interstitial crusts and transient ablation model results in much less ablation during the early portion of the melt cooling transient for the MELCOR case.

Melt progression predictions with tools that use a quasi-steady ablation model (e.g. CORCON-Mod3) will predict greater concrete ablation than tools that capture the transient process. In addition, for cases where the melt pour from the RPV is cool, relative to the freezing point, tools which cannot predict the formation of interstitial crusts at the melt-concrete interface (e.g. CORCON-Mod3) will predict greater concrete ablation.

4.3.4 Decay Heat Level

The decay heat in the melt may be reduced by the volatilization of the radionuclides. To investigate the impact of reduced decay heat, the melt decay heat (see Figure 31) was reduced by 25%. The 25% decay heat reduction is also approximately equivalent to an additional decay time of 22 (MELCOR cases), 15 (MAAP-HP cases), and 18 (MAAP-LP cases) hours.

As to be expected, the decrease in decay heat increased the melt coolability. In the sump region, the reduction in decay heat resulted in the melt solidifying earlier with reduced concrete ablation as summarized in Table 28. For the MAAP cases, where no interstitial crust formed and there was a long core-concrete interaction, the 25% reduction in decay heat resulted in approximately 15% reduction in concrete ablation in the sump region. For the MELCOR case, in which an interstitial crust formed and the melt solidified in a couple hours, the reduction in decay heat had a minor impact on the melt cooling and concrete ablation in the sump region.

Future analyses of the core-concrete interaction should consider the reduced debris decay heat due to the volatilization of the radionuclides.

Table 28. Impact of Decay Heat Level on Core Melt Progression

Case	Decay Heat	In Sump Region			Total H_2 Gas Released (kmoles)
		Time to Solidification (min)	Axial Ablation (cm)	Radial Ablation (cm)	
MELCOR-1-1	100%	151	13.4	19.9	37.4
MELCOR-1-5	75%	151	13.5	13.6	32.9
MAAP-HP-3-1	100%	1362	64.1	64.1	348
MAAP-HP-3-5	75%	1121	53.9	53.9	345
MAAP-LP-4-1	100%	1176	58.8	58.8	345
MAAP-LP-4-5	75%	957	49.9	49.9	342

4.3.5 Crust Anchoring to Concrete Surfaces

Crust anchoring to the concrete sidewalls and subsequent separation of the crust from the melt pool was disabled for the base case (-1) model setup. A majority of the tests in Table 2 have experienced some crust attachment and anchoring to the test section walls. The large MACE M1b test, at 1.2 x 1.2 m, also experienced crust anchoring. However, a portion of the crust eventually failed and relocated downwards [75]. The sumps in Unit 1 are 1.45 × 1.45 m. To investigate the possibility of crust anchoring, simulations were conducted with the model enabled.

The equation below is the minimum crust thickness to enable crust anchoring for the case where there is no particle bed and the mass of water over the crust is not taken into account in the crust loading. The macroscopic crust mechanical failure strength, $\sigma_{cr,f}$, used in the anchoring analysis was set at 3.0 MPa based on the measurements and data assessment made as part of the OECD/MCCI program [4]. The constant, C_{geom}, in the crust mechanical strength model can vary from 2.53-8.84 depending on the failure mode, geometry and the edge conditions. The value was set to 4.71 representative of a ductile failure of a circular crust with simply supported edges. The other parameters in the equation include gravity, g, the crust density, ρ_{cr}, and the basemat area, A_b. For the geometry of the sumps, pedestal, and doorway, the equation predicts the minimum crust thickness is 0.87 cm, 8.2 cm, and 0.50 cm, respectively, assuming a crust density of 6000 kg/m^3.

$$\delta_{t,min} = \frac{\rho_{cr} \cdot A_b \cdot g}{C_{geom} \cdot \sigma_{cr,f}}$$

As noted, C_{geom} can vary from 2.53-8.84 for various geometry and failure modes resulting in a 2x variation in the predicted minimum crust thickness for crust anchoring. In addition, the measured macroscopic crust strength of large post-test crust ingots range from approximately 0.9-4 MPa and measurements of in-situ crust strengths, at temperature and during MCCI, range from approximately 0.2-1 MPa [4].

Crust anchoring was predicted to occur in a number of the cases. For cases where crust anchoring occurred, there was continued concrete ablation after two days of simulation time, Table 29. Crust anchoring was predicted to occur in the sumps for every case. Most of the inner pedestal regions were also predicted to have crust anchoring. However, this region was modeled using a 1-D geometry and the crust is predicted to attach to 'walls' that are not present in reality. Thus, the results for the inner pedestal region are not representative. As the edge pedestal region is modeled as a 2-D cylinder with the dimensions of the actual pedestal, this region provides a more accurate prediction of crust anchoring within the pedestal. Only MELCOR cases 1-4 are predicted to anchor in the edge pedestal region. The larger initial melt depth for these cases allows for a crust to develop that is thick enough to support itself. Finally, crust anchoring is predicted to occur in the doorway. Like the sumps this region consists of a

small area confined by walls. However, there are only two walls and the other 'walls' are debris in the neighboring regions. The unique boundary conditions of this region are only captured in basic detail.

It is currently believed crust anchoring and separation of the melt pool from the crust is unlikely at the pedestal scale. However, the possibility exists for crust anchoring in the sumps.

Table 29. Impact of Crust Anchoring on Core Melt Progression

Case	Crust Anchoring Enabled	In Sump Region			Total H_2 Gas Released (kmoles)
		Time to Solidification (min)	Axial Ablation (cm)	Radial Ablation (cm)	
MELCOR-1-1	no	151	13.4	19.9	37.4
MELCOR-1-6	yes	**2879**	**51.2**	**65.6**	**305**
MAAP-HP-3-1	no	1362	64.1	64.1	348
MAAP-HP-3-6	yes	**2880**	**86.8**	**86.8**	**348**
MAAP-LP-4-1	no	1176	58.8	58.8	345
MAAP-LP-4-6	yes	**2879**	**85.1**	**85.1**	**347**

4.4 CORQUENCH RESULTS SYNTHESIS

Figures 47-51 present ex-vessel core melt progression predictions relative to the Unit 1 SCRAM timing. The case where the decay heat is reduced by 25% (Case 5 in Table 15) and the case where no water is added (Case 2 in Table 15) are presented. These two cases bound all the CORQUENCH simulations performed except for the cases which used the quasi-steady ablation model (Case 4 and Case 7). Case 4 and 7 simulations were only performed to investigate the influence of this modeling option which is the only available option in other tools (CORCON-Mod 3). Case 1 and Case 3 is closer to the Case 5 results, whereas Case 6, where crust anchoring is allowed, is more similar to Case 2 results.

The wet and dry MAAP and the dry MELCOR cases generate sufficient hydrogen and carbon monoxide during the MCCI to support deflagration or an explosion at the 24.8 hour point, Figures 47, 48. The wet MELCOR case did not produce much hydrogen or carbon monoxide during the MCCI simulation; however, this case produced over 700 kg of hydrogen during the in-vessel degradation phase [1]. Thus, all simulations generate enough flammable gas to support an explosion at 24.8 hours.

The closest distance between the corner of the sump and the drywell liner is approximately 1.4 m. Approximately 1 m of radial and axial ablation in the sump would be required to reach the liner. If water was added at 15 hours at a sufficient rate to offset the decay heat, the simulations predict the melt was quenched before reaching the underlying drywell liner. In the extreme case of no water addition, it would take over two days of MCCI in the sumps for the melt to reach the liner. There are several additional meters of concrete below the liner before ground is reached.

Figure 51 provides the results of the total pedestal wall thickness that is ablated away from melt in the edge pedestal and drywell regions. The wall is 1.2m thick. With water addition, the pedestal wall is predicted to experience less than 25 cm of concrete ablation for the MAAP cases and only minor ablation for the MELCOR case. Even without water addition, it is predicted that the upward heat transfer from the MAAP cases is sufficient to offset the decay heat. For the dry MELCOR case, the melt depth in the pedestal edge region is approximately twice the depth as the MAAP cases. The upward heat removal to the containment atmosphere is not sufficient to remove the decay heat and continued radial (as well as axial) concrete ablation occurs. As previously mentioned, CORQUENCH does not model the structural integrity of the pedestal. As expected, if no water was added and there was a deep melt pool in the pedestal (e.g. >20 cm) the pedestal wall may not remain structurally sound over the long term.

Finally, the CORQUENCH calculations predict that even though very deep melt pools may have formed during the 1F1 accident due to very high predicted core release fractions [1, 2], the debris is

coolable. This is primarily due to two factors. First, the decay heat is relatively low several hours after SCRAM. Most of the MCCI experiments to date, Table 2, have simulated decay heat levels that are representative of two hours of decay time after SCRAM. The decay heat level in the current simulations, Table 24, are approximately 1/3 that of the previous experimental and analysis focus. Second, the debris dryout heat flux, as predicted by the Lomperski and Farmer model [54], is augmented by the high containment pressure (scales as 5/13 with containment pressure). However, the dryout limit is reduced by the addition of concrete oxides. For the MELCOR cases, there was very limited or no concrete ablation and the dryout limit remained high. For the MAAP cases, there was concrete ablation with considerable ablation occurring in the sump region resulting in a reduced dryout limit. However, as the concrete was ablated in the sumps, the cross sectional area in contact with the overlying water increased. For both the MELCOR and MAAP cases, the net effect of these factors resulted in dryout limits which were high enough to remove the decay heat even for the deep melt pools in the sump region. It should be noted that the water ingression model was adapted from theory developed for the field of volcanology and has been successfully compared to field data of the cooling of several meters of lava [80]. In addition, the trends in the dryout heat flux (pressure and concrete content) are supported by the results of the reactor-material SSWICS test series [54].

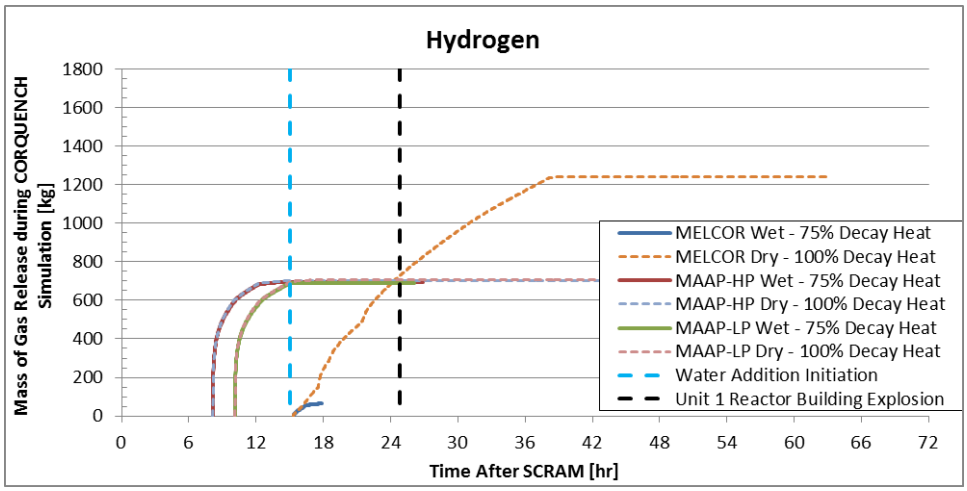

Fig. 47. Total Hydrogen Generation during MCCI (some curves overlap).

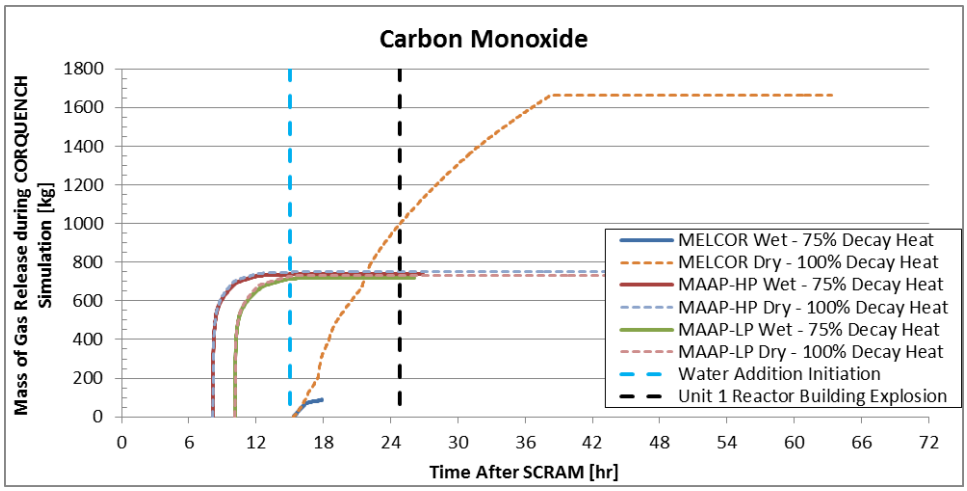

Fig. 48. Total Carbon Monoxide Generation during MCCI (some curves overlap).

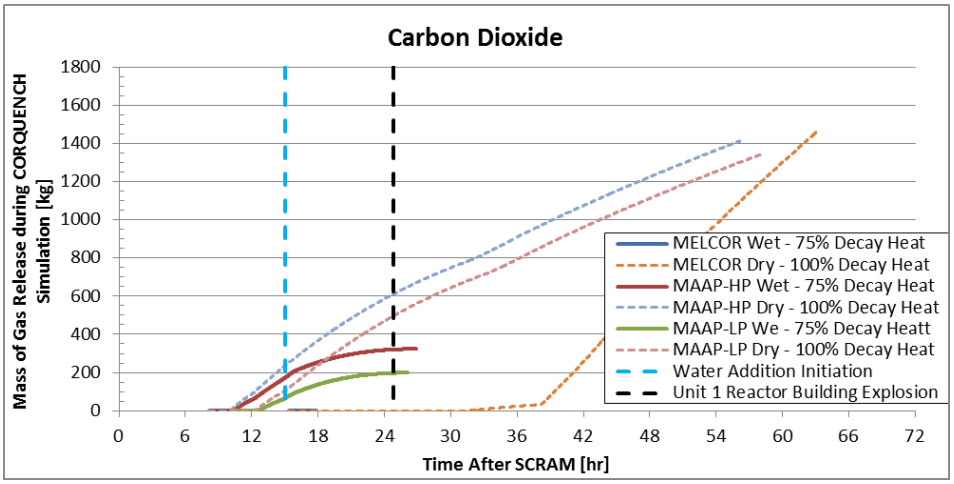

Fig. 49. Total Carbon Dioxide Generation during MCCI.

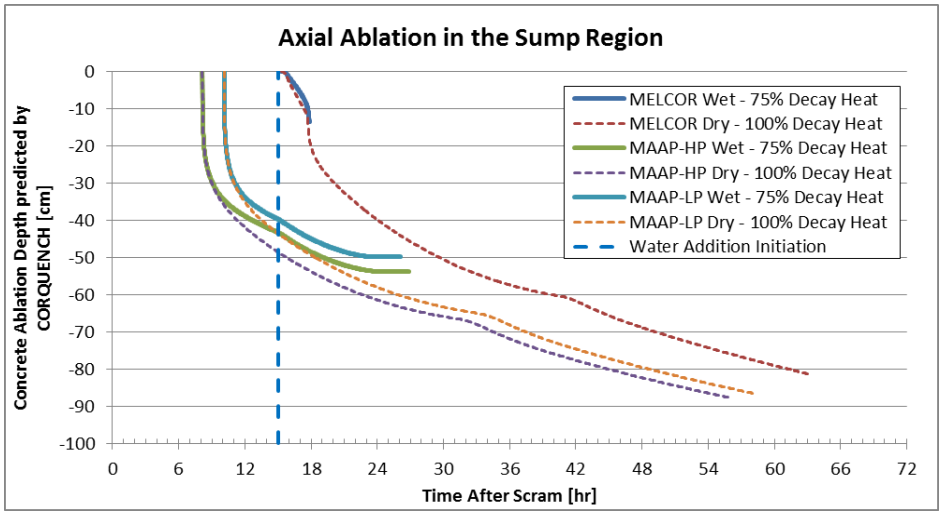

Fig. 50. Total Axial Ablation in the Sump Region during MCCI.

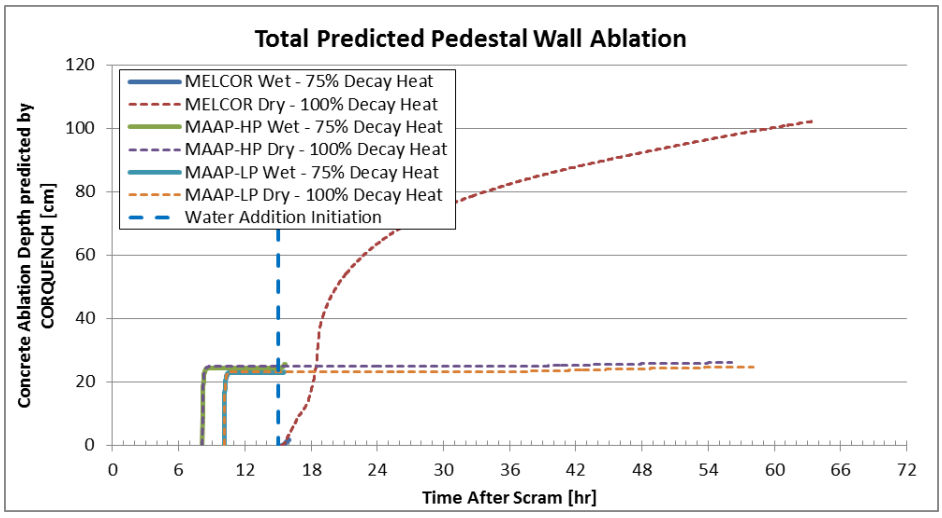

Fig. 51. Total Pedestal Wall Ablation during MCCI (some curves overlap).

4.5 COMPARISON OF CORQUENCH RESULTS TO OTHER WORK

Figure 52 and 53 compares the total gas released for the CORQUENCH MELCOR-1-5 (Wet, 25% decay heat reduction) and MELCOR-1-2 (dry, 100% decay heat) against the predictions by the MELCOR code. The data for the MELCOR code results were taken from Fukushima Daiichi Accident Study [1]. Both used the same initial melt pour timing and mass. As noted earlier, the melt temperature in the CORQUENCH MELCOR simulations was artificially increased to 2110 K. The MELCOR code results assume water was injected starting 15 hours after SCRAM at a rate of 3 kg/s until approximately 24 hours after SCRAM. Water injection resumes at 28 hours at a rate of 17 kg/s until approximately 57.5 hours and reinstated around 81 hours, see report for details [1]. The MELCOR code predicted long term, continued MCCI. The high rate of water injection between 28 and 57.5 hours does not appear to affect the MCCI progression in MELCOR. If sufficient water was added, CORQUENCH predicts the melt was readily quenched. In the bounding case of no water addition and 100% decay heat, CORQUENCH predicts much less flammable gas generation over a shorter interval.

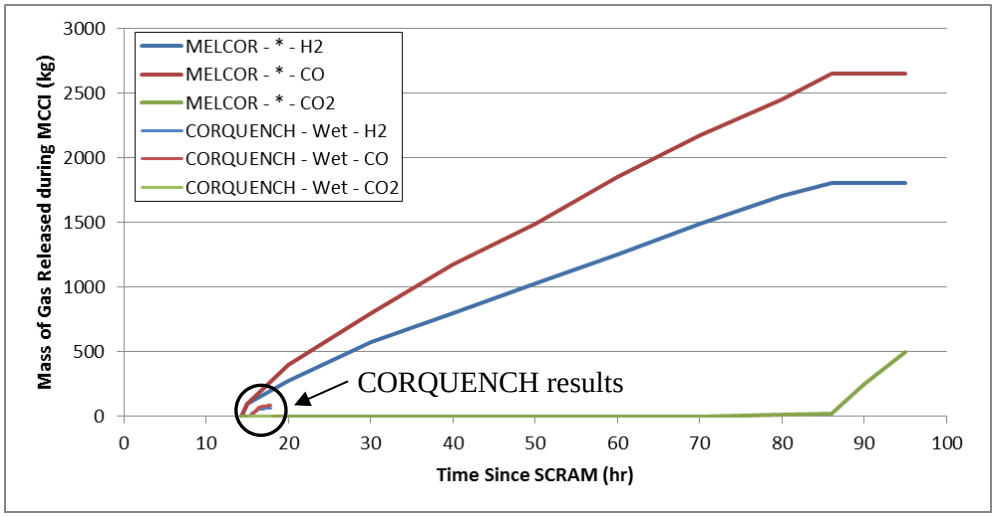

Fig. 52. Gas Production Comparison of CORQUENCH wet case vs. MELCOR.

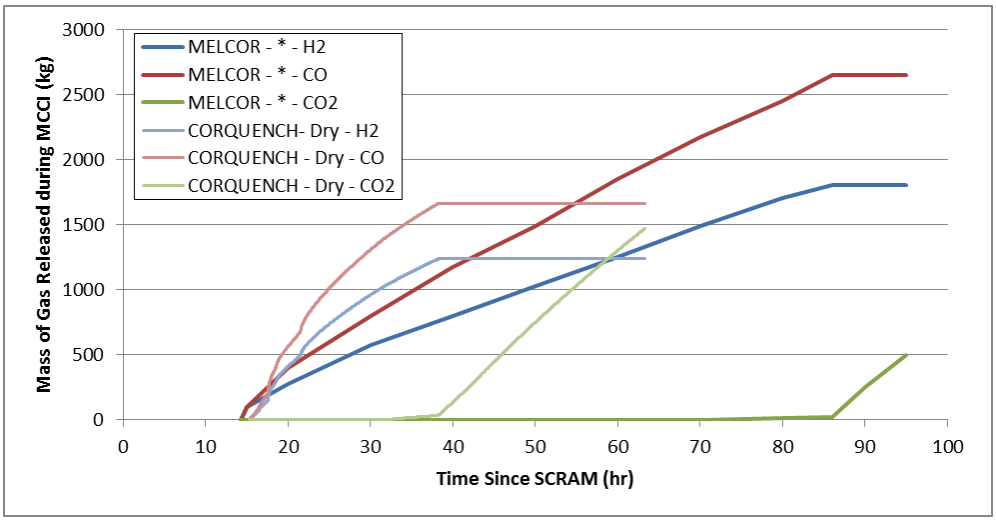

Fig. 53. Gas Production Comparison of CORQUENCH dry case vs. MELCOR.

TEPCO performed MCCI simulations of the sump region using MAAP [81]. The simulation conditions included melt relocation at 15 hours, 81cm of melt in the 1.2 cm deep sumps, a 20% reduction in decay heat due to radionuclide volatilization and water was present above the sump debris. The simulations predicted the melt solidified within the sump after 65 cm of axial and radial ablation.

Table 30 compares the final ablation depths in the sump for the simulation performed by TEPCO using MAAP4 [81] and the simulation results for some of the cases performed as part of this study. Most of the simulations performed in this study have melt depths greater than 81 cm in the sump region. This is the result of the sump plates failing during the melt pour and subsequently filling with debris. The melt pour timing as well as the decay heat level is also slightly different, and a one-to-one comparison is not possible. However, in general, the predicted ablation in the sump region of the TEPCO-MAAP4 simulation compares reasonably well with the simulations where water was added and crust anchoring in the sump region was prohibited. When crust anchoring is enabled in CORQUENCH, which is a phenomenon not modeled in MAAP, the simulations predict crust anchoring occurs in the sumps and the melt does not solidify after two days of simulated time.

Table 30. Comparison of Simulation Results to TEPCO-MAAP Results

Simulation	Relocation Timing (hrs)	Decay Heat Level (%)	In Sump		
			Initial Melt Thickness (cm)	Total Axial Ablation (cm)	Total Radial Ablation (cm)
MAAP4-TEPCO [80]	15	80	81	65	65
MELCOR-1-5	14.27	75	187	13.5	13.6
MELCOR-2-5	14.27	75	69	7.7	3.1
MAAP-HP-3-5	8.14	75	140	53.9	53.9
MAAP-LP-4-5	10.11	75	139	49.9	49.9
MELCOR-1-6	14.27	100	187	**51.2**	**65.6**
MELCOR-2-6	14.27	100	69	**15.4**	**21.7**
MAAP-HP-3-6	8.14	100	140	**86.8**	**86.8**
MAAP-LP-4-6	10.11	100	139	**85.1**	**85.1**

*Values noted in bold are the results for cases where the debris has not fully solidified before the end of the simulation (2 days of simulated time in CORQUENCH).

5. SUMMARY AND CONCLUSIONS

The MELCOR [1] and MAAP [2] simulation results for Unit 1 span a wide range of melt pour conditions from the RPV ranging from a gradual pour of low-temperature core debris (MELCOR), to a rapid pour of high temperature melt (MAAP). Since cavity conditions during the accident are uncertain, a sensitivity study was carried out with MELTSPREAD to evaluate the effect of the presence or absence of water on the cavity floor, melt pour rate and temperature, and sump cover plate failure on the global spreading behavior. A parameter study was also conducted with CORQUENCH to evaluate the effect of the presence of water, cavity pressure, decay heat level, and modeling options on the long term coolability of the melt.

The results of the MELTSPREAD analysis predict quite different behavior depending upon the pour scenario. For the low-temperature gradual MELCOR pour, the code predicts lethargic spreading of a highly viscous melt over a period of approximately 4000 seconds. Concrete ablation is minimal in these cases since the high viscosity limits convection from the melt to the underlying concrete. Despite the low flow rate, in all cases the melt is predicted to eventually spread out of the pedestal doorway and contact the liner. MELTSPREAD predicts that the liner does not fail in this location for the MELCOR simulations. When water is present, the core debris spreading is limited to a total of approximately 33 m^2.

For the high temperature MAAP pours, MELTSPREAD predicted the sump plates rapidly ablated through in less than 5 seconds. Furthermore, the concrete erosion during spreading was significant with approximately 2 m^3 in the first 2 minutes with a maximum ablation depth of about 20 cm outside the pedestal door. The melt was also predicted to fully cover the pedestal and drywell annulus floor areas which sum to approximately 111 m^2. Both low and high-pressure MAAP pour sequences were analyzed. The drywell liner was predicted to remain intact for all low-pressure wet cases, and to fail by erosion due to impingement heat transfer from the melt for the high pressure cases. However, the analysis did not take into account additional failure modes such as creep rupture.

The best-estimate results of the long-term debris coolability analysis with CORQUENCH assumed sufficient water was injected into containment to cover the debris starting 15 hours after shutdown. Under this condition the simulations indicate that the melt was coolable over the long term. The predicted concrete ablation was less than that necessary to reach the liner through downward melt progression. The MELCOR case, which contained relatively cool melt, readily cooled within 2.5 hours after relocation with limited concrete ablation in the sump regions (~18 cm) and less than 10 cm ablation elsewhere. Seventy-six kilograms of hydrogen and 103 kilograms of carbon monoxide were predicted to be generated during core-concrete interactions. The MAAP cases, which contained relatively hot melt, cooled approximately 22.5 hours after melt relocation and resulted in 65 cm of concrete ablation in the sump region and less than 23 cm elsewhere in containment. Large amounts of hydrogen (700 kg), carbon monoxide (750 kg), and carbon dioxide (490 kg) were predicted to be generated during concrete ablation for the MAAP cases.

Recently, within the October 2012 timeframe, TEPCO was able to insert a camera along with instrumentation through a penetration into the Unit 1 PCV [83]. Video within containment was obtained; however, the information has not been fully scrutinized and interpreted as of this report. The camera was able to view a small portion of the drywell floor [84] in a drywell location approximately 180 degrees opposite from the pedestal doorway. Core melt did not appear to be present in this view. Future analysis and data collection as to the debris location will provide insight into the accident progression.

This page intentionally left blank.

6. REFERENCES

1. R.O. Gauntt, D. A. Kalinich, J. Cardoni, A. Goldmann, J. Phillips, S. Pickering, C. Smith, S. St. Germain, D. Schwieder, C. Phelan, M. W. Francis, K. R. Robb, L. J. Ott, and D. Wang, "Fukushima Daiichi Accident Study," SAND2012-6173, July 2012.
2. David Luxant et al., "Fukushima Technical Evaluation: Phase 1 – MAAP5 Analysis," EPRI Technical Report, in preparation.
3. T.G. Theofanous, H. Yan, M.Z. Podowski, C.S. Cho, D.A. Powers, T.J. Heames, J.J. Sienicki, C.C. Chu, B.W. Spencer, J.C. Castro, Y.R. Rashid, R.A. Dameron, J.S. Maxwell, "The Probability of Mark-I Containment Failure by Melt-Attack of the Liner", NUREG/Cr-6025, November (1993).
4. S. Lomperski and M. T. Farmer, "Corium Crust Strength Measurements," Nucl. Eng. Design, 238, 2551 (2009).
5. Nuclear Emergency Response Headquarters, Government of Japan, "Report of Japanese Government to the IAEA Ministerial Conference on Nuclear Safety - The Accident at TEPCO's Fukushima Nuclear Power Stations," June 2011.
6. Y. Yamanaka, Tokyo Electric Power Company, Inc., "Research plan regarding improvement of simulation code for understanding the status of fuel debris in the reactor," International Symposium on the Decommissioning of TEPCO's Fukushima Daiichi Nuclear Power Plant Unit 1-4, Tokyo, Japan, March 14, 2012.
7. Tokyo Electric Power Company Inc. (TEPCO), "Amendments to the estimate value of the core damage ratio of Unit 1 to 3 of Fukushima Daiichi Nuclear Power Station based on the measurement of the Containment Atmospheric Monitoring System," press release, Apr. 27, 2011.
8. Tokyo Electric Power Company Inc. (TEPCO), "The Evaluation Status of Reactor Core Damage at Fukushima Daiichi Nuclear Power Station Units 1 to 3," press release handout, Nov. 30, 2011.
9. Tokyo Electric Power Company Inc. (TEPCO), "Various Approaches for Understanding State of Nuclear Fuel," press release handout, Nov. 30, 2011.
10. M. T. Farmer, J. J. Sienicki, and B. W. Spencer, "The MELTSPREAD-1 Computer Code for the Analysis of Transient Spreading in Containments," Proceedings of ANS Winter Meeting, Washington D.C., Nov. 11–15, 1990.
11. M. T. Farmer, J. J. Sienicki, C. C. Chu and B. W. Spencer, "The MELTSPREAD-1 Code for Analysis of Transient Spreading and Cooling of High-Temperature Melts, Code Manual," EPRI TR-103413 (1993).
12. M. T. Farmer, "The CORQUENCH Code for Modeling of Ex-Vessel Corium Coolability Under Top Flooding Conditions, Code Manual – Version 3.03", OECD/MCCI-2010-TR03, Draft March, 2010.
13. M. T. Farmer, "Modeling of Ex-Vessel Corium Coolability with the CORQUENCH Code," Proceedings ICONE-9, Nice, France (2001).
14. D. R. Bradley, D. R. Gardner, J. E. Brockmann, and R. O. Griffith, "CORCON-MOD3: An Integrated Computer Model for Analysis of Molten Core-Concrete Interactions," NUREG/CR-5843, October, 1993.
15. M. T. Farmer, D. J. Kilskonk, and R. W. Aeschlimann, "Corium Coolability Under Ex-Vessel Accident Conditions for LWRs," Nuclear Engineering and Technology, 41, 5 (2009).
16. K. R. Robb and M. L. Corradini, "Ex-Vessel Corium Coolability Sensitivity Study with CORQUENCH Code," Proc. of NURETH-13, ANS, Sept. 27-Oct. 2, Kanazawa, Japan, paper N13P1290, 2009.
17. K. R. Robb and M. L. Corradini, "MCCI Simulation Comparison Between MELCOR and CORQUENCH," Proc. of NURETH-14, ANS, September 25-30, Toronto, Canada, paper 289, 2011.

18. M. T. Farmer and S. Basu, "Melt Spreading Code Assessment, Modifications, and Initial Applications to the EPR Core Catcher Design," Proceedings ICAPP '09, Tokyo, Japan (2009).
19. C. Journeau, J.-F. Haquet, B. Spindler, C. Spengler, and J. Foit, "The VULCANO VE-U7 Corium Spreading Benchmark," Progress in Nuclear Energy, 48, 215 (2006).
20. T. Loulou, E. A. Artyukhin, and J. P. Bardon, "Estimation of Thermal Contract Resistance during the First Stages of Metal Solidification Process: I – Experiment Principle and Modelisation, International J. of Heat and Mass Transfer, 42, 2119 (1999).
21. T. Loulou, E. A. Artyukhin, and J. P. Bardon, "Estimation of Thermal Contract Resistance during the First Stages of Metal Solidification Process: II – Experimental Setup and Results," International J. of Heat and Mass Transfer, 42, 2129 (1999).
22. W. Wang and H.–H. Qiu, "Interfacial Thermal Conductance in Rapid Contact Solidification Process," Int. J. of Heat and Mass Transfer, 45, 2043 (2002).
23. C. Journeau, E. Boccaccio, C. Brayer, G. Cognet, J .F. Haquet, C. Jégou, P. Piluso, and J. Monerris, "Ex-Vessel Corium Spreading: Results from the VULCANO Spreading Tests," Nuclear Engineering and Design, 223, 75 (2003).
24. M. Ishii and N. Zuber, "Drag Coefficient and Relative Velocity in Bubbly, Droplet or Particulate Flows," AlChE Journal, 25, 843 (1979).
25. M. Ramacciotti, C. Journeau, F. Sudreau, and G. Cognet, "Viscosity Models for Corium Melts," Nuclear Engineering and Design, 204, 377 (2001).
26. T. B. Benjamin, "Gravity Currents and Related Phenomena," J. Fluid Mechanics, 31, 208 (1968).
27. T. G. Theofanous, W. H. Amarasooriya, H. Yan, and U. Ratnam, "The Probability of Liner Failure in a Mark I Containment," NUREG/CR-5423 (1991).
28. J M. Veteau, B. Spindler, and G. Daum, "Modelling of Two-Phase Friction from Isothermal Spreading Experiments with Gas Fed from the Bottom and Application to Spreading Accompanied by Solidification," Proceedings NURETH-10, Seoul, Korea (2003).
29. G. Cognet et al., "Corium Spreading and Coolability CSC Project," Nuclear Engineering and Design, 209, 127 (2001).
30. D. Magallon and W. Tromm, "Dry and Wet Spreading Experiments with Prototypic Material at the FARO Facility," OECD Workshop on Ex-Vessel Debris Coolability, Karlsruhe, Germany (1999).
31. M. Sappok and W. Steinwarz, "COMAS Experiments as Contribution to the Validation of the EPR Mitigation Concept for Core Melt Accidents," Proceedings ICONE-6, San Diego, California (1998).
32. W. Steinwarz, A. Alemberti, W. Häfner, Z. Alkan, and M. Fischer, "Investigations on the Phenomenology of Ex-Vessel Core Melt Behavior (COMAS)," Nuclear Engineering and Design, 209, 139 (2001).
33. T. N. Dinh, M. Konovalikhin, D. Paladino, J. A. Green, A. Gubaidulin, and B. R. Sehgal, "Experimental Simulation of Core Melt Spreading on a LWR Containment Floor in a Severe Accident," Proceedings ICONE-6, San Diego, California (1998).
34. G. Engel, G. Fieg, H. Massier, U. Stegmaier, and W. Schütz, "KATS Experiments to Simulate Corium Spreading in the EPR Core Catcher Concept," OECD Workshop on Ex-Vessel Debris Coolability, Karlsruhe, Germany (1999).
35. B. Eppinger, G. Fieg, H. Massier, W. Schütz, and U. Stegmaier, and G. Stern, "SternSimulationsexperimente zum Ausbreitungsverhalten von Kernschmelzen: KATS-8 bis KATS-17," FZKA 6589 (2001).
36. J. J. Foit, "Large-Scale ECOKATS Experiments: Spreading of Oxide Melt on Ceramic and Concrete Surfaces," Nuclear Engineering and Design, 236, 2567 (2006).

37. H. Alsmeyer, T. Cron, J. J. Foit, G. Messemer, S. Schmidt-Stiefel, W. Hafner, and H. Kriscio, "Experiment ECOKATS-2 on Melt Spreading and Subsequent Top Flooding," FZKA 7084 (2005).
38. H. Suzuki, et al., "Fundamental Experiments and Analysis for Melt Spreading on a Concrete Floor," Proceedings ICONE-2, San Francisco, CA, March 21–25 (1993).
39. B. Spindler, J. M. Veteau, C. Brayer, M. Cranga, L. De Cecco, P. Montanelli, and D. Pineau, "Assessment of THEMA Code Against Spreading Experiments," OECD Workshop on Ex-Vessel Debris Coolability, Karlsruhe, Germany (1999).
40. B. Spindler and J.M. Veteau, "The Simulation of Melt Spreading with THEMA Code Part 1: Model, Assessment Strategy and Assessment Against Analytical and Numerical Solutions," Nuclear Engineering and Design, 236, 415 (2006).
41. B. Spindler and J.M. Veteau, "The Simulation of Melt Spreading with THEMA Code Part 2: Model, Assessment Against Spreading Experiments," Nuclear Engineering and Design, 236, 425 (2006).
42. G. Nazare, G. Ondracek, G., and B. Shulz, "Properties of Light Water Reactor Core Melts," Nucl. Tech., 32, 239 (1977).
43. H. R. Shaw, "Viscosities of Magmatic Silicate Liquids: An Empirical Method of Prediction," American J. of Science, 272, 870 (1972).
44. M. Kunitz, "An Empirical Formula for the Relationship between Viscosity of Solution and Volume of Solute," J. General Physiology, 9, 715 (1926).
45. J. E. Brockmann, F. E. Arellano, and D. A. Lucero, "Validation of Models of Gas Holdup in the CORCON Code," NUREG/CR-5433 (1989).
46. G.B. Wallis, One-Dimensional Two-Phase Flow, 2nd Ed., McGraw Hill, New York, 1979.
47. Kataoka and M. Ishii, "Drift Flux Model for Large Diameter Pipe and New Correlation for Pool Void Fraction," Int. J. Heat Mass Transfer, 30, 1927 (1987).
48. M. L. Corradini, "A Transient Model for the Ablation and Decomposition of Concrete," Nucl. Tech., 62, 263 (1983).
49. D. R. Bradley, "Modeling of Heat Transfer Between Core Debris and Concrete," ANS Proc. 1988 National Heat Transfer Conf., Houston, Texas USA, July 24-28 (1988).
50. S. S. Kutateladze and I. G. Malenkov, "Boiling and Bubbling heat Transfer under the Conditions of free and Forced convection," 6th Int. Heat Transfer Conf., Toronto, Canada, August 7-11 (1978).
51. T. Sevon, "A Heat Transfer Analysis of the CCI Experiments 1-3," Nucl. Eng. Design, 238, 2377 (2008).
52. M. T. Farmer, J. J. Sienicki, and B. W. Spencer, "CORQUENCH: A Model for Gas Sparging-Enhanced, Melt-Water, Film Boiling Heat Transfer," ANS Winter Meeting on the Thermal Hydraulics of Severe Accidents, Washington, D.C. USA, November 11-15 (1990).
53. M. T. Farmer et al., "Modeling and Database for Melt-Water Interfacial Heat Transfer," 2nd CSNI Specialist Meeting on Core Debris-Concrete Interactions, Karlsruhe, Germany, April 1-3 (1992).
54. S. Lomperski and M. T. Farmer, "Experimental Evaluation of the Water Ingression Mechanism for Corium Cooling," Nucl. Eng. Design, 237, 905 (2006).
55. R. J. Lipinski, "A Particle-Bed Dryout Model with Upward and Downward Boiling," Trans. Amer. Nucl. Soc., 35, 358 (1980).
56. J. M. Bonnet and J. M. Seiler, "Coolability of Corium Spread Onto Concrete Under Water, the PERCOLA Model," 2nd CSNI Specialist Meeting on Core Debris-Concrete Interactions," Karlsruhe, Germany, April 1-3 (1992).
57. F. B. Ricou and D. B. Spalding, "Measurements of Entrainment of Axisymmetrical Turbulent Jets," J. Fluid Mechanics, 11, 21 (1961).

58. M. T. Farmer, "Phenomenological Modeling of the Melt Eruption Cooling Mechanism During Molten Corium Concrete Interaction (MCCI)," Proceedings ICAPP '06, Reno, Nevada USA, June 6-8 (2006).
59. R. J. Roark and W. C. Young, Formulas for Stress and Strain, 6th Ed., McGraw Hill, New York, 1975. (see pp. 480-482).
60. M. T. Farmer, B. W. Spencer, D. J. Kilsdonk, and R. W. Aeschlimann, "Results of MACE Corium Coolability Experiments M0 and M1b," Proceedings 8th Int. Conf. on Nucl. Eng., Baltimore, MD USA, April 2-6 (2000).
61. M. T. Farmer, B. W. Spencer, J. L. Binder, and D. J. Hill, "Status and Future Direction of the Melt Attack and Coolability Experiments (MACE) Program at Argonne National Laboratory," Proceedings 9th Int. Conf. on Nucl. Eng., Nice, France, April 8-12 (2001).
62. D. H. Thompson, J. K. Fink, D. R. Armstrong, B. W. Spencer, and B. R. Sehgal, "Thermal-Hydraulic Aspects of the Large-Scale MCCI Tests in the ACE Program," 2nd CSNI Specialist Meeting on Core Debris-Concrete Interactions, Karlsruhe, Germany, April 1-3 (1992).
63. D. H. Thompson, M. T. Farmer, J. K. Fink, D. R. Armstrong, and B. W. Spencer, "ACE Phase C Final Report: Volume I-MCCI Thermalhydraulic Results," EPRI/ACE-TR-C42 (1997).
64. E. R. Copus, "Sustained Uranium Dioxide/Concrete Interaction Tests: The SURC Test Series," 2nd CSNI Specialist Meeting on Core Debris-Concrete Interactions, Karlsruhe, Germany, April 1-3 (1992).
65. M. T. Farmer, S. Lomperski, D. J. Kilsdonk, and R. W. Aeschlimann, "OECD MCCI-2 Project Final Report," OECD/MCCI-2010-TR07 (2010).
66. M. T. Farmer, S. Lomperski, and S. Basu, "Results of Reactor Material Experiments Investigating 2-D Core-Concrete Interaction and Debris Coolability," Proceedings ICAPP '04, Pittsburgh, PA USA, June 13-17 (2004).
67. M. T. Farmer, S. Lomperski, and S. Basu, "The Results of the CCI-2 Reactor Material Experiment Investigating 2-D Core-Concrete Interaction and Debris Coolability," Proceedings NURETH-11, Avignon, France, October 2-6 (2005).
68. M. T. Farmer, S. Lomperski, D. Kilsdonk, R. W. Aeschlimann, and S. Basu, "A Summary of Findings from the Melt Coolability and Concrete Interaction (MCCI) Program," Proceedings ICAPP '07, Nice, France, May 13-18 (2007).
69. D. Kalinich, Sandia National Laboratory, personal communication to M. T. Famer, Argonne National Laboratory, September 19, 2012.
70. D. Kalinich, Sandia National Laboratory, personal communication to M. T. Famer, Argonne National Laboratory, July 13, 2012.
71. H. Martin, "Heat and Mass Transfer Between Impinging Gas Jets and Solid Surfaces," Advances in Heat Transfer, 31, 1 (1977).
72. T. G. Theofanous et al., "Bubble-Induced Circulation and Associated Boundary Heat Transfer," Nuclear Engineering and Design, 121, 93 (1990).
73. Nuclear Emergency Response Headquarters, Government of Japan, "Report of Japanese Government to the IAEA Ministerial Conference on Nuclear Safety - The Accident at TEPCO's Fukushima Nuclear Power Stations", June 2011.
74. Tokyo Electric Power Company Inc. (TEPCO), "Volume of water injected into the reactor of Unit 1 to Unit 3 of Fukushima Nuclear Power Station," May 31, 2011.
75. M. T. Farmer, R. W. Aeschlimann, D. J. Kilsdonk, and B. W. Spencer, "Results of MACE Test M3b Posttest Debris Characterization," EPRI/ACEX-TR-C32 (2000).
76. M. T. Farmer, S. Lomperski, D. J. Kilsdonk, and R. W. Aeschlimann, "OECD MCCI Project Final Report," OECD/MCCI-2005-TR06 (2006).
77. L.T. Phan, "Fire Performance of High-Strength Concrete: A Report of the State-of-the-art," NISTIR 5934, December 1996.

78. J.H. Ptacek, Z. Feng, R.L. Engelstad, E.G. Lovell, M.L. Corradini, B.R. Sehgal, "Modeling of the MCCI Phenomena with the Presence of a Water Layer," Proceedings of the Second OCED (NEA) CSNI Specialist Meeting on Molten Core Debris-Concrete Interactions, Karlsruhe, Germany, April 1-3, 1992.
79. Tokyo Electric Power Company Inc. (TEPCO), "Fukushima Daiichi Nuclear Power Station Unit1 Parameters of Water level and Pressure", accessed December 1, 2011.
80. M. Epstein, "Dryout Heat Flux During Penetration of Water Into Solidifying Rock," J. Heat Transfer, 128, 847 (2006).
81. Tokyo Electric Power Company Inc. (TEPCO), "MAAP Analysis and Core Concrete Reaction," press release handout, Nov. 30, 2011.
82. C. C. Chu, J. J. Sienicki, and B.W. Spencer, "The Effects of Below-Vessel Structure and Water on Ex-Vessel Melt Arrival Conditions in a MARK I Containment," Proceedings NURETH-5, Salt Lake City, UT, September 21-24 (1992).
83. Tokyo Electric Power Company Inc. (TEPCO), "Investigation Results of the Inside of Unit 1 PCV at Fukushima Daiichi Nuclear Power Station," press release handout, Oct. 10, 2012.
84. Tokyo Electric Power Company Inc. (TEPCO), "Investigation of the Inside of Unit 1 PCV Using a CCD Camera at Fukushima Daiichi Nuclear Power Station (October 11)," press release handout, Oct. 12, 2012.

This page intentionally left blank.

APPENDIX A - CORQUENCH Result Data

Table A-1. CORQUENCH Case 1 - Simulation Time (min) until Melt Solidification

Case	1 Sump	2 Inner Pedestal	3 Edge Pedestal	4 Doorway	5 Door Exit	6 Drywell
MELCOR-1-1	151	63	42	24	18	2
MELCOR-2-1	59	59	43	22	19	15
MELCOR-3-1	139	41	34	13	10	9
MELCOR-4-1	145	58	56	46	18	2
MELCOR-5-1	137	42	41	39	40	40
MELCOR-6-1	42	44	43	41	43	42
MAAP-HP-1-1	1361	473	455	497	479	439
MAAP-HP-2-1	1344	479	455	494	476	439
MAAP-HP-3-1	1362	476	458	500	483	440
MAAP-HP-4-1	1361	473	455	497	479	439
MAAP-LP-1-1	1184	350	334	376	352	318
MAAP-LP-2-1	1179	357	335	373	345	318
MAAP-LP-3-1	1179	353	338	381	356	320
MAAP-LP-4-1	1176	349	333	376	352	319

Table A-2. CORQUENCH Case 1 - Total Gas Release (moles)

Case	H_2 (moles)	CO (moles)	CO_2 (moles)
MELCOR-1-1	37400	3690	10
MELCOR-2-1	32400	3145	10
MELCOR-3-1	39600	3862	20
MELCOR-4-1	37400	3670	0
MELCOR-5-1	77800	7780	0
MELCOR-6-1	68880	6956	0
MAAP-HP-1-1	347000	26300	10800
MAAP-HP-2-1	347000	26200	10600
MAAP-HP-3-1	348000	26900	11200
MAAP-HP-4-1	347000	26300	10800
MAAP-LP-1-1	345000	26300	7500
MAAP-LP-2-1	345000	26300	7320
MAAP-LP-3-1	347000	27000	7570
MAAP-LP-4-1	345000	26300	7310

Table A-3. CORQUENCH Case 1 - Total Axial Concrete Ablation (cm)

Case	1 Sump	2 Inner Pedestal	3 Edge Pedestal	4 Doorway	5 Door Exit	6 Drywell
MELCOR-1-1	13.4	8.9	6.9	5.1	4.4	1.3
MELCOR-2-1	8.3	8.6	7.1	4.9	4.5	4.1
MELCOR-3-1	12.7	6.9	6.2	3.7	3.4	3.2
MELCOR-4-1	13.1	8.4	8.2	7.2	4.4	1.3
MELCOR-5-1	12.9	7.4	6.9	6.8	6.9	8.4
MELCOR-6-1	6.7	7.4	7.4	6.6	7.3	7.3
MAAP-HP-1-1	64.1	22.6	15.2	20.9	21.3	10.7
MAAP-HP-2-1	63.5	24.2	15.3	20.5	20.6	10.7
MAAP-HP-3-1	64.1	23.4	16.2	21.5	22.5	11.4
MAAP-HP-4-1	64.0	22.6	15.2	20.9	21.4	10.7
MAAP-LP-1-1	59.2	21.5	14.4	20.2	19.1	10.0
MAAP-LP-2-1	58.9	23.2	14.6	19.7	17.5	10.1
MAAP-LP-3-1	58.9	22.2	15.6	20.9	20.3	10.6
MAAP-LP-4-1	58.8	21.1	14.4	20.2	19.1	10.1

Table A-4. CORQUENCH Case 1 - Total Radial Concrete Ablation (cm)

Case	1 Sump	2 Inner Pedestal	3 Edge Pedestal	4 Doorway	5 Door Exit	6 Drywell
MELCOR-1-1	19.9	n/a	2.2	0.7	0.2	0.0
MELCOR-2-1	4.2	n/a	2.3	0.6	0.3	0.1
MELCOR-3-1	16.5	n/a	1.4	0.0	0.0	0.1
MELCOR-4-1	18.1	n/a	3.7	2.6	0.2	0.0
MELCOR-5-1	16.9	n/a	5.3	6.0	5.6	6.4
MELCOR-6-1	4.3	n/a	2.9	5.1	3.0	3.7
MAAP-HP-1-1	64.1	n/a	15.4	21.1	21.4	10.9
MAAP-HP-2-1	63.5	n/a	15.4	20.7	20.7	10.9
MAAP-HP-3-1	64.1	n/a	16.3	21.7	22.6	11.5
MAAP-HP-4-1	64.0	n/a	15.4	21.1	21.5	10.9
MAAP-LP-1-1	59.2	n/a	14.6	20.2	19.2	10.2
MAAP-LP-2-1	58.9	n/a	14.8	19.8	17.6	10.3
MAAP-LP-3-1	58.9	n/a	15.8	20.9	20.4	10.8
MAAP-LP-4-1	58.8	n/a	14.6	20.2	19.2	10.3

Table A-5. CORQUENCH Case 2 - Simulation Time (min) until Melt Solidification

Case	1 Sump	2 Inner Pedestal	3 Edge Pedestal	4 Doorway	5 Door Exit	6 Drywell
MELCOR-1-2	**2879**	**2879**	**2879**	**2879**	**2879**	2
MELCOR-2-2	**2879**	**2879**	**2879**	**2879**	**2879**	**2879**
MELCOR-3-2	**2879**	**2879**	**2879**	45	33	27
MELCOR-4-2	**2879**	**2879**	**2879**	**2879**	**2879**	2
MELCOR-5-2	**2879**	**2879**	**2879**	46	**2879**	**2879**
MELCOR-6-2	**2879**	**2879**	**2879**	**2879**	**2879**	**2879**
MAAP-HP-1-2	**2880**	**2880**	**2880**	**2880**	**2880**	**2880**
MAAP-HP-2-2	**2880**	**2880**	**2880**	**2880**	**2880**	**2880**
MAAP-HP-3-2	**2880**	**2880**	**2880**	**2880**	**2880**	**2880**
MAAP-HP-4-2	**2880**	**2880**	**2880**	**2880**	**2880**	**2880**
MAAP-LP-1-2	**2879**	**2879**	**2879**	**2879**	**2879**	**2879**
MAAP-LP-2-2	**2879**	**2879**	**2879**	**2879**	**2879**	**2879**
MAAP-LP-3-2	**2879**	**2879**	**2879**	**2879**	**2879**	**2879**
MAAP-LP-4-2	**2879**	**2879**	**2879**	**2879**	**2879**	**2879**

Table A-6. CORQUENCH Case 2 - Total Gas Release (moles)

Case	H_2 (moles)	CO (moles)	CO_2 (moles)
MELCOR-1-2	**613000**	**59400**	**33500**
MELCOR-2-2	**614000**	**58400**	**31900**
MELCOR-3-2	**463000**	**45300**	**28800**
MELCOR-4-2	**645000**	**62300**	**34500**
MELCOR-5-2	**515000**	**46300**	**30310**
MELCOR-6-2	**524900**	**46730**	**29230**
MAAP-HP-1-2	**347000**	**26100**	**31710**
MAAP-HP-2-2	**347000**	**26100**	**31760**
MAAP-HP-3-2	**348000**	**26800**	**32100**
MAAP-HP-4-2	**347000**	**26100**	**31700**
MAAP-LP-1-2	**350000**	**26200**	**30660**
MAAP-LP-2-2	**350000**	**26200**	**31050**
MAAP-LP-3-2	**351000**	**26800**	**31000**
MAAP-LP-4-2	**350000**	**26200**	**30540**

*Values noted in bold are the results for cases where the debris has not fully solidified before the end of the simulation (2 days of simulated time in CORQUENCH).

Table A-7. CORQUENCH Case 2 - Total Axial Concrete Ablation (cm)

Case	1 Sump	2 Inner Pedestal	3 Edge Pedestal	4 Doorway	5 Door Exit	6 Drywell
MELCOR-1-2	**81.4**	**419.1**	**94.0**	**41.3**	**58.5**	1.3
MELCOR-2-2	**58.2**	**403.2**	**95.1**	**37.1**	**60.7**	**49.7**
MELCOR-3-2	**83.0**	**326.4**	**85.2**	8.6	7.7	6.8
MELCOR-4-2	**79.7**	**398.6**	**108.4**	**68.7**	**58.5**	1.3
MELCOR-5-2	**78.5**	**137.2**	**37.2**	8.6	**40.9**	**37.9**
MELCOR-6-2	**20.5**	**151.5**	**43.2**	**24.0**	**48.3**	**46.9**
MAAP-HP-1-2	**87.9**	**19.4**	**13.4**	**17.0**	**17.5**	**9.8**
MAAP-HP-2-2	**87.5**	**29.3**	**13.4**	**16.7**	**17.0**	**9.8**
MAAP-HP-3-2	**87.9**	**20.1**	**14.2**	**17.5**	**18.6**	**10.6**
MAAP-HP-4-2	**87.9**	**19.4**	**13.4**	**17.0**	**17.6**	**9.8**
MAAP-LP-1-2	**86.7**	**19.2**	**13.4**	**17.2**	**16.4**	**9.8**
MAAP-LP-2-2	**86.7**	**29.3**	**13.5**	**16.8**	**15.2**	**9.9**
MAAP-LP-3-2	**86.7**	**19.7**	**14.3**	**17.8**	**17.5**	**10.6**
MAAP-LP-4-2	**86.6**	**18.8**	**13.3**	**17.2**	**16.4**	**9.9**

Table A-8. CORQUENCH Case 2 - Total Radial Concrete Ablation (cm)

Case	1 Sump	2 Inner Pedestal	3 Edge Pedestal	4 Doorway	5 Door Exit	6 Drywell
MELCOR-1-2	**96.3**	n/a	**102.1**	**44.0**	**59.7**	0.0
MELCOR-2-2	**65.0**	n/a	**103.5**	**39.2**	**62.2**	**49.7**
MELCOR-3-2	**97.4**	n/a	**91.3**	7.3	4.5	1.4
MELCOR-4-2	**94.2**	n/a	**119.6**	**75.0**	**59.6**	0.0
MELCOR-5-2	**91.7**	n/a	**36.1**	7.4	**39.6**	**35.8**
MELCOR-6-2	**20.2**	n/a	**43.2**	**23.4**	**48.2**	**46.7**
MAAP-HP-1-2	**87.9**	n/a	**14.8**	**25.2**	**33.5**	**9.8**
MAAP-HP-2-2	**87.5**	n/a	**15.0**	**23.9**	**32.0**	**9.8**
MAAP-HP-3-2	**87.9**	n/a	**15.5**	**26.6**	**34.2**	**10.6**
MAAP-HP-4-2	**87.9**	n/a	**14.8**	**25.3**	**33.6**	**9.8**
MAAP-LP-1-2	**86.7**	n/a	**14.8**	**24.9**	**30.1**	**9.8**
MAAP-LP-2-2	**86.7**	n/a	**15.6**	**24.2**	**26.5**	**9.9**
MAAP-LP-3-2	**86.7**	n/a	**16.1**	**27.3**	**31.3**	**10.6**
MAAP-LP-4-2	**86.6**	n/a	**14.8**	**25.1**	**30.3**	**9.9**

*Values noted in bold are the results for cases where the debris has not fully solidified before the end of the simulation (2 days of simulated time in CORQUENCH).

Table A-9. CORQUENCH Case 3 - Simulation Time (min) until Melt Solidification

Case	1 Sump	2 Inner Pedestal	3 Edge Pedestal	4 Doorway	5 Door Exit	6 Drywell
MELCOR-1-3	174	80	52	29	21	3
MELCOR-2-3	71	75	54	26	22	18
MELCOR-3-3	162	52	42	15	13	11
MELCOR-4-3	168	73	69	55	21	3
MELCOR-5-3	156	44	43	41	43	42
MELCOR-6-3	44	46	46	43	45	45
MAAP-HP-1-3	1737	481	462	522	495	442
MAAP-HP-2-3	1713	488	462	518	489	442
MAAP-HP-3-3	1739	485	466	527	501	445
MAAP-HP-4-3	1737	481	462	522	495	442
MAAP-LP-1-3	1540	358	341	396	361	322
MAAP-LP-2-3	1535	366	342	392	354	322
MAAP-LP-3-3	1534	361	346	403	367	324
MAAP-LP-4-3	1529	356	341	396	362	322

Table A-10. CORQUENCH Case 3 - Total Gas Release (moles)

Case	H_2 (moles)	CO (moles)	CO_2 (moles)
MELCOR-1-3	45100	4450	11
MELCOR-2-3	36100	3440	0
MELCOR-3-3	43600	4210	0
MELCOR-4-3	43000	4210	0
MELCOR-5-3	80900	7990	0
MELCOR-6-3	70100	6970	0
MAAP-HP-1-3	344000	24900	11800
MAAP-HP-2-3	344000	24900	11400
MAAP-HP-3-3	346000	25600	12200
MAAP-HP-4-3	344000	24900	11800
MAAP-LP-1-3	336000	24900	8370
MAAP-LP-2-3	337000	24900	8250
MAAP-LP-3-3	342000	25600	8610
MAAP-LP-4-3	337000	24900	8190

Table A-11. CORQUENCH Case 3 - Total Axial Concrete Ablation (cm)

Case	1 Sump	2 Inner Pedestal	3 Edge Pedestal	4 Doorway	5 Door Exit	6 Drywell
MELCOR-1-3	21.2	10.3	7.7	5.4	4.6	1.4
MELCOR-2-3	9.1	9.8	7.9	5.2	4.8	4.2
MELCOR-3-3	15.4	7.8	6.7	3.8	3.5	3.3
MELCOR-4-3	17.6	9.6	9.2	7.9	4.6	1.4
MELCOR-5-3	17.5	7.3	7.0	7.2	7.0	8.3
MELCOR-6-3	7.0	7.4	7.3	6.8	7.3	7.2
MAAP-HP-1-3	66.9	20.4	14.0	20.7	20.3	9.4
MAAP-HP-2-3	66.3	21.9	14.0	20.2	19.4	9.4
MAAP-HP-3-3	67.0	21.2	14.9	21.3	21.6	10.3
MAAP-HP-4-3	66.9	20.4	14.0	20.7	20.4	9.4
MAAP-LP-1-3	62.0	19.3	13.4	19.1	17.3	8.8
MAAP-LP-2-3	61.8	20.9	13.6	18.6	15.9	8.9
MAAP-LP-3-3	61.8	20.0	14.4	19.9	18.5	9.8
MAAP-LP-4-3	61.7	18.9	13.4	19.1	17.3	8.9

Table A-12. CORQUENCH Case 3 - Total Radial Concrete Ablation (cm)

Case	1 Sump	2 Inner Ped.	3 Edge Ped.	4 Doorway	5 Door Exit	6 Drywell
MELCOR-1-3	24.6	n/a	2.6	1.0	0.3	0.0
MELCOR-2-3	4.6	n/a	2.8	0.8	0.4	0.1
MELCOR-3-3	18.5	n/a	1.7	0.0	0.0	0.0
MELCOR-4-3	21.3	n/a	4.2	3.1	0.3	0.0
MELCOR-5-3	20.7	n/a	3.2	4.0	3.3	2.9
MELCOR-6-3	3.4	n/a	2.7	3.8	2.7	2.8
MAAP-HP-1-3	66.9	n/a	14.0	20.7	20.3	9.5
MAAP-HP-2-3	66.3	n/a	14.0	20.2	19.4	9.5
MAAP-HP-3-3	67.0	n/a	14.9	21.3	21.6	10.3
MAAP-HP-4-3	66.9	n/a	14.0	20.7	20.4	9.5
MAAP-LP-1-3	62.0	n/a	13.4	19.1	17.3	8.9
MAAP-LP-2-3	61.8	n/a	13.6	18.6	15.9	9.0
MAAP-LP-3-3	61.8	n/a	14.4	19.9	18.5	9.9
MAAP-LP-4-3	61.7	n/a	13.4	19.1	17.3	9.0

Table A-13. CORQUENCH Case 4 - Simulation Time (min) until Melt Solidification

Case	1 Sump	2 Inner Pedestal	3 Edge Pedestal	4 Doorway	5 Door Exit	6 Drywell
MELCOR-1-4	131	228	100	50	39	4
MELCOR-2-4	96	205	103	45	42	33
MELCOR-3-4	128	125	80	25	22	19
MELCOR-4-4	128	198	138	103	39	4
MELCOR-5-4	438	54	56	53	55	53
MELCOR-6-4	57	56	59	56	58	58
MAAP-HP-1-4	1387	499	476	530	508	454
MAAP-HP-2-4	1370	507	476	527	504	454
MAAP-HP-3-4	1388	503	480	534	513	456
MAAP-HP-4-4	1387	499	476	530	508	454
MAAP-LP-1-4	1214	373	353	405	374	333
MAAP-LP-2-4	1210	381	354	401	366	333
MAAP-LP-3-4	1210	376	357	411	380	335
MAAP-LP-4-4	1206	371	352	405	374	333

Table A-14. CORQUENCH Case 4 - Total Gas Release (moles)

Case	H_2 (moles)	CO (moles)	CO_2 (moles)
MELCOR-1-4	141000	14800	0
MELCOR-2-4	166000	17400	0
MELCOR-3-4	134000	14100	0
MELCOR-4-4	153000	16100	0
MELCOR-5-4	193000	20300	0
MELCOR-6-4	167000	17500	0
MAAP-HP-1-4	283000	29700	11200
MAAP-HP-2-4	283000	29600	10900
MAAP-HP-3-4	293000	30700	11200
MAAP-HP-4-4	283000	29700	11200
MAAP-LP-1-4	270000	28300	8880
MAAP-LP-2-4	271000	28400	8670
MAAP-LP-3-4	281000	29400	8720
MAAP-LP-4-4	271000	28400	8650

Table A-15. CORQUENCH Case 4 - Total Axial Concrete Ablation (cm)

Case	1 Sump	2 Inner Pedestal	3 Edge Pedestal	4 Doorway	5 Door Exit	6 Drywell
MELCOR-1-4	28.9	68.3	33.9	18.3	17.3	2.8
MELCOR-2-4	24.6	64.0	34.6	17.0	18.1	15.1
MELCOR-3-4	28.7	45.4	29.3	11.5	11.0	9.9
MELCOR-4-4	28.6	62.5	41.5	28.2	17.3	2.8
MELCOR-5-4	44.9	17.2	15.5	13.4	15.4	14.5
MELCOR-6-4	13.9	18.5	16.9	14.2	16.9	16.6
MAAP-HP-1-4	75.0	29.6	21.3	27.9	28.4	15.8
MAAP-HP-2-4	74.3	31.4	21.3	27.4	27.5	15.9
MAAP-HP-3-4	75.0	30.6	22.3	28.5	29.7	16.7
MAAP-HP-4-4	75.0	29.6	21.3	27.9	28.4	15.8
MAAP-LP-1-4	70.0	27.6	19.9	26.2	24.8	15.0
MAAP-LP-2-4	69.6	29.5	20.2	25.7	23.1	15.0
MAAP-LP-3-4	69.7	28.4	21.1	27.1	26.2	15.7
MAAP-LP-4-4	69.5	27.1	19.9	26.3	24.8	15.0

Table A-16. CORQUENCH Case 4 - Total Radial Concrete Ablation (cm)

Case	1 Sump	2 Inner Ped.	3 Edge Ped.	4 Doorway	5 Door Exit	6 Drywell
MELCOR-1-4	28.5	n/a	33.5	17.9	16.8	2.5
MELCOR-2-4	24.2	n/a	34.2	16.6	17.6	14.6
MELCOR-3-4	28.3	n/a	28.8	11.1	10.6	9.4
MELCOR-4-4	28.2	n/a	41.1	27.8	16.9	2.5
MELCOR-5-4	44.5	n/a	15.0	12.8	14.8	14.0
MELCOR-6-4	13.4	n/a	16.4	13.7	16.3	16.0
MAAP-HP-1-4	75.0	n/a	21.3	27.9	28.4	16.3
MAAP-HP-2-4	74.3	n/a	21.3	27.4	27.5	16.3
MAAP-HP-3-4	75.0	n/a	22.3	28.5	29.7	17.0
MAAP-HP-4-4	75.0	n/a	21.3	27.9	28.4	16.3
MAAP-LP-1-4	70.0	n/a	19.9	26.2	24.8	15.3
MAAP-LP-2-4	69.6	n/a	20.2	25.7	23.1	15.4
MAAP-LP-3-4	69.7	n/a	21.1	27.1	26.2	16.0
MAAP-LP-4-4	69.5	n/a	19.9	26.3	24.8	15.4

Table A-17. CORQUENCH Case 5 - Simulation Time (min) until Melt Solidification

Case	1 Sump	2 Inner Pedestal	3 Edge Pedestal	4 Doorway	5 Door Exit	6 Drywell
MELCOR-1-5	151	59	40	24	17	2
MELCOR-2-5	57	56	42	21	18	15
MELCOR-3-5	136	39	33	13	10	9
MELCOR-4-5	144	54	53	44	17	2
MELCOR-5-5	138	41	40	38	39	40
MELCOR-6-5	41	43	42	40	42	42
MAAP-HP-1-5	1122	462	447	484	467	434
MAAP-HP-2-5	1108	467	447	482	465	434
MAAP-HP-3-5	1122	465	450	487	471	435
MAAP-HP-4-5	1121	462	447	484	468	434
MAAP-LP-1-5	965	340	327	364	341	314
MAAP-LP-2-5	960	346	328	361	335	314
MAAP-LP-3-5	960	343	330	368	346	316
MAAP-LP-4-5	957	339	327	364	341	315

Table A-18. CORQUENCH Case 5 - Total Gas Release (moles)

Case	H_2 (moles)	CO (moles)	CO_2 (moles)
MELCOR-1-5	32900	3180	0
MELCOR-2-5	30700	2956	0
MELCOR-3-5	36200	3490	0
MELCOR-4-5	33100	3190	0
MELCOR-5-5	76200	7550	0
MELCOR-6-5	66700	6717	0
MAAP-HP-1-5	343000	25800	7090
MAAP-HP-2-5	343000	25700	6880
MAAP-HP-3-5	345000	26400	7380
MAAP-HP-4-5	343000	25800	7090
MAAP-LP-1-5	342000	25600	4700
MAAP-LP-2-5	341000	25700	4530
MAAP-LP-3-5	343000	26400	4830
MAAP-LP-4-5	342000	25600	4540

Table A-19. CORQUENCH Case 5 - Total Axial Concrete Ablation (cm)

Case	1 Sump	2 Inner Pedestal	3 Edge Pedestal	4 Doorway	5 Door Exit	6 Drywell
MELCOR-1-5	13.5	8.1	6.5	4.9	4.3	1.2
MELCOR-2-5	7.7	7.8	6.6	4.7	4.4	4.0
MELCOR-3-5	12.7	6.4	5.8	3.7	3.3	3.1
MELCOR-4-5	13.2	7.7	7.5	6.7	4.3	1.2
MELCOR-5-5	13.0	7.1	6.7	6.7	6.8	8.6
MELCOR-6-5	6.6	7.2	7.1	6.5	7.1	7.1
MAAP-HP-1-5	53.9	20.6	13.8	19.2	19.3	9.9
MAAP-HP-2-5	53.4	22.1	13.8	18.8	18.5	9.9
MAAP-HP-3-5	53.9	21.4	14.7	19.8	20.4	10.6
MAAP-HP-4-5	53.8	20.6	13.8	19.2	19.3	9.9
MAAP-LP-1-5	50.3	19.6	13.1	18.6	17.0	9.6
MAAP-LP-2-5	49.9	21.4	13.3	18.1	14.9	9.7
MAAP-LP-3-5	50.0	20.4	14.0	19.4	18.4	10.4
MAAP-LP-4-5	49.9	19.1	13.1	18.6	17.0	9.7

Table A-20. CORQUENCH Case 5 - Total Radial Concrete Ablation (cm)

Case	1 Sump	2 Inner Pedestal	3 Edge Pedestal	4 Doorway	5 Door Exit	6 Drywell
MELCOR-1-5	13.6	n/a	1.5	0.4	0.0	0.0
MELCOR-2-5	3.1	n/a	1.6	0.3	0.0	0.0
MELCOR-3-5	12.0	n/a	0.9	0.0	0.0	0.0
MELCOR-4-5	12.7	n/a	2.6	1.9	0.0	0.0
MELCOR-5-5	12.5	n/a	4.5	5.4	4.8	5.6
MELCOR-6-5	3.7	n/a	2.1	4.5	2.3	2.6
MAAP-HP-1-5	53.9	n/a	14.0	19.3	19.4	10.0
MAAP-HP-2-5	53.4	n/a	14.0	18.9	18.7	10.0
MAAP-HP-3-5	53.9	n/a	14.8	19.9	20.6	10.7
MAAP-HP-4-5	53.8	n/a	14.0	19.3	19.5	10.0
MAAP-LP-1-5	50.3	n/a	13.2	18.7	17.2	9.7
MAAP-LP-2-5	49.9	n/a	13.4	18.3	15.2	9.8
MAAP-LP-3-5	50.0	n/a	14.1	19.5	18.6	10.4
MAAP-LP-4-5	49.9	n/a	13.2	18.8	17.2	9.8

Table A-21. CORQUENCH Case 6 - Simulation Time (min) until Melt Solidification

Case	1 Sump	2 Inner Pedestal	3 Edge Pedestal	4 Doorway	5 Door Exit	6 Drywell
MELCOR-1-6	**2879**	**2879**	**2879**	**2879**	35	2
MELCOR-2-6	**2879**	**2879**	**2879**	**2879**	37	15
MELCOR-3-6	**2879**	**2879**	**2879**	**2879**	10	9
MELCOR-4-6	**2879**	**2879**	**2879**	**2879**	35	2
MELCOR-5-6	**2879**	44	40	**2879**	39	40
MELCOR-6-6	**2879**	48	42	**2879**	41	42
MAAP-HP-1-6	**2880**	**2880**	467	**2880**	**2880**	439
MAAP-HP-2-6	**2880**	**2880**	468	**2880**	**2880**	439
MAAP-HP-3-6	**2880**	**2880**	480	**2880**	**2880**	440
MAAP-HP-4-6	**2880**	**2880**	467	**2880**	**2880**	439
MAAP-LP-1-6	**2879**	**2879**	336	**2879**	**2879**	318
MAAP-LP-2-6	**2879**	**2879**	339	**2879**	**2879**	318
MAAP-LP-3-6	**2879**	**2879**	346	**2879**	**2879**	320
MAAP-LP-4-6	**2879**	**2879**	336	**2879**	**2879**	319

Table A-22. CORQUENCH Case 6 - Total Gas Release (moles)

Case	H_2 (moles)	CO (moles)	CO_2 (moles)
MELCOR-1-6	**305000**	**25900**	**2150**
MELCOR-2-6	**229500**	**18000**	**10**
MELCOR-3-6	**245000**	**19700**	**1680**
MELCOR-4-6	**326000**	**28300**	**1715**
MELCOR-5-6	**210000**	**19300**	**4200**
MELCOR-6-6	**92800**	**7790**	**150**
MAAP-HP-1-6	**347000**	**26200**	**23300**
MAAP-HP-2-6	**347000**	**26200**	**22900**
MAAP-HP-3-6	**348000**	**26900**	**23600**
MAAP-HP-4-6	**347000**	**26200**	**23300**
MAAP-LP-1-6	**347000**	**26200**	**21100**
MAAP-LP-2-6	**347000**	**26200**	**21100**
MAAP-LP-3-6	**348000**	**26900**	**21300**
MAAP-LP-4-6	**347000**	**26200**	**21000**

*Values noted in bold are the results for cases where the debris has not fully solidified before the end of the simulation (2 days of simulated time in CORQUENCH).
**Values highlight in grey are the results for cases where crust anchoring was predicted to have occurred.

Table A-23. CORQUENCH Case 6 - Total Axial Concrete Ablation (cm)

Case	1 Sump	2 Inner Pedestal	3 Edge Pedestal	4 Doorway	5 Door Exit	6 Drywell
MELCOR-1-6	**51.2**	**126.4**	**21.1**	**17.6**	3.7	1.3
MELCOR-2-6	**15.4**	**116.4**	**22.7**	**15.3**	3.7	3.8
MELCOR-3-6	**48.4**	**68.9**	**13.3**	**9.8**	2.8	3.2
MELCOR-4-6	**48.1**	**112.6**	**42.5**	**44.0**	3.6	1.3
MELCOR-5-6	**62.8**	6.7	6.4	**8.3**	6.3	8.4
MELCOR-6-6	**9.1**	6.5	6.8	**9.1**	6.7	7.3
MAAP-HP-1-6	**86.7**	**21.3**	14.7	**18.8**	**19.4**	10.7
MAAP-HP-2-6	**86.2**	**22.7**	14.7	**18.4**	**18.8**	10.7
MAAP-HP-3-6	**86.8**	**22.1**	15.6	**19.3**	**20.6**	11.4
MAAP-HP-4-6	**86.7**	**21.3**	14.7	**18.8**	**19.5**	10.7
MAAP-LP-1-6	**85.3**	**20.6**	14.1	**18.5**	**17.7**	10.0
MAAP-LP-2-6	**85.3**	**22.1**	14.3	**18.0**	**16.2**	10.1
MAAP-LP-3-6	**85.2**	**21.2**	15.2	**19.2**	**18.9**	10.6
MAAP-LP-4-6	**85.1**	**20.2**	14.0	**18.5**	**17.7**	10.1

Table A-24. CORQUENCH Case 6 - Total Radial Concrete Ablation (cm)

Case	1 Sump	2 Inner Pedestal	3 Edge Pedestal	4 Doorway	5 Door Exit	6 Drywell
MELCOR-1-6	**65.6**	n/a	**29.6**	**23.3**	0.5	0.0
MELCOR-2-6	**21.7**	n/a	**30.7**	**20.3**	0.6	0.1
MELCOR-3-6	**63.0**	n/a	**13.8**	**8.9**	0.0	0.1
MELCOR-4-6	**62.4**	n/a	**56.5**	**57.5**	0.5	0.0
MELCOR-5-6	**77.1**	n/a	4.8	**6.7**	4.7	6.4
MELCOR-6-6	**8.1**	n/a	2.8	**7.9**	2.8	3.7
MAAP-HP-1-6	**86.7**	n/a	14.8	**19.0**	**19.6**	10.9
MAAP-HP-2-6	**86.2**	n/a	14.9	**18.6**	**18.9**	10.9
MAAP-HP-3-6	**86.8**	n/a	15.7	**19.5**	**20.8**	11.5
MAAP-HP-4-6	**86.7**	n/a	14.8	**19.0**	**19.7**	10.9
MAAP-LP-1-6	**85.3**	n/a	14.3	**18.5**	**17.8**	10.2
MAAP-LP-2-6	**85.3**	n/a	14.5	**18.1**	**16.4**	10.3
MAAP-LP-3-6	**85.2**	n/a	15.3	**19.2**	**19.0**	10.8
MAAP-LP-4-6	**85.1**	n/a	14.2	**18.6**	**17.8**	10.3

*Values noted in bold are the results for cases where the debris has not fully solidified before the end of the simulation (2 days of simulated time in CORQUENCH).
**Values highlight in grey are the results for cases where crust anchoring was predicted to have occurred.

Table A-25. CORQUENCH Case 7 - Simulation Time (min) until Melt Solidification

	Section					
Case	1 Sump	2 Inner Pedestal	3 Edge Pedestal	4 Doorway	5 Door Exit	6 Drywell
MELCOR-1-7	**2879**	**2879**	**2879**	**2879**	**2879**	1
MELCOR-2-7	**2879**	**2879**	**2879**	**2879**	**2879**	**2879**
MELCOR-3-7	**2879**	**2879**	**2879**	**2879**	**2879**	**2879**
MELCOR-4-7	**2879**	**2879**	**2879**	**2879**	**2879**	1
MELCOR-5-7	**2879**	**2879**	**2879**	**2879**	**2879**	**2879**
MELCOR-6-7	**2879**	**2879**	**2879**	**2879**	**2879**	**2879**
MAAP-HP-1-7	**2880**	**2880**	**2880**	**2880**	**2880**	**2880**
MAAP-HP-2-7	**2880**	**2880**	**2880**	**2880**	**2880**	**2880**
MAAP-HP-3-7	**2880**	**2880**	**2880**	**2880**	**2880**	**2880**
MAAP-HP-4-7	**2880**	**2880**	**2880**	**2880**	**2880**	**2880**
MAAP-LP-1-7	**2879**	**2879**	**2879**	**2879**	**2879**	**2879**
MAAP-LP-2-7	**2879**	**2879**	**2879**	**2879**	**2879**	**2879**
MAAP-LP-3-7	**2879**	**2879**	**2879**	**2879**	**2879**	**2879**
MAAP-LP-4-7	**2879**	**2879**	**2879**	**2879**	**2879**	**2879**

Table A-26. CORQUENCH Case 7 - Total Gas Release (moles)

Case	H_2 (moles)	CO (moles)	CO_2 (moles)
MELCOR-1-7	**623000**	**65300**	**47500**
MELCOR-2-7	**611000**	**64100**	**40100**
MELCOR-3-7	**570000**	**59800**	**44900**
MELCOR-4-7	**655000**	**68600**	**49900**
MELCOR-5-7	**508000**	**53200**	**34700**
MELCOR-6-7	**506000**	**53000**	**29100**
MAAP-HP-1-7	**332000**	**34800**	**33800**
MAAP-HP-2-7	**332000**	**34800**	**33500**
MAAP-HP-3-7	**334000**	**35000**	**34700**
MAAP-HP-4-7	**332000**	**34800**	**33800**
MAAP-LP-1-7	**334000**	**35000**	**31700**
MAAP-LP-2-7	**335000**	**35100**	**31600**
MAAP-LP-3-7	**337000**	**35300**	**32400**
MAAP-LP-4-7	**335000**	**35100**	**31600**

*Values noted in bold are the results for cases where the debris has not fully solidified before the end of the simulation (2 days of simulated time in CORQUENCH).

Table A-27. CORQUENCH Case 7 - Total Axial Concrete Ablation (cm)

	Section					
Case	1 Sump	2 Inner Pedestal	3 Edge Pedestal	4 Doorway	5 Door Exit	6 Drywell
MELCOR-1-7	**106.2**	**505.3**	**109.7**	**56.6**	**69.5**	1.8
MELCOR-2-7	**74.3**	**484.8**	**111.0**	**52.4**	**71.8**	**60.7**
MELCOR-3-7	**104.4**	**383.0**	**99.7**	**35.4**	**45.4**	**40.4**
MELCOR-4-7	**107.0**	**478.6**	**126.8**	**84.6**	**69.4**	1.8
MELCOR-5-7	**99.1**	**146.8**	**50.3**	**34.9**	**53.7**	**50.5**
MELCOR-6-7	**32.4**	**160.8**	**55.3**	**37.1**	**59.5**	**58.4**
MAAP-HP-1-7	**97.6**	**49.9**	**34.7**	**46.7**	**49.4**	**24.9**
MAAP-HP-2-7	**97.2**	**53.8**	**34.8**	**45.9**	**47.9**	**24.9**
MAAP-HP-3-7	**97.6**	**51.8**	**36.1**	**47.5**	**51.2**	**25.4**
MAAP-HP-4-7	**97.6**	**49.9**	**34.7**	**46.7**	**49.6**	**24.9**
MAAP-LP-1-7	**96.4**	**48.4**	**34.0**	**46.5**	**45.4**	**24.6**
MAAP-LP-2-7	**96.4**	**53.1**	**34.6**	**45.6**	**42.0**	**24.6**
MAAP-LP-3-7	**96.3**	**50.5**	**35.8**	**47.9**	**47.5**	**24.9**
MAAP-LP-4-7	**96.2**	**47.9**	**34.0**	**46.6**	**45.5**	**24.7**

Table A-28. CORQUENCH Case 7 - Total Radial Concrete Ablation (cm)

	Section					
Case	1 Sump	2 Inner Pedestal	3 Edge Pedestal	4 Doorway	5 Door Exit	6 Drywell
MELCOR-1-7	**106.2**	n/a	**109.7**	**56.6**	**69.5**	1.8
MELCOR-2-7	**74.3**	n/a	**111.0**	**52.4**	**71.8**	**60.7**
MELCOR-3-7	**104.4**	n/a	**99.7**	**35.4**	**45.4**	**40.4**
MELCOR-4-7	**107.0**	n/a	**126.8**	**84.6**	**69.4**	1.8
MELCOR-5-7	**99.1**	n/a	**50.3**	**34.9**	**53.7**	**50.5**
MELCOR-6-7	**32.4**	n/a	**55.3**	**37.1**	**59.5**	**58.4**
MAAP-HP-1-7	**97.6**	n/a	**34.7**	**46.7**	**49.4**	**27.0**
MAAP-HP-2-7	**97.2**	n/a	**34.8**	**45.9**	**47.9**	**27.0**
MAAP-HP-3-7	**97.6**	n/a	**36.1**	**47.5**	**51.2**	**27.2**
MAAP-HP-4-7	**97.6**	n/a	**34.7**	**46.7**	**49.6**	**27.0**
MAAP-LP-1-7	**96.4**	n/a	**34.0**	**46.5**	**45.4**	**27.1**
MAAP-LP-2-7	**96.4**	n/a	**34.6**	**45.6**	**42.0**	**27.1**
MAAP-LP-3-7	**96.3**	n/a	**35.8**	**47.9**	**47.5**	**27.2**
MAAP-LP-4-7	**96.2**	n/a	**34.0**	**46.6**	**45.5**	**27.2**

*Values noted in bold are the results for cases where the debris has not fully solidified before the end of the simulation (2 days of simulated time in CORQUENCH).